TECHNISCHE UNIVERSITÄT MÜNCHEN
Advanced Technologies in Radiation Therapy

Uncertainties in biological dose response models and their integration in treatment planning of carbon ion therapy

Florian Kamp

Vollständiger Abdruck der von der Fakultät für Physik der Technischen Universität München zur Erlangung des akademischen Grades eines

Doktors der Naturwissenschaften (Dr. rer. nat.)

genehmigten Dissertation.

Vorsitzender:	Univ.-Prof. Dr. Martin Zacharias
Prüfer der Dissertation:	
	1. Univ.-Prof. Dr. Jan J. Wilkens
	2. Univ.-Prof. Dr. Franz Pfeiffer

Die Dissertation wurde am 07.01.2015 bei der Technischen Universität München eingereicht und durch die Fakultät für Physik am 19.02.2015 angenommen.

Physik-Department

Uncertainties in biological dose response models and their integration in treatment planning of carbon ion therapy

Dissertation
von

Florian Kamp

– Januar 2015 –

Technische Universität
München

Abstract

Purpose: Carbon ion radiotherapy aims to treat cancer with accelerated carbon ions by depositing dose inside a patient's body. Treatment planning is essential to develop an optimal treatment scheme to treat the tumor most efficiently and simultaneously spare normal tissue the best. Treatment plan evaluation is based on the RBE-weighted dose RWD (relative biological effectiveness (RBE) x deposited dose) which combines biological and physical concepts. RBE changes spatially depending on the irradiated cell type and the present ion spectra. Physical beam properties including deposited dose, linear energy transfer, nuclear fragmentation and lateral spread are considered in the treatment planning. The accuracy of the physical dose delivery was increased enormously with recent developments. RBE is predicted by biological modeling processes, extrapolating x-ray dose response to ions. Considerable uncertainties are associated with the commonly used biological models as well as with their input parameters. Current treatment planning systems for carbon ion therapy do not consider these uncertainties and display a definite RWD distribution. Physicians and medical physicists assess these uncertainties according to experience and general knowledge in the field. The objective of this work is to directly include and evaluate the impact of uncertainties in the biological dose response modeling on carbon ion treatment plans.

Methods: Treatment planning for carbon ion therapy is implemented in a research treatment planning environment. This is accomplished by combining Monte Carlo simulated physical beam behavior with biological model predictions to facilitate biological effect based treatment planning. Variance-based sensitivity analyses are adapted to the treatment planning process to account for uncertainties in the biological modeling and their impact on treatment plan. Within one execution of the sensitivity analysis 10^5 treatment plans are calculated in few hours, each with randomly changed input parameters. The random changes in the input settings represent the examined uncertainties. This provides the possibility to quantify and visualize the impact of different biological uncertainties on the resulting uncertainty of RWD distributions.

Results: The sensitivity analyses allow to examine the impact of different uncertainties on the planned treatment. Biological uncertainties result in considerable variations of the RWD distribution. This affects treatment outcome as it leads to potential under- or overdosage. The considerable uncertainties persist even in case an ideally precise physical dose delivery is assumed. The newly developed methods are able to identify the biological input parameters which have the highest impact on the resulting uncertainties in the treatment plan and therefore have the greatest potential to improve accuracy of carbon ion radiotherapy. The broad capability of the described approach is demonstrated in three-dimensional geometries based on computed tomography images of real patients.

Conclusion: It is essential to include biological dose response uncertainties in the treatment planning process of carbon ion radiotherapy. The presented sensitivity analysis is suitable for carbon ion treatment planning and provides new insight to improve it. The developed approach is an important contribution to enhance accuracy and reliability of carbon ion treatment planning and its evaluation.

Contents

Part I.

Introduction

Radiotherapy with carbon ions has the potential to improve treatment outcome. Due to their physical properties, carbon ions provide several advantages over x-ray or proton radiotherapy. The dose deposition of carbon ions is characterized by a steep Bragg peak and a small lateral spread. This offers the potential of very conformal dose application, potentially improving the treatment outcome and reducing side effects. In addition, carbon ions are densely ionizing. This is associated with an increased biological effectiveness. Carbon ion facilities for radiotherapy are either in use or planned at several institutions worldwide.

Carbon ion radiotherapy is based on two main aspects, a physical and a biological one. The physical dose has to be combined with biological effects to facilitate precise and accurate treatment. Recent developments in ion therapy allow very precise application of the physical dose. The modeling of the biological effects is complex and based on approximations, assumptions and extrapolation of the interplay of physical and biological properties. Currently the resulting uncertainties in the biological modeling are omitted in carbon ion treatment planning systems. Physicians and medical physicists assess these uncertainties according to experience and general knowledge in the field. The aim of this work is to include, analyze and visualize the impact of biological uncertainties on carbon ion treatment planning.

Topic of this introduction is to present the context of carbon ion therapy along with the uncertainties in biological dose response models. In chapters 1 and 2 the definitions necessary for biological dose response modeling are given. This starts with the rationale of radiotherapy in chapter 1. In this chapter also x-ray radiotherapy is introduced in combination with the required accuracy in treatment delivery and planning. Chapter 2 focuses on carbon ion therapy. This includes sections concerning the physical and biological principles applied to carbon ion therapy. The discussed uncertainties in biological dose response modeling for carbon ion therapy are presented in chapter 3. The aim of this thesis is to include these uncertainties into treatment plan evaluation to assess their impact and improve the reliability of treatment planning. The proceeding to achieve this aim within the scope of this thesis is outlined in chapter 4.

1. Radiotherapy

Radiotherapy aims to treat tumors with ionizing radiation. Soon after the discovery of x-rays by Röntgen in 1895 they were employed to treat cancer. Since then, external beam therapy has been continuously developed. State of the art techniques for radiotherapy with x-rays are based on linear accelerators and sophisticated beam shaping techniques. The developments facilitate to treat the tumor and at the same time spare normal, not malignant tissue as much as possible. Radiotherapy aims to irradiate the tumor with sufficient dose to achieve local control while the dose to adjacent organs at risk is minimized to avoid complications in normal tissue. This can be visualized by the therapeutic window in figure 1.1. The figure shows the tissue damage as function of the applied (cumulative) dose. The dose is defined as deposited energy per mass $d = \Delta E/\Delta m$ and is reported in Gray (1 Gy = 1 J kg^{-1}). For the tumor (blue line) high doses are favorable as they results in higher tumor control probability. The aim is to spare normal tissue in order to not induce critical normal tissue damage. The therapeutic window itself is the dose range where the probability of tumor control without normal tissue complications is the highest.

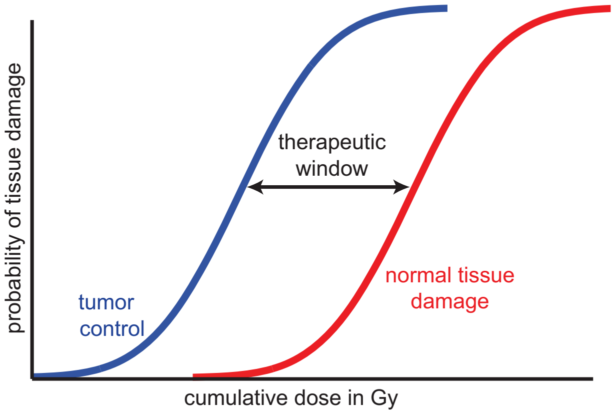

Figure 1.1.: Schematic representation of the dependencies of tumor control probability and normal tissue complication probability on the dose.

Both the probability of tumor control and of normal tissue complication are described by steep curves in the range of the therapeutic window. A small change in the dose has a potentially high impact on the probability of tumor control and normal tissue complications. This requires precise treatment and reliable treatment planning. New techniques, such as intensity modulated radiation therapy (IMRT) or volumetric arc therapy (VMAT) facilitate very conformal dose distribution matching the shape of the tumor. Typical requirements for treatment plans based on these modern techniques are very strict. For instance, applied requirements for the planning target volume (PTV) can be that 98% of the volume need to receive at least 95% of the prescribed dose and less than 2% of the volume are allowed to receive more than 107% of the prescribed dose.

This required accuracy of x-ray radiotherapy demonstrates the importance of the evaluation of uncertainties associated with different radiotherapy types. The aim of this thesis is to evaluate the uncertainties in biological dose response models for carbon ion treatment planning. The use of ion radiotherapy is based on favorable properties of ions. They have the potential to better balance the probabilities of tumor control and normal tissue complication than radiotherapy with x-rays. Ion therapy, especially carbon ion therapy, is topic of the following chapter.

2. Carbon Ion Radiotherapy

In this chapter carbon ion therapy is introduced. Due to their properties, carbon ion beams have the potential to provide more conformal physical dose distribution in combination with an increased biological effectiveness based on their dense ionization patterns. This facilitates a better normal tissue sparing. In order to show the potential of ion beams in radiotherapy, the depth-dose deposition for x-ray (photons), protons and carbon ion beams are discussed (section 2.1). In section 2.2 the physical properties of carbon ion beams are summarized followed by a section focusing on the biological modeling process (section 2.3). The biological modeling process is crucial to understand the biological uncertainties in dose response modeling for carbon ion therapy that will be addressed throughout this work.

2.1. Depth Dose Curves: Bragg Peaks

The application of light ion beams (proton and carbon ions) for radiotherapy spreads rapidly worldwide. The main rationale is the favorable energy loss of ions in matter, resulting in the characteristic dose maximum at the end of their range. This peak is characteristic for ions and known as the Bragg peak. A proton and a carbon ion Bragg peak are compared to the depth dose curve of photons (x-rays) in figure 2.1. In this example the depth of the proton and carbon ion Bragg peak is 15 cm, which corresponds to an initial beam energy of 147 MeV/u and 279 MeV/u for protons and carbon ions respectively. The depth of the peak can be adjusted by the ion energy. The higher the energy the deeper the Bragg peak. A superposition of several thousands pristine Bragg peaks with different energies and coming from several beam directions can be optimized to achieve homogeneous tumor coverage.

2.2. Basic Physics: Fragmentation, Linear Energy Transfer and Lateral Spread

In this section the underlying physical properties and concepts of carbon ion therapy are introduced and compared to proton and photon therapy. The main physical properties, important for carbon ion therapy can be classified into fragmentation, energy transfer and lateral behavior.

2.2.1. Fragmentation

One of the differences in the dose distribution between carbon ions and protons (cf. figure 2.1) is the fragmentation tail behind the Bragg peak. This tail is caused by nuclear interactions of the primary carbon ion beam with the atomic nuclei of the irradiated medium, resulting in the fragmentation of the carbon ion. The fragments are dominated by protons and alpha particles, but lithium, beryllium and boron ions are also generated. Some of

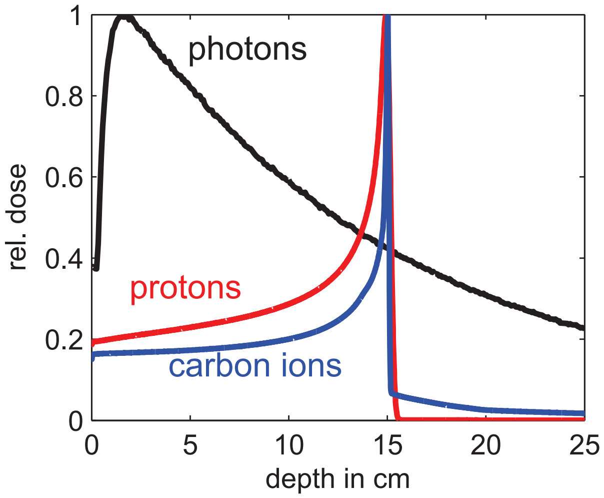

Figure 2.1.: Depth dose curves of broad photon (x-ray), proton and carbon ion beams. The energies of the beams are 6 MeV photons, 147 MeV/u protons and 279 MeV/u carbon ions. Protons and carbon ions show the characteristic Bragg peak. Carbon ions show in addition the fragmentation tail behind the peak.

these have energies high enough to travel considerable distances beyond the range of the initial carbon ions, producing the fragmentation tail [1].

There are two main reasons to consider the fragmentation of the carbon ion beam. On the one hand, fragments deposit dose behind the Bragg peak, where potential organs at risk (OAR) might be located. On the other hand, the effect of the irradiation on cells varies greatly for different ions and their energies.

2.2.2. Linear Energy Transfer (LET)

A second physical term widely used to describe radiation quality in carbon ion therapy is the linear energy transfer (LET). The dose-averaged LET concept is used throughout this work. For one ion type Z with a certain fluence $\Phi\left(E,Z\right)$ the dose-weighted LET can be written as

$$LET\left(Z\right) = \frac{\int_0^\infty \Phi\left(Z,E\right) \cdot \left(SP\left(Z,E\right)\right)^2 \mathrm{d}E}{\int_0^\infty \Phi\left(Z,E\right) \cdot SP\left(Z,E\right) \mathrm{d}E} \tag{2.1}$$

It is based on the stopping power $SP(E,Z) = \mathrm{d}E\left(Z\right)/\mathrm{d}l$, where $\mathrm{d}E$ is the energy lost by the ion in the distance $\mathrm{d}l$ [2, 3]. In addition, stopping powers depend on the medium which the particle is going through. Treatment planning is based on the “dose to water” concept in which dose calculations are done in water. This means that all materials are converted to their “water-equivalent”. Consequently SP and LET are considered in water.

For ion energies relevant in carbon ion therapy, one can generally state two relations. First, the slower the ion is, the larger becomes its stopping power. Second, the lighter the ion is, the smaller the stopping power. The restricted LET_Δ, which only accounts for the locally deposited energy by treating secondary electrons with energies higher than Δ separately, is not used here. Hence $LET = LET_\infty$ is assumed. In carbon ion therapy LET distributions are important, because the biology (in terms of cell survival after irradiation) depends on LET. The absolute values and the change of LET for proton therapy is less pronounced.

2.2.3. Lateral Spread

One of the rationales for the use of carbon ion therapy is a smaller lateral spread of carbon ions compared to protons while penetrating a material. Carbon ions are heavier than protons, hence their direction is less affected by multiple-scattering effects and range straggling [4]. This results in steeper lateral and distal dose gradients, promising the potential of better normal tissue sparing compared to proton therapy. Treatment planning for carbon ion therapy must consider the lateral beam behavior.

2.3. Basic Biology: Cell Survival, LQ-Model and RBE

The aim of radiotherapy is to kill cancer cells with ionizing radiation. Cells respond differently to radiation. Biological modeling is needed to predict the radiation response of biological systems. The linear-quadratic (LQ) model [5] is widely used to describe the survival fraction S of cells irradiated with the dose d.

$$S = e^{-\left(\alpha d + \beta d^2\right)} \tag{2.2}$$

The exponent is the so called biological effect ε.

$$\varepsilon = -\ln S = \alpha \cdot d + \beta \cdot d^2 \tag{2.3}$$

The radiosensitivity parameters α (linear) and β (quadratic) define the slope of the survival curve. The radiobiological properties of cells are often described by an α/β -ratio. It is considered that small α/β -ratios correspond to late reacting, larger α/β -ratios to early reacting tissue types. Panel A of figure 2.2 shows two exemplary survival curves, one for a late reacting tissue type ($\alpha/\beta = 2$ Gy) and one for an early reacting tissue type ($\alpha/\beta = 20$ Gy).

The LQ model can be used to calculate fraction effects and to explain why tumor cells can be efficiently treated with radiation. Compared to normal tissue, tumor cells have a higher α/β -ratio and hence a less pronounced shoulder in the survival curve (figure 2.2, panel A). Choosing the right dose per fraction (around $d = 2$ Gy in the plotted case) allows to treat tumors with least affecting the normal tissue.

It is a general finding that high-LET radiation (particle therapy) achieves the same biological effect with lower dose than photons [6]. This leads to the concept of the relative biological effectiveness (RBE). As clinical experience is mostly based on photon (x-ray) therapy, the RBE is defined as the ratio of photon dose d_x to particle dose d_p yielding the same biological effect.

$$RBE = \left.\frac{d_x}{d_p}\right|_{\varepsilon = const} \tag{2.4}$$

Panel B of figure 2.2 shows the determination of RBE with exemplified survival curves for x-ray and carbon ion irradiation. Using the iso-effect criteria in equation (2.4) and the LQ formula of equation (2.3) for the RBE determination, it can be expressed with the following function.

$$RBE\left(\alpha_x, \beta_x, \alpha_p, \beta_p, d_p\right) = \frac{-\alpha_x + \sqrt{{\alpha_x}^2 + 4 d_p \beta_x \left(\alpha_p + \beta_p d_p\right)}}{2 d_p \beta_x} \tag{2.5}$$

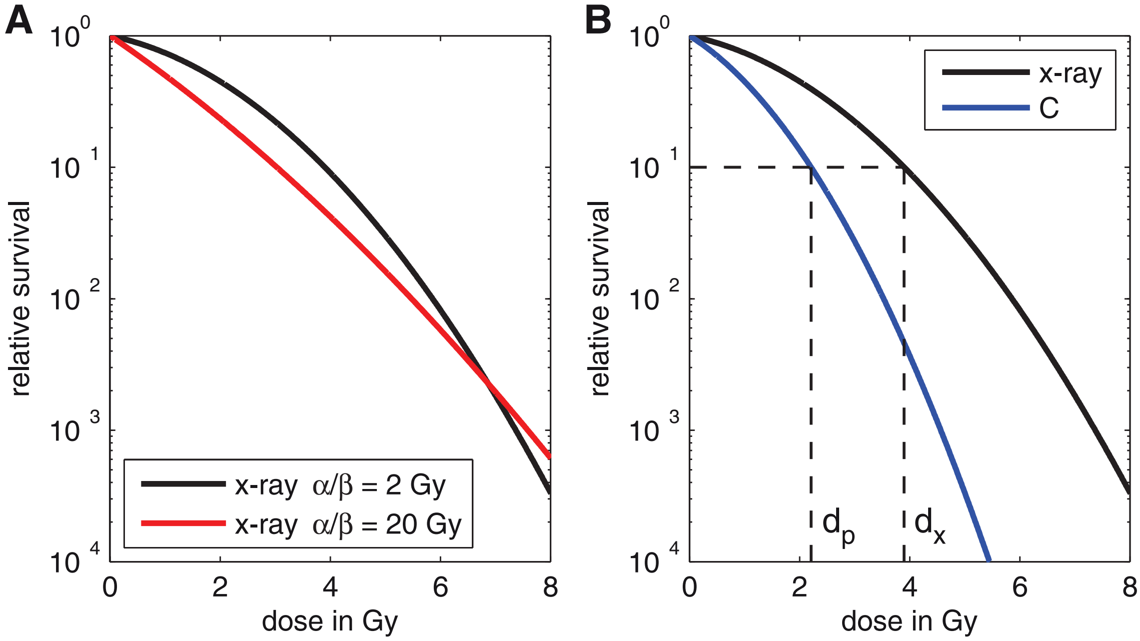

Figure 2.2.: Panel A shows cell survival curves for exemplary tumor tissue ($\alpha_x/\beta_x = 20$ Gy) and an exemplary normal tissue ($\alpha_x/\beta_x = 2$ Gy) irradiated with x-rays. The shoulder in the curve is more pronounced for smaller α_x/β_x. In panel B the cell survival curve for $\alpha_x/\beta_x = 2$ Gy for x-ray are compared to an example cell survival curve for carbon ion irradiation. The survival curve is steeper for carbon ions. The dashed lines show the determination of the $RBE = d_x/d_p$ at 10% survival level (cf. equation (2.4)).

The radiosensitivity parameters for particle radiation are not only dependent on cell properties, but also on the LET and hence on the energy of the particles. For proton therapy RBE values typically range between 1.0 and 1.3. A widely used approximation for proton therapy is to set RBE to a constant value of 1.1 [7]. For heavier ions such an approximation is not sufficient. As most of the cell survival data and clinical experience are obtained for photon irradiation, biological modeling is needed to predict RBE (or α_p and β_p) for ions based on photon parameters. Typical RBE values for carbon ion therapy range between 1.0 and 5.0 and are strongly dependent on the LET of the examined carbon ions and their fragments.

3. Uncertainties in Biological Dose Response Models

Treatment planning for carbon ion therapy is based on the interplay of physics and biology as described in the previous chapter. Achievement of sufficient tumor control and sparing of the normal tissue requires high accuracy in the delivered dose. Image guidance, Monte Carlo dose calculation and tracking are just a few examples for newly developed techniques that aim to reduce uncertainties in the dose application. In contrast to this increasing accuracy, state of the art carbon ion treatment planning systems do not account for biological uncertainties in the dose response modeling process. These uncertainties and their impact are assessed by physicians and medical physicists based on their experience. The various sources of the biological uncertainties are introduced in section 3.1.

To plan the treatment and predict its outcome, treatment planning for carbon ion radiotherapy considers the combination of the physical dose and the relative biological effectiveness (RBE, cf. section 2.3). The RBE reflects the biological modeling. Uncertainties in RBE calculation directly affect the treatment of patients as they might result in under- or overdosage and hence in potential treatment failure or normal tissue complications.

Up to now uncertainties in biological models have been examined only for simplified scenarios or the models themselves [8, 9]. A comprehensive uncertainty analysis based on real patient data has not been accomplished yet. This comprehensive analysis needs to include uncertainties in biological parameters and provide the possibility to analyze effects on treatment outcome. The objective of this thesis is to add biological uncertainties to carbon ion treatment planning and evaluation. A key task in this context is the clear visualization of the impact of biological uncertainties in treatment planning and evaluation.

3.1. Sources of Biological Uncertainties

There are numerous sources of uncertainty in the four radiosensitivity parameters (α_x, β_x, α_p and β_p, cf. equation (2.5) on page 9) used for describing the RBE within the framework of the linear-quadratic (LQ) model. In this section these sources are introduced. The investigation of the impact of the shown and discussed uncertainties on carbon ion treatment planning is the main objective of this thesis.

The first assumption on which biological modeling in radiotherapy relies is the LQ model itself. In carbon ion therapy treatment planning in general and throughout this thesis in particular it is assumed that the LQ model provides a sufficient framework for biological modeling. It is assumed that the calculation of $RBE\,(\alpha_x, \beta_x, \alpha_p, \beta_p, d_p)$ as it is described in equation (2.5) on page 9 represents the dose response relation. The uncertainties discussed here concern the used biological parameters α_x, β_x, α_p and β_p. Uncertainties associated with the mathematical description or validity of the LQ model itself are not considered.

The process of biological modeling in carbon ion therapy is difficult and complex, as biological quantities cannot be measured directly. In the following sections the biological uncertainties are classified in an application-oriented way. In the first section the uncertainties of measurable values are discussed. Those values are obtained from experiments. Their uncertainties can theoretically be reduced by better statistics or more precise measurements. In the second section a compilation of conceptual assumptions and extrapolations used in the biological response modeling of carbon ion therapy is presented. In the last case the uncertainties are not quantified yet. The examination of the relations requires additional development in the field of radiation biology.

3.1.1. Determination of the Used Biological Parameters and Their Uncertainties

RBE is calculated based on the radiosensitivity parameters (α_x and β_x) of the x-ray reference radiation and the same set (α_p and β_p) of the considered particle irradiation. Cell experiments with x-ray or ion beams facilitate the determination of the corresponding α and β. These experiments are done with cell cultures plated on culture dishes and are commonly characterized as *in vitro*. A precise description of these experiments can be found in literature (e.g. in chapter 3 of reference [10]).

The uncertainty in the cell experiment is approximated by a standard deviation of several repetitions of the same experiment. The number of independent but similar experiments is commonly below ten, due to the great experimental effort to provide the cells and evaluate their dose response. An increased number of repetitions could provide a better statistics and hence a smaller standard deviation.

Figure 3.1 shows an example of the result and the further proceeding of the described experiment with HEP3B (human hepatoma) cells irradiated with x-ray (panel A) and carbon ions (panel B) [11]. The dots indicate the experimental results. They are displayed together with the corresponding standard deviations (error bars). The LQ model parameters are obtained from a fit to the experimental data. The panels in figure 3.1 show two frequently used fitting methods. Within both approaches the function $-\alpha d - \beta d^2$ is fitted to the natural logarithm of the survival $\ln(S(d))$. This reflects the natural logarithm of equation (2.2) on page 9 describing the LQ model. The difference between the two fitting approaches is the relative weighting of the experimental data points. The standard fit (black lines in figure 3.1) assigns equal weights to all data points. The weighted fit (blue lines in figure 3.1) weights the different data points by the inverse of their relative standard deviations σ_{rel}. This relative standard deviation is obtained dividing the absolute standard deviation divided by the mean value. The weight $1/\sigma_{rel}$ increases the impact of data points with a low σ_{rel}. The influence of data points with large σ_{rel} is reduced.

The tables below the panels in figure 3.1 summarize the results of the two different fitting approaches. Although the difference of the resulting lines for both fits seems small, their resulting α and β have considerable deviations. The marked 68.3% (one sigma) confidence measure of both fitting approaches are large. These measures are commonly reported as uncertainties in α and β. Figure 3.2 shows a compilation of reported fitting results for α_p and β_p [12, 13]. α_p and β_p are shown together with their uncertainties (68.3% confidence level) for protons, helium and carbon ions of different energies (different LET values) for several cell lines. These values have large uncertainties. An additional issue is that the confidence values of the fit do not represent the standard deviations of the initial data points. If for instance the standard deviation of all data points in figure 3.1 would be doubled, both fitting results and their confidence values would not change.

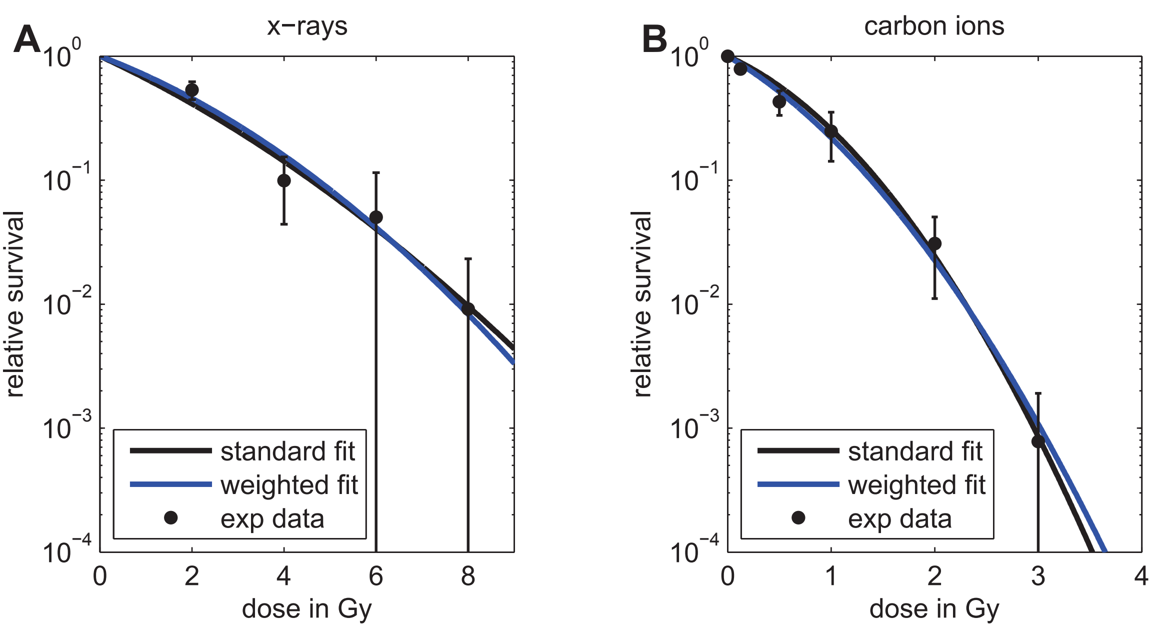

	α_x in Gy^{-1}	β_x in Gy^{-2}
standard fit	0.397 ± 0.129	0.023 ± 0.019
weighted fit	0.323 ± 0.123	0.034 ± 0.021

	α_p in Gy^{-1}	β_p in Gy^{-2}
standard fit	0.866 ± 0.236	0.496 ± 0.090
weighted fit	1.134 ± 0.338	0.382 ± 0.148

Figure 3.1.: Example of the result of a cell experiment and the fitting process. The mean values of the experimentally derived data points are shown together with the corresponding standard deviations. They are calculated from six independent repetitions of the same cell experiment. Panel A shows an example for x-ray, panel B for carbon ion irradiation. The results of two fitting approaches are shown: a standard approach with equal weights for all data points (black lines) and a weighted fitting approach (blue lines). Here the data points are weighted with the inverse of their relative standard deviation $1/\sigma_{rel}$. The fit result for the radiosensitivity parameters are summarized in the tables below the corresponding panels. The experimental data are courtesy of Daniel Habermehl [11].

Besides the irradiated cell type the radiosensitivity parameters for ions depend on the ion type and its linear energy transfer (LET): $\alpha_p(Z, LET)$ and $\beta_p(Z, LET)$. Theoretically it is possible to determine α_p and β_p for all needed ions as a function of LET with the above described experimental and fitting procedures. Practically the analysis is not feasible due to the extremely high amount of different combinations. Biological models are used instead to extrapolate the x-ray results α_x and β_x to $\alpha_p\left(Z, LET, \alpha_x, \beta_x\right)$ and $\beta_p\left(Z, LET, \alpha_x, \beta_x\right)$. Two biological models are used in this thesis. They are further discussed later in chapter 6. Both models depend on assumptions and parameters which introduce additional uncertainties in α_p and β_p. The predictions of these biological models are validated against experimentally derived α_p and β_p.

It can be concluded that uncertainties in biological parameters arise from α and β which are fitted with large confidence intervals to experimental data that have considerable error bars themselves. Additional biological models are needed to predict α_p and β_p. This modeling is based on assumptions and uncertain parameters and can only be validated against experimentally derived, hence inherently uncertain data.

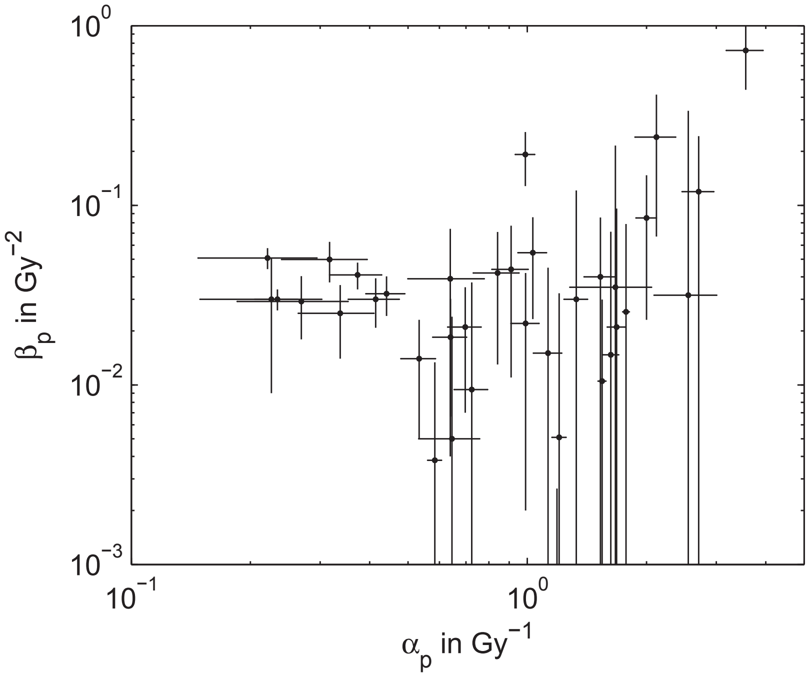

Figure 3.2.: LQ model radiosensitivity parameters α_p and β_p together with their uncertainties reported in literature. The values are taken from references [12, 13]. They were determined for a range of different cell lines, irradiation types (protons, helium and carbon ions) and energies. The figure demonstrates the considerable uncertainties in the radiation sensitivity parameters.

3.1.2. Potentially Uncertain Concepts in the Biological Modeling Process

The quantified uncertainties described in the previous section are not the only challenges in the biological modeling of carbon ions. In this section a compilation of additional arguments for uncertainties in carbon ion therapy is given. The human body is a very complex system and direct measurement of needed cell properties is currently not possible. This is why the below discussed characteristics are far from clinical implementation. In the routine day-to-day practice only the planned dose distribution is individualized, while the biological part of treatment planning is not personalized for every patient. Mean values of biological parameters obtained from a group of patients are used. The implementation of individual radiotherapy accounting for radiobiological properties is only possible if predictive assays are developed, determining the crucial biological factors. The here presented challenges are explained in detail in radiobiology literature (for instance reference [10]).

Biological parameters are obtained from cell experiments which can be done only *in vitro*. The challenge is to perform the transfer from these *in vitro* experiments to cells in the human body. Even if the possibility to successfully cultivate tumor or normal tissue cells of a patient is assumed, there are factors such as the immune system response or the oxygenation level that influence the dose response but cannot be exactly reproduced *in* *vitro*. This also includes the so-called bystander effect which appears between cells located in close proximity to each other.

A further challenge is the possibly high spatial variation of crucial biological factors for the dose response in the human body. In order to account for the spatial variations of for instance the oxygenation level, two consequent challenges need to be solved. First, the spatial distributions of the cell properties that influence dose response need to be obtained. The second challenge is the resolution. The properties might change from cell to cell (micrometer scale) whereas treatment planning is done based on computed tomography images with a resolution in the order of millimeters.

The research in the field of biological dose response behavior of cells inside the human body is not yet sufficient to include these potential sources of uncertainties in the analysis within the scope of this thesis. It is not known yet whether the relations and potential sources of uncertainty presented here can be included in the framework of the standard LQ model. It may be necessary to adapt or replace the model.

To improve carbon ion treatment planning the implementation of an uncertainty analysis is necessary. Including the quantified uncertainties discussed in section 3.1.1 is a first step. Though it is not yet possible to account for the entire set of radiobiological challenges mentioned in this section.

4. Structure and Outline

Following the introduction and the objective of this thesis presented in the previous chapters, the outline and structure of it is given here. Throughout this work, uncertainties in biological dose response modeling are implemented into carbon ion treatment planning and its evaluation. This is subdivided into six parts:

- Part I ("Introduction") summarizes the context of this work and states its objectives. Radiotherapy in general and carbon ion therapy in particular are introduced in chapter 1 and chapter 2 respectively. The sources of biological uncertainties are discussed in chapter 3. Outline and structure of this thesis are described here, in chapter 4.
- Part II ("Implementing Biological Optimization for Carbon Ion Therapy") deals with carbon ion treatment planning, optimization and their implementation into a treatment planning system. The physical beam model is described in chapter 5 followed by the used biological models and their implementation in chapter 6. Treatment plan optimization and evaluation are described in chapter 7.
- Part III ("Sensitivity Analysis") introduces different sensitivity analysis approaches. Throughout chapter 8 they are introduced along with their limitations and implementations tailored to biological uncertainties in carbon ion therapy. The developed visualization tools are introduced in section 8.5.
- Part IV ("Impact of Uncertainties in Biological Dose Response Models on Carbon Ion Treatment Plans") contains the result of the sensitivity analysis applied to carbon ion therapy. In chapter 9 the examined uncertainty settings are summarized. In the following chapter 10 the results for comprehensive sensitivity analyses are presented. Several partial sensitivity analyses are discussed in chapter 11. The partial sensitivity analysis considers only a subset of the comprehensive sensitivity analysis. The analysis of the tumor control probability is topic of chapter 12. A conclusion of the evaluations in this part of the thesis is given in chapter 13.
- Part V ("Summary and Conclusion") summarizes and concludes this thesis.
- Part VI ("Appendix") contains supplementary information and figures.

Part II.

Implementing Biological Optimization for Carbon Ion Therapy

In the following the methods to calculate and optimize dose and RBE-weighted dose (RWD) are described. Based on patient data, these methods are implemented in a research treatment planning system (TPS). The TPS is based on CERR (Computational Environment for Radiotherapy Research) [14]. CERR is an open source radiation therapy tool written in Matlab. It allows handling of computed tomography (CT) images, contouring of regions of interest, dose calculation for photons, treatment plan optimization and treatment plan analysis. The potential of CERR is extended by LAP-CERR (Laser Accelerated Proton - CERR) [15, 16]. In this context the capability to calculate dose distributions for protons and carbon ions is added to CERR. LAP-CERR is based on CERR version 4.0 beta 2 and primarily designed for dose calculation of laser accelerated protons. In the following chapters the extension of LAP-CERR to carbon ion therapy, including fragmentation, LET calculations, biological modeling and RWD-optimization is described. Please contact the author[*] for a version of the source code or further support.

In the next chapters the basic physical beam model (chapter 5) and used biological models (chapter 6) are introduced. In the course of this thesis, the repair-misrepair-fixation (RMF) model was combined for the first time with fragmentation spectra to predict RBE for carbon ions [17]. That is why we validated the RMF model predictions against experimentally measured cell survival data and commonly used biological models (cf. section 6.2 and 6.3). In chapter 7 the used optimization method and its' implementation is described.

---

[*] Contact Florian Kamp, florian.kamp@mytum.de

5. Physical Beam Model

5.1. Depth Dose Curves and d_{ij} -Matrix

The physical information of carbon ion beams is simulated with Monte Carlo (MC) algorithms and implemented into the dose calculation of CERR. The fragmentation spectra of the incident carbon ion beam are generated with the MC code FLUKA [18, 19] as described by Parodi *et al.* [20] but for a generic beamline. In total Parodi *et al.* provided a set of 32 carbon ion beams with energies ranging from 90 to 400 MeV/u in 10 MeV/u steps. This energy range covers treatment depths up to 27 cm in water with a mean distance of 0.8 cm between the single Bragg peaks. Here the fully ionized elements H, He, Li, Be, B and C are scored. Generated neutrons are not considered. The resulting fragmentation spectra are described as particle fluence $\Phi(z, Z, E)$ which depends on the depth z, the atomic number Z of the ion and its energy E [21]. Figure 5.1 panel A and B show an example of the simulated fragmentation spectra for an initial carbon ion beam energy of $E_0 = 350$ MeV/u. Due to fragmentation, the number of carbon ions decreases with increasing depth. At the depth of the Bragg peak, there is a steep drop in the number of carbon ions. Here they have lost all their energy and stopped. Protons and helium ions are the most prominent fragments and reach higher energies per nucleon (panel B).

Depth dose curves $D\left(z\right)$ are obtained using the fragmentation spectra and the stopping power *SP*. The preparation of the fragment spectra for the use in the TPS CERR was done with the help of Sarah Brüningk within the scope of her master thesis [22].

$$D\left(z\right) = \sum_{Z} \int_{0}^{\infty} \Phi\left(z, Z, E\right) \cdot SP\left(Z, E\right) \mathrm{d}E \tag{5.1}$$

Figure 5.1 panel C shows the percentage depth dose (pdd) curves for the initial carbon ion beam energy $E_0 = 350$ MeV/u and the contribution of the six considered ion types. The pdd curves are obtained by normalizing depth dose curves to the maximum of the total dose. Panel C has a logarithmic y-axis to highlight the contribution of the fragments. Besides the initial carbon ions, protons and helium ions have the highest contribution to dose, followed by boron ions. The total depth dose curve, as sum over the six curves (cf. equation (5.1)), is plotted with a linear y-axis in panel D, showing the steep Bragg peak and the fragmentation tail.

The lateral spread $\sigma(z)$ without an initial width of the carbon ion beam is plotted in panel E. The lateral information for this work is gained via interpolation of a lateral spread database to the simulated initial carbon energies. The database was previously simulated with the MC code Geant4 [23]. The lateral spread increases to a maximum of $\sigma\left(z\right) = 2$ mm at the depth of the Bragg peak of the highest tabulated energy (400 MeV/u). In general higher initial energy results in a deeper Bragg peak and larger maximum lateral spread. The small $\sigma\left(z\right)$ facilitates very steep lateral dose gradients. This is one of the rationales for carbon ion therapy (cf. chapter 2 on page 7). The increase of the lateral spread in the fragmentation tail, distal to the Bragg peak is caused by the lighter fragments. In the database [23] the lateral spread is approximated by Gaussian functions. To evaluate and demonstrate the impact of biological uncertainties in a TPS, the lateral beam modeling by one Gaussian is sufficient.

For protons a spot-scanning, Pencil Beam (PB) algorithm was implemented in (LAP-) CERR by Stefan Schell [16, 15]. Within this thesis, I extended LAP-CERR to carbon ions and their fragmentation spectra. In the implemented approach the dose distribution of one spot of a PB can be described as function of $D(z)$ and $\sigma(z)$. An initial spread of the PB can be included in $\sigma(z)$.

$$D\left(x,y,z\right) = \frac{D\left(z\right)}{2\pi\,\sigma^2(z)} exp\left(-\frac{1}{2}\frac{x^2+y^2}{\sigma^2(z)}\right) \tag{5.2}$$

Here, $\sigma(z)$ is not dependent on x and y. z is the beam direction while x and y are the two lateral directions. There are drawbacks related to the PB algorithm, for instance in case inhomogeneous structures are present [24]. Neither the lateral spread nor the fragmentation spectra include the necessary information to account for inhomogeneous structures. The uncertainty caused by this is not considered in the evaluation of the biological uncertainties.

Necessary spots in between the 32 initial carbon ion beam energies, are implemented by a simplified range shifter. It shifts the next Bragg peak with higher energy to the desired depth. The treatment plan optimization is based on a d_{ij} matrix which contains the complete dose information for every voxel i for every spot j. A spot can have its own set of position and initial beam energy. One entry in d_{ij} represents the dose in voxel i by a normalized spot j. Multiplying d_{ij} by a weights vector ω results in the dose distribution in every voxel $d_i = \sum_j d_{ij} \cdot \omega_j$. Note, that d is used instead of D, indicating a dose per fraction. Further details about the PB algorithm and the construction of the d_{ij} matrix can be found in references [16, 25].

5.2. LET and LET_{ij}- Matrix

The dose-weighted LET is calculated by combining the fragmentation spectra and the corresponding stopping powers (cf. equation (2.1)).

$$\mathit{LET}\left(z\right) = \frac{\sum_Z \int_0^\infty \Phi\left(z,Z,E\right) \cdot \left(\mathit{SP}\left(Z,E\right)\right)^2 \mathrm{d}E}{\sum_Z \int_0^\infty \Phi\left(z,Z,E\right) \cdot \mathit{SP}\left(Z,E\right) \mathrm{d}E} \tag{5.3}$$

The $\mathit{LET}(z)$ curves are tabulated for all 32 initial carbon ion beam energies. Figure 5.2 shows the (total) LET for $E_0 = 350$ MeV/u together with the contributions of the fragmentation ions. Up to some millimeters distal to the Bragg peak ($z_{Bragg} = 21.9$ cm) the carbon ions are the crucial contribution to the total LET. Nevertheless, the lower LET fragmentation ions result in a noteworthy lower total LET. With further depth, distal to the Bragg peak, there are no carbon ions left and LET decreases in a first big step. Then it continuously declines with decreasing number of high-LET ions (compare to the depth dose relations and relative particle numbers in figure 5.1).

Similar to the d_{ij} approach a LET_{ij} matrix is implemented in the TPS, allowing the fast calculation of dose-weighted LET maps. The LET distribution lateral to the central axes is assumed to be constant at the value of the central axes ($\mathit{LET}(x,y,z) = \mathit{LET}(z)$ for any x, y combination). The uncertainty caused by this is not considered in the evaluation of the biological uncertainties.

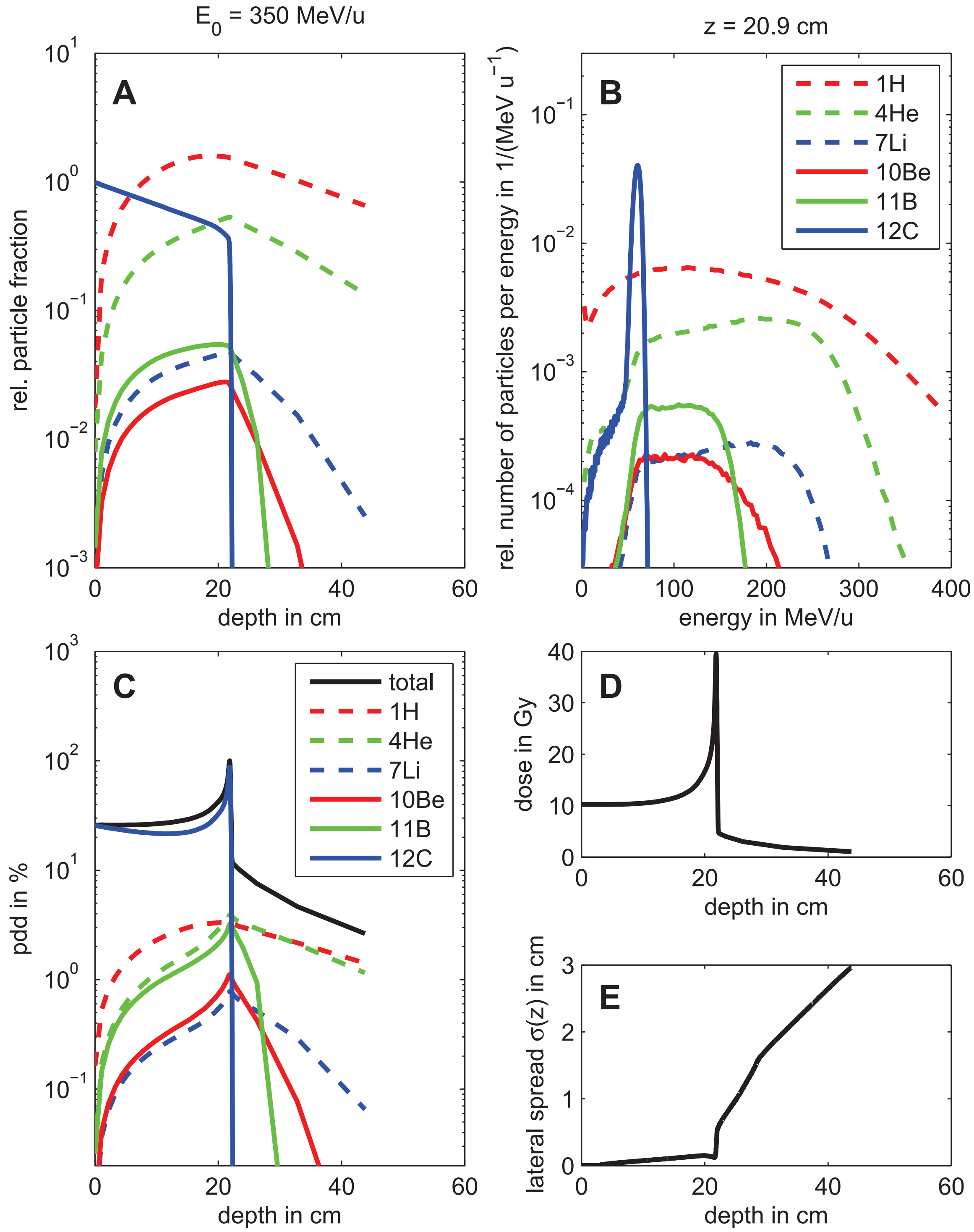

Figure 5.1.: Exemplary fragmentation spectra, corresponding depth dose curves and fitted lateral spread for an initial carbon ion energy of $E_0 = 350$ MeV/u. Panel A shows the relative occurrence of different ion types (The legend of panel A can be found in panel B). Panel B shows the fragmentation spectra in a depth of $z = 20.9$ cm close to the Bragg peak. In panel C the percentage depth dose (pdd) curve including the contribution of different fragments is displayed with a logarithmic y-axis. The data is completed by the total depth dose curve with a linear y-axis (panel D) and the lateral spread (panel E).

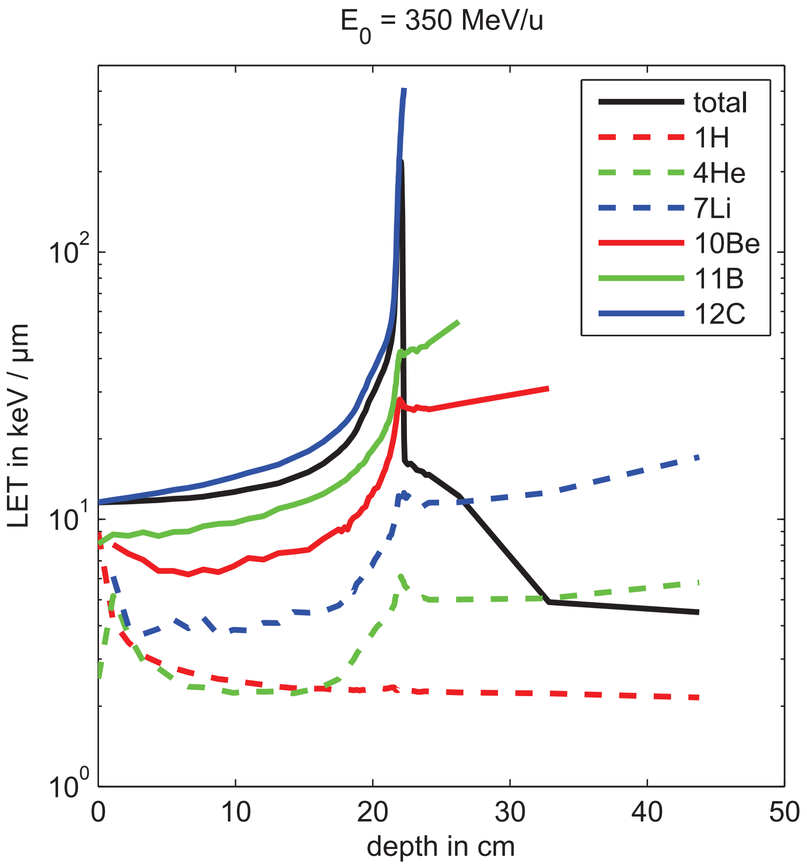

Figure 5.2.: Depth dependency of dose-weighted LET distributions for carbon ions with $E_0 = 350$ MeV/u. The total LET as well as the contributions of the different fragmentation ions are displayed. The Bragg peak lies in a depth of 21.9 cm. The corresponding depth dose relations for the different ions are displayed in figure 5.1 panel C on page 25.

6. Biological Models and their Implementation

In carbon ion therapy, treatment planning must include physical beam properties such as absorbed dose, LET and nuclear fragmentation, as well as differences in the relative biological effectiveness (RBE) of ions compared to photons. In ion therapy RBE or the radiosensitivity parameters α and β, which are needed to calculate RBE (cf. equation (2.5)) are dependent on the irradiated cell itself, then on ion type and energy. Due to the nuclear fragmentation of the carbon ion beam there are several different ion types present. The energy spectra of these ion types change with depth (cf. figure 5.1 on page 25). The number of possible combinations for cell experiments is hence too high to perform them systematically for all needed ions and their different energies. Consequently biological models are needed to estimate RBE for treatment plan optimization and evaluation. Within the framework of the LQ model (cf. section 2.3), several biological models have been developed to predict changes in α and β as a function of particle type and energy, assuming a set of x-ray reference parameters. As most of clinical experience and biological experiments are obtained with x-rays, they are used as reference radiation.

Two biological models are used in this work: the local effect model (LEM) and the repair-misrepair-fixation (RMF) model. These models and their implementation are presented in the following chapter. The RMF model has not been combined with fragmentation spectra or implemented in a TPS before. Therefore the model predictions are compared to other models and to *in vitro* measured data, based on cell survival experiments. The implementation of the RMF model into carbon ion treatment planning as well as the comparisons, mentioned above, have recently been summarized in a paper which was submitted in December 2014 [17]. The LEM was chosen because it is actually used in patient treatment at the HIT (Heidelberger Ionenstrahl-Therapiezentrum). The RMF model was chosen because it is very fast and thus provides the possibility to perform a comprehensive sensitivity analysis, as described later on in this work.

6.1. Local Effect Model (LEM)

6.1.1. Basic Concept

The local effect model (LEM) has been developed to predict cell survival after charged particle irradiation [26, 27]. Besides the x-ray radiosensitivity parameters, the model is based on several further considerations. One of the main features (cf. reference [28], page 230) is a threshold dose, above which the LQ model becomes purely linear. This is needed because the photon response curve is extrapolated to very high local doses, prominent in high-LET radiation. Then, the radial track structure of deposited dose is parametrized on a sub-µm scale. In addition the critical target (e.g. the cell nucleus) is modeled as a cylinder. The distribution of the particle tracks over the target structure is simulated with a Monte Carlo algorithm. The obtained local dose deposition in the target structure is then converted to a dose and a probability of cell survival. This leads to a survival curve to which α_p and β_p are fitted.

There have been several improvements on the original LEM1 version (LEM2-4). For a more detailed overview see Grün *et al.* [29] and references therein. Within the scope of this thesis the LEM1 is implemented into CERR. LEM1 is the only version which is currently implemented in clinical routine [30]. For comparison with other biological models, LEM4 [31] results, published in [29], are used as well.

6.1.2. Implementation

The dependencies of α_p and β_p on the ion type and energy are taken from the LEM implementations by INFN (Istituto Nazionale di Fisica Nucleare) and I-SEE (Internet - Simulation, Evaluation, Envision) which are available online* [32]. There, tabulated LEM1 data sets are available for different cell lines (α_x and β_x). Following Zaider and Rossi [33], dose-weighted $\alpha_p(z)$ and $\beta_p(z)$ can be calculated for each cell line by integrating over the fragmentation spectra:

$$\alpha_p(z) = \frac{\sum_Z \int_0^\infty \alpha_p(z,Z,E) \cdot \mathit{\Phi}(z,Z,E) \cdot \mathit{SP}(Z,E)\,\mathrm{d}E}{\sum_Z \int_0^\infty \mathit{\Phi}(z,Z,E) \cdot \mathit{SP}(Z,E)\,\mathrm{d}E} \tag{6.1}$$

$$\sqrt{\beta_p(z)} = \frac{\sum_Z \int_0^\infty \sqrt{\beta_p(z,Z,E)} \cdot \mathit{\Phi}(z,Z,E) \cdot \mathit{SP}(Z,E)\,\mathrm{d}E}{\sum_Z \int_0^\infty \mathit{\Phi}(z,Z,E) \cdot \mathit{SP}(Z,E)\,\mathrm{d}E} \tag{6.2}$$

The depth dependencies according to equations (6.1) and (6.2) are pre-calculated for all 32 carbon ion beam energies and needed cell lines and tabulated. For carbon ion treatment optimization two matrices $\alpha_{p,ij}$ and $\beta_{p,ij}$ are constructed similar to the d_{ij} matrix. These matrices contain the contribution of spot j to the voxel i.

6.2. Repair-Misrepair-Fixation (RMF) Model

6.2.1. Basic Concept

The repair-misrepair-fixation (RMF) model was developed and evaluated by Carlson *et al.* [12] as a mechanistic approach, linking reproductive cell death by mitotic catastrophe, apoptosis, or other cell death modes to double-strand break (DSB) induction and processing. Carlson *et al.* [12] and Frese *et al.* [34] showed how to determine the linear α and the quadratic β term of the LQ model for a given radiation quality, using DSB induction (Σ) and the frequency-mean specific energy ($\bar{z}_F$).

$$\alpha = \frac{\Sigma}{\Sigma_x}\left[\alpha_x + 2\frac{\beta_x}{\Sigma_x}\left(\Sigma \cdot \bar{z}_F - \Sigma_x \cdot \bar{z}_{F_x}\right)\right] \tag{6.3}$$

$$\beta = \left(\frac{\Sigma}{\Sigma_x}\right)^2 \beta_x \tag{6.4}$$

---

[*] *http://totlxl.to.infn.it/lem*

The initial number of DSB per Gy per giga-base-pair is derived from the Monte Carlo Damage Simulation (MCDS) [35, 36]. In the MCDS, Σ is only dependent on the physical property [37],

$$\frac{Z_{\mathit{eff}}^2}{\beta_v^2} = \frac{Z^2}{\beta_v^2}\left[1 - exp\left(-125 \cdot \beta_v \cdot Z^{-\frac{2}{3}}\right)\right] \tag{6.5}$$

where Z_{eff} is the effective ion charge and β_v is the velocity of the ion divided by the speed of light in vacuum. This is a key feature of the RMF model, resulting in one $(Z_{\mathit{eff}}/\beta_v)^2$ - Σ table describing the DSB induction for all relevant ions and their energies. The second variable depending on the radiation quality is $\bar{z}_F$, which can be approximated as

$$\bar{z}_F = 0.204\frac{SP}{d_C^2} \tag{6.6}$$

with the stopping power SP and d_C the diameter of a spherical water target, representing the cell. Here $d_C =$ 5 µm is used as it was done by Carlson *et al.* [12]. The x-ray reference radiation is modeled by its spectrum of secondary electrons. An electron spectrum of a Cobalt-60 source is provided at MCDS homepage† [38]. A complementary MCDS run for the generation of the used Σ lookup table lasts approximately 2 h on a 2.66 GHz dual-core work station. In this work, MCDS version 3.10 is used. It provides an improvement of the $\bar{z}_F$ approximation for high stopping powers [39], which had no impact on the here presented results.

6.2.2. Implementation

The structure of the RMF model allows an adapted, faster way to calculate α_p and β_p for different cell lines (characterized here by α_x and β_x). Inserting equations (6.3) and (6.4) in equations (6.1) and (6.2), α_x and β_x can be factored out.

$$\begin{aligned}
\alpha_p(z) = {} & \alpha_x \frac{\sum_Z \int_0^\infty \left[\frac{\Sigma(z,Z,E)}{\Sigma_x}\right] \mathit{\Phi}(z,Z,E) \cdot SP(Z,E)\,\mathrm{d}E}{\sum_Z \int_0^\infty \mathit{\Phi}(z,Z,E) \cdot SP(Z,E)\,\mathrm{d}E} \\
& + \beta_x \frac{\sum_Z \int_0^\infty \left[2\frac{\Sigma^2(z,Z,E)}{\Sigma_x^2} \cdot \bar{z}_F\right] \mathit{\Phi}(z,Z,E) \cdot SP(Z,E)\,\mathrm{d}E}{\sum_Z \int_0^\infty \mathit{\Phi}(z,Z,E) \cdot SP(Z,E)\,\mathrm{d}E} \\
& - \beta_x \frac{\sum_Z \int_0^\infty \left[2\frac{\Sigma(z,Z,E)}{\Sigma_x} \cdot \bar{z}_{F_x}\right] \mathit{\Phi}(z,Z,E) \cdot SP(Z,E)\,\mathrm{d}E}{\sum_Z \int_0^\infty \mathit{\Phi}(z,Z,E) \cdot SP(Z,E)\,\mathrm{d}E} \\
& = \alpha_x \cdot c_1(z) + \beta_x \cdot c_2(z)
\end{aligned} \tag{6.7}$$

$$\begin{aligned}
\sqrt{\beta_p(z)} & = \frac{\sum_Z \int_0^\infty \left[\sqrt{\beta_x} \cdot \frac{\Sigma(z,Z,E)}{\Sigma_x}\right] \mathit{\Phi}(z,Z,E) \cdot SP(Z,E)\,\mathrm{d}E}{\sum_Z \int_0^\infty \mathit{\Phi}(z,Z,E) \cdot SP(Z,E)\,\mathrm{d}E} \\
& = \sqrt{\beta_x} \cdot c_1(z)
\end{aligned} \tag{6.8}$$

---

† *http://faculty.washington.edu/trawets/mcds*

This allows to tabulate only $c_1(z)$ and $c_2(z)$ for the RMF model. Any desired α_x, β_x combination can be chosen still after the ray tracing, when the ij-matrices are already constructed. This leads to the concept of $c_{1,ij}$ and $c_{2,ij}$ within the RMF model.

Please note the further step in section 7.1, equations (7.5) - (7.8), where it is shown that α_x and β_x can be still changed after the optimization using the RMF model. The calculation of a new set of α_p and β_p based on changes in α_x and β_x is hence very fast. Another advantage of the RMF model is that RBE (cf. equation (2.5)) is only a function of α_x/β_x and not α_x and β_x (cf. reference [34], equation (17))

$$RBE_{RMF}\left(\frac{\alpha_x}{\beta_x}, c_1, c_2, d\right) = \frac{1}{2d} \cdot \left(-\frac{\alpha_x}{\beta_x} + \sqrt{\left(\frac{\alpha_x}{\beta_x}\right)^2 + 4d\left(c_1\frac{\alpha_x}{\beta_x} + c_2 + c_1^2 d\right)}\right). \tag{6.9}$$

6.2.3. Validation of RMF Model Predictions against a Cell Survival Database

In contrast to the LEM, the RMF model has not been used in three-dimensional ion treatment planning before. To validate the use of the RMF model for carbon ion therapy, the model predictions are compared to published, experimentally derived values [17]. The Particle Irradiation Data Ensemble (PIDE)‡ [40] provides a compilation of α and β values, fitted to cell survival curves for ions and reference x-rays. PIDE version 2.0 released in September 2013 is used. In contrast to the evaluation by Frese *et al.* [34], who compared α_p and β_p values as function of LET to *in vitro* results, RBE values at two survival levels are compared. The low dose limit RBE_α and $RBE(S = 10\%)$ are evaluated here. Figure 6.1 shows the comparison of protons (panel A and B) and carbon ions (panel C and D). Protons are chosen because they are the most prominent fragmentation ions. Panel A and C show the simplified zero dose limit, where RBE reduces to $RBE = \alpha_p/\alpha_x$. Using the RMF model (equations (6.3) and (6.4)), the hyperbolas describing the RMF model results can be calculated as a function of α_x/β_x.

$$RBE_\alpha = \frac{\alpha_p}{\alpha_x} = \frac{\Sigma}{\Sigma_x} + 2\left(\frac{\Sigma^2}{\Sigma_x^2} \cdot \bar{z}_F - \frac{\Sigma}{\Sigma_x} \cdot \bar{z}_{F,x}\right)\left(\frac{\alpha_x}{\beta_x}\right)^{-1} \tag{6.10}$$

Instead of the integrals in equation (6.7), the DSB induction Σ can be used as monoenergetic protons and carbon ions are evaluated.

Figure 6.1 illustrates that the RMF model is able to predict quantitative and qualitative trends in ion RBE. Higher LET results in higher RBE. Additionally, the value of RBE declines with increasing α_x/β_x. This observation is valid for RBE_α as well as $RBE(S = 10\%)$. The RBE for carbon ions is much higher than RBE for protons. The described relations are more pronounced for carbon ions, but do have the same trend for protons. The RBE of further ions ($Z = 2...5$) contained in the fragmentation spectra lie in between protons and carbon ions. RBE_α shows a higher dependency on α_x/β_x.

RMF model based RBE predictions for carbon ions change from $RBE_\alpha = 17$ to 3.6 (LET = 130 keV/µm) or 7 to 2.5 (LET = 70 keV/µm) in the evaluated α_x/β_x range. There is only a slight decrease in RBE at 10% survival level: 3.6 to 3.3 and 2.42 to 2.33 for LET = 130 keV/µm and 70 keV/µm respectively. For protons this effect is smaller, ranging from $RBE_\alpha = 3.12$ to 1.92 (LET = 24 keV/µm) or 1.4 to 1.26 (LET = 8 keV/µm).

---

‡ *https://www.gsi.de/bio-pide*

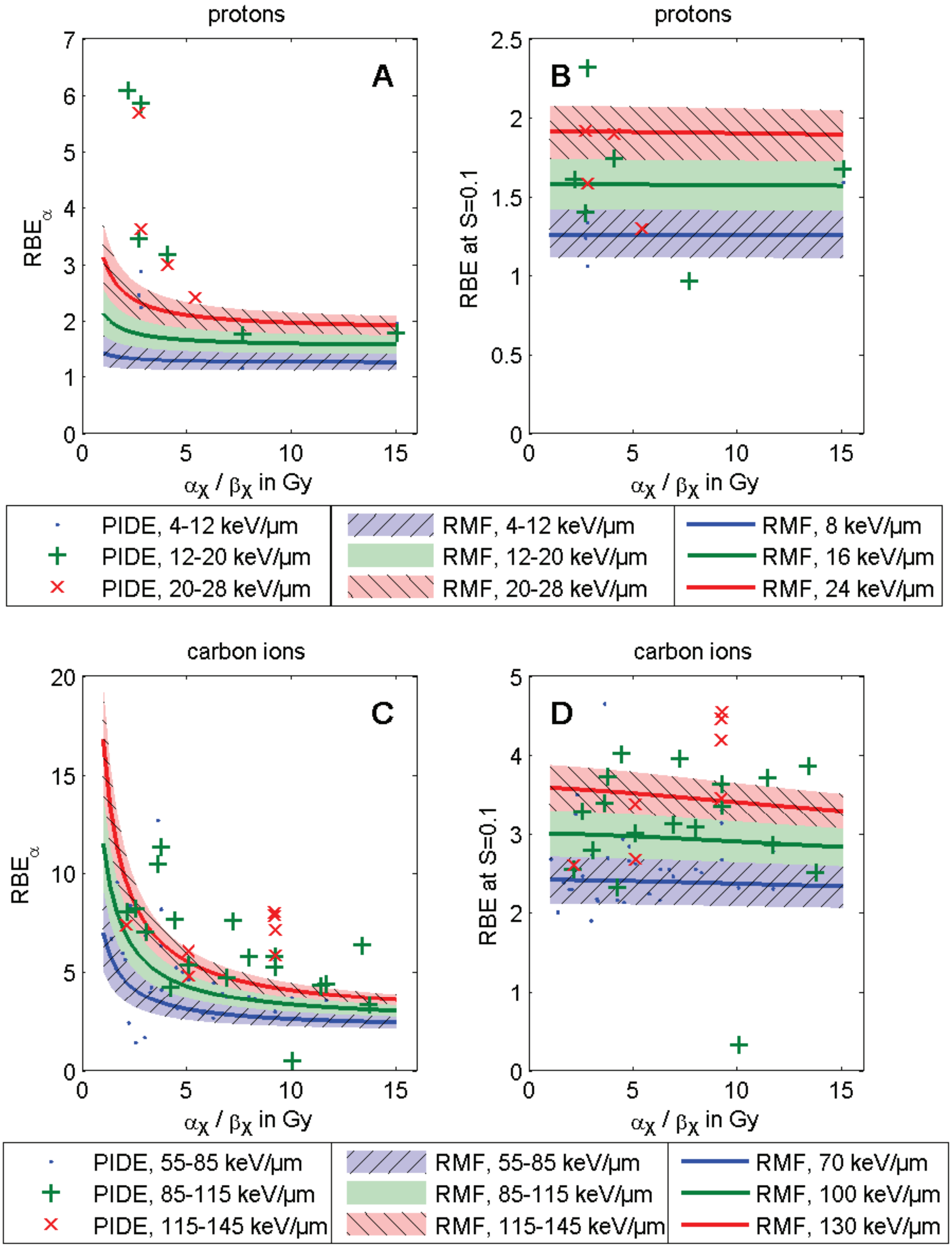

Figure 6.1.: Comparison of RMF model predictions with experimentally derived values reported by multiple institutions (PIDE data base) for RBE values of two biological endpoints (panel A and C: RBE$_\alpha$, panel B and D: RBE at a survival $S = 10\%$ for protons and carbon ions respectively) and a range of linear energy transfer (LET) and α_x/β_x values.

For the presented proton LET ranges, the RBE at 10% survival is quasi constant over the plotted α_x/β_x range. The values are RBE = 1.9 for LET = 24 keV/µm and RBE = 1.3 for 8 keV/µm respectively.

In the framework of the RMF model, the displayed relations depend only on α_x/β_x (cf. equation (6.9)). This means if one specific LET and survival level is considered, two cell lines with equal α_x/β_x have the same RBE value.

Error bars are not reported in the PIDE database. They are in general large and represent a main challenge for biological modeling. This affects both, LEM and RMF model predictions. The error bars and the basic issue of taking the step from *in vitro* cell experiments to cell response inside the human body, represent the rationales of this thesis. This key topic is subject of chapter 3.

6.2.4. Combining Fragmentation Spectra with the RMF Model

In order to evaluate the impact of the fragmentation on RBE predictions three different approaches are compared: FLUKA-simulated spectra with and without fragmentation and the analytical approach without fragmentation used by Frese *et al.* [34]. This work was accomplished in collaboration with David J. Carlson, Katia Parodi, Gonzalo Cabal and Andrea Mairani [17]. Figure 6.2 shows the impact of the fragmentation spectra on RWD for two different $\alpha_x/\beta_x = 2$ and 10 Gy for a one-dimensional spread-out Bragg peak (SOBP) covering a 5 cm target, from 10 to 15 cm depth in water. A constant dose $d = 1$ Gy was optimized for panel A and B. In addition, a constant RWD of 3 Gy(RBE) is shown in panel C and D. The inclusion of fragmentation spectra reduces the predicted RWD, particularly in the distal part of the SOBP. Table 6.1 shows the reduction of the RBE values for different dose levels ranging from 0.1 to 10 Gy, comparing the FLUKA spectra with and without fragmentation for the proximal edge ($z = 10$ cm), distal edge ($z = 15$ cm) and the mean value across the entire SOBP. Panels C and D in figure 6.2 illustrate the physical dose, which is needed to obtain a uniform biological effect of 3 Gy(RBE) within the SOPB. If nuclear fragments are neglected in the simulation, the estimated physical dose required to obtain a constant RWD may be underestimated. For the here used 5 cm SOBP this is by up to 33% for $\alpha_x/\beta_x = 2$ Gy and 24% for $\alpha_x/\beta_x = 10$ Gy respectively (panel C and D). The highest underestimations occur in the distal part of the SOBP. Without fragmentation a dose of 0.36 Gy is needed instead of 0.54 Gy with fragmentation for $\alpha_x/\beta_x = 2$ Gy. The corresponding dose values for $\alpha_x/\beta_x = 10$ Gy are $d = 0.60$ Gy without and $d = 0.79$ Gy with fragmentation.

If fragmentation spectra are included, the absolute value of RBE reduces. Similar evaluations for different treatment depths and target sizes are quantitatively and qualitatively consistent. The reduction is the largest where the number of fragments is the highest (close to the distal part of the SOBP). The potential RBE over prediction of the RMF model at the distal edge of a carbon ion SOBP, as reported by Frese *et al.* [34], is less prominent.

Figure 6.2 and table 6.1 furthermore show good agreement of the analytical implementation and the FLUKA spectra without fragmentation. The approximation done by Frese *et al.* [34] matches with the Monte Carlo results (differences smaller than 10%). This comparison to published data is the reason for choosing a one-dimensional SOBP in this part of the work.

RBE($\alpha_x/\beta_x = 2$ Gy)

	Proximal			Distal			Average		
dose in Gy	anal. w/o Frag.	MC w/o Frag.	MC Frag.	anal. w/o Frag.	MC w/o Frag.	MC Frag.	anal. w/o Frag.	MC w/o Frag.	MC Frag.
0.1	2.17	2.04	2.01	10.75	9.74	8.37	4.42	4.12	3.75
0.5	1.93	1.84	1.80	6.71	6.22	5.48	3.28	3.12	2.90
1	1.80	1.74	1.70	5.34	5.01	4.45	2.81	2.71	2.53
2	1.64	1.63	1.59	4.36	4.12	3.67	2.43	2.37	2.22
5	1.53	1.54	1.51	3.45	3.34	2.99	2.10	2.07	1.95
10	1.49	1.51	1.47	3.04	3.00	2.69	1.95	1.95	1.84

RBE($\alpha_x/\beta_x = 10$ Gy)

	Proximal			Distal			Average		
dose in Gy	anal. w/o Frag.	MC w/o Frag.	MC Frag.	anal. w/o Frag.	MC w/o Frag.	MC Frag.	anal. w/o Frag.	MC w/o Frag.	MC Frag.
0.1	1.64	1.61	1.58	5.02	4.73	4.06	2.46	2.39	2.22
0.5	1.63	1.59	1.56	4.53	4.30	3.75	2.36	2.30	2.15
1	1.61	1.58	1.54	4.15	3.98	3.50	2.28	2.23	2.08
2	1.55	1.55	1.52	3.77	3.63	3.21	2.17	2.13	2.00
5	1.50	1.52	1.48	3.27	3.19	2.85	2.02	2.00	1.89
10	1.48	1.50	1.46	2.98	2.95	2.64	1.93	1.92	1.82

Table 6.1.: RBE values for a range of physical doses and α_x/β_x values. RBE estimations of the analytical model without fragmentation as published by Frese *et al.* [34] can be compared to estimations using the MC spectra with and without fragmentation. The RBE values are shown for the proximal edge ($z = 10$ cm), the distal edge ($z = 15$ cm) and the mean from 10-15 cm (compare to figure 6.2, upper row).

6.3. Comparison of RMF Model Predictions to LEM Predictions

We compared LEM1 predictions to RMF model predictions for two different cell lines, one with a small α_x/β_x ratio of 2 Gy ($\alpha_x = 0.1$ Gy^{-1}, $\beta_x = 0.05$ Gy^{-2} as used for chordoma of the skull base, [30]) and a second with a higher ratio $\alpha_x/\beta_x = 9.2$ Gy ($\alpha_x = 0.184$ Gy^{-1}, $\beta_x = 0.02$ Gy^{-2} for Chinese hamster fibroblast, V79 [41]). Tabulated LEM1 data for both cell lines are provided online by the INFN/I-SEE project. Figure 6.3 illustrates the comparison in a simplified one-dimensional geometry, similar to figure 6.2 (cf. Kamp *et al.* [17]). Both models were implemented using the FLUKA generated fragmentation spectra.

In panels A and B RBE predictions for the LEM1(RBE_{LEM1}) and the RMF model (RBE_{RMF}) can be compared. For $\alpha_x/\beta_x = 2$ Gy and a constant physical dose of 0.5 and 2 Gy, RBE_{RMF} lies below RBE_{LEM1} in the entrance region (-58% and -40% for $d = 0.5$ and 2 Gy) and the proximal part (-48% and -30%) of the target. On the distal edge, RBE_{RMF} values rise above the RBE_{LEM1} values (+23% and +38%). For the higher $\alpha_x/\beta_x = 9.2$ Gy RBE_{RMF} is close to to RBE_{LEM1} (-10% and -5%) in the entrance region, approximately the same in the proximal part of the SOBP and lies above it in the distal part (+60% and +66%). The same behavior is observed for those plans that are optimized on constant RBE_{LEM1} and then recalculated with the RMF model, keeping d constant at the LEM1 optimization result. The difference between RBE_{RMF} and RBE_{LEM1} ranges from -58% over

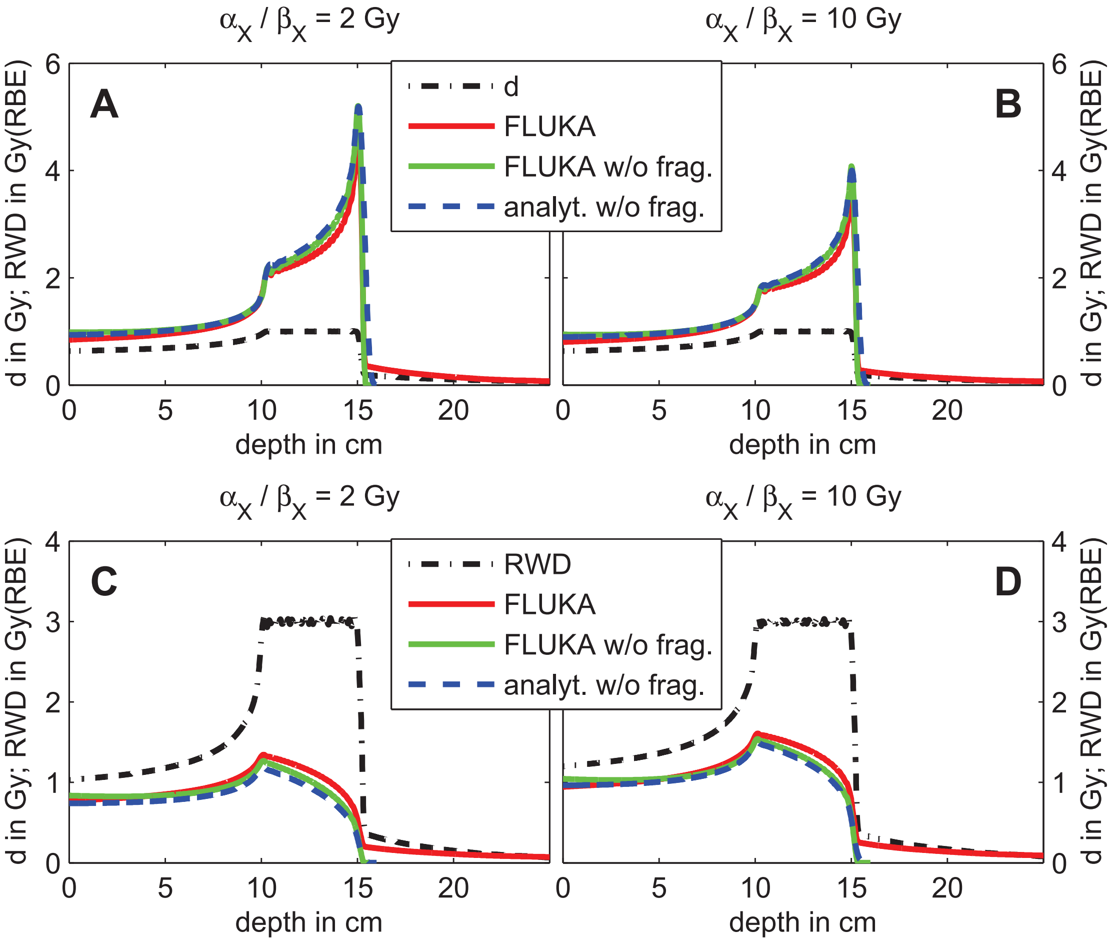

Figure 6.2.: Comparison of RMF model predictions of RWD for a SOBP in one dimension with and without FLUKA-generated nuclear fragments and an analytical approach without fragmentation implemented by Frese *et al.* [34]. The comparison is shown for two assumed $\alpha_x/\beta_x = 2$ and 10 Gy (left and right panels respectively). SOBPs were optimized for a target in water at a depth of 10-15 cm for a physical dose of 1 Gy (panels A and B) and a RWD of 3 Gy(RBE) (panels C and D).

-43% to +24% (entrance, proximal, distal) for $\alpha_x/\beta_x = 2$ Gy and -9% over -3% to +60% respectively for $\alpha_x/\beta_x = 9.2$ Gy. The changes are less prominent in the two fields cases (panel E and F), because high LET regions from one field average each other out with the low LET regions of the second field. The trends for $\alpha_x/\beta_x = 2$ Gy in figure 6.3 (smaller RBE in the entrance region, and the proximal part of the target and higher RBE in the distal part of the target) resemble the figures reported by Grün *et al.* [29] obtained in a 3-D geometry. Similar to their LEM1/LEM4 comparison for chordoma ($\alpha_x = 0.1$ Gy^{-1}, $\beta_x = 0.05$ Gy^{-2}), we optimized a spherical target, with 6 cm diameter located at $z = 7$ to 13 cm depth in water. Here, plans are optimized on constant physical dose for five different dose levels, ranging from 0.5 to 10 Gy for one field. The RBE is evaluated for the LEM1 and the RMF model. Table 6.2 shows the results for the proximal edge, distal edge, and mean RBE in the sphere for the FLUKA-RMF implementation, our FLUKA-LEM1 combination and the results for LEM1 and LEM4 reported by Grün *et al.* [29].

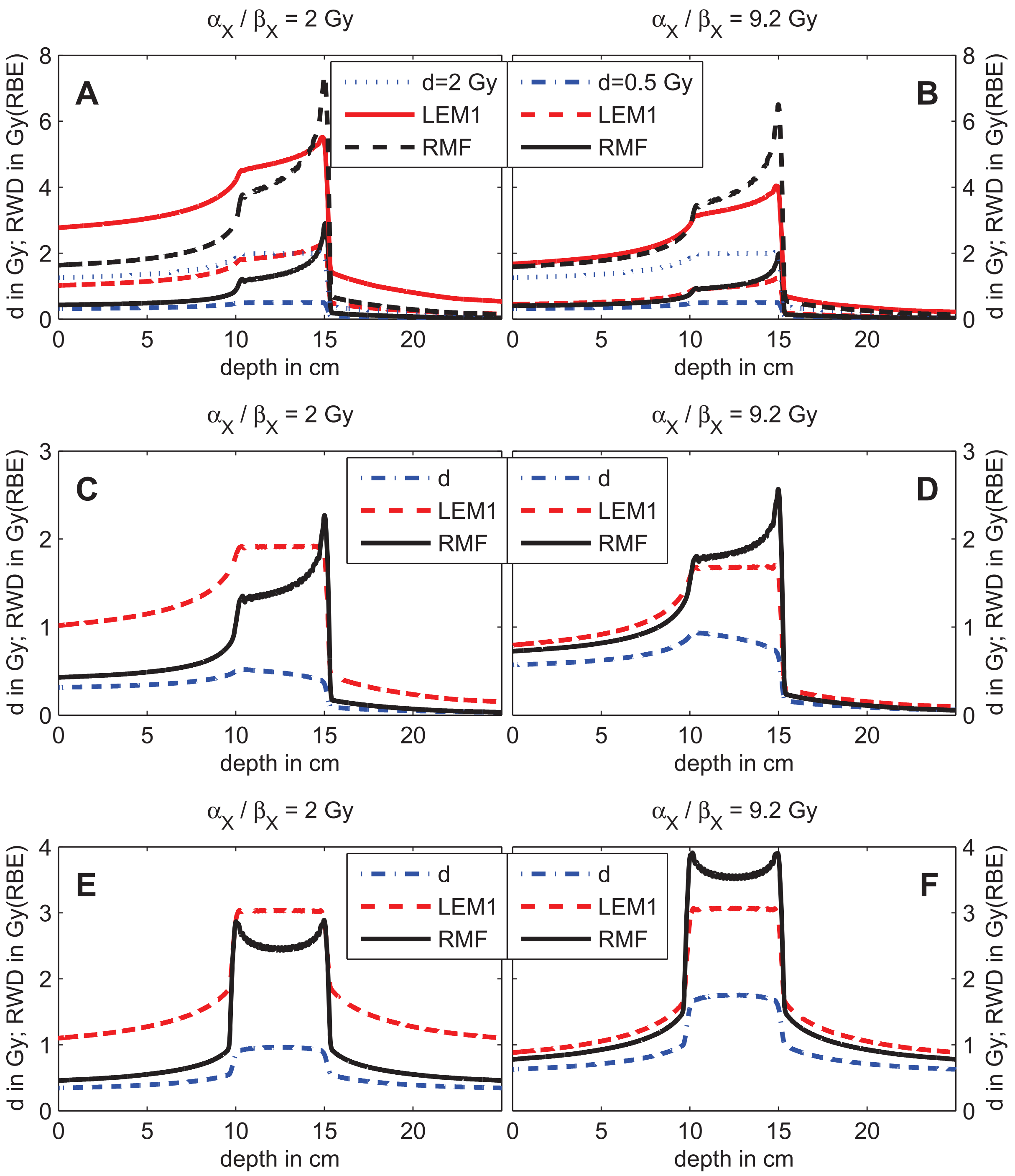

Figure 6.3.: Comparison of RMF model and LEM1 predictions for a 1-D treatment scenario. Plans were optimized on a constant physical dose of 0.5 and 2 Gy (panels A and B). Panels C and D (single field) and panels E and F (two fields) show scenarios based on the biological effect optimization for LEM1. RMF model predictions are recalculated with the same physical dose distribution resulting from LEM1. Panels C and D show the left fields of panels E and F.

	RBE (LEM1 / FLUKA)			RBE (LEM1 / Grün[29])		
Dose in Gy	Proximal	Distal	Average	Proximal	Distal	Average
0.5	3.52	4.77	3.94	3.69	4.99	4.19
1	2.83	3.74	3.12	2.96	3.86	3.30
2	2.24	2.87	2.43	2.33	2.93	2.56
5	1.65	1.99	1.74	1.70	2.01	1.82
10	1.34	1.52	1.39	1.38	1.52	1.43

	RBE (RMF / FLUKA)			RBE (LEM4 / Grün[29])		
Dose in Gy	Proximal	Distal	Average	Proximal	Distal	Average
0.5	1.89	5.28	2.88	2.09	8.61	4.19
1	1.77	4.31	2.52	1.80	6.45	3.30
2	1.65	3.55	2.22	1.53	4.75	2.56
5	1.55	2.87	1.95	1.26	3.13	1.83
10	1.51	2.57	1.84	1.13	2.28	1.45

Table 6.2.: Comparison of RBE model predictions calculated with the RMF model, LEM1-FLUKA combination as well as the LEM1 and LEM4 results reported by Grün *et al.* [29]. The values are taken from a spherical target optimization (diameter 6 cm) located in 10 cm depth in water at the depths 7 cm (proximal) and 13 cm (distal). The plans are optimized in 3-D to constant physical dose values ranging from 0.5 to 10 Gy.

We are able to reproduce the Grün-LEM1 values with our FLUKA-LEM1 combination. Deviations in RBE are less than 6%. This implementation allows the comparison of RMF model predictions to the latest version LEM4. In the proximal part of the planning target volume (PTV), RMF model and the LEM4 have lower RBE predictions than the LEM1. This effect is higher for the RMF model and small doses and smaller for higher doses. At the distal point of the PTV, both, RMF model and LEM4 increase the RBE values. Despite the high dose level of 10 Gy, RMF model prediction show a less steep increase of the RBE. The mean RBE values of the RMF model calculations are smaller than LEM1 and LEM4. This can be explained by a steeper increase at greater depth, towards the distal edge of the PTV of the RMF model predictions.

The RMF model predictions show similar behavior like the versions of the LEM. Deviations from the LEM1 have the same trend as the LEM4 (for $\alpha_x/\beta_x = 2$ Gy). Further LEM4 data, e.g. for different cell lines or treatment depths and geometries are not available in literature. For a comprehensive RMF model comparison to LEM4 further data are needed. Nevertheless, the performed validation of the RMF model justifies its use in the analysis of the uncertainties in the biological modeling of carbon ion treatment planning.

7. Treatment Optimization and Evaluation

The goal of radiotherapy is to kill cancer cells (treat the tumor) and at the same time spare normal tissue. This means to obtain the optimal treatment plan within physical and technological boundaries and respect to given clinical criteria. Those criteria and constraints are translated into numerical values which can be used as an input for optimization algorithms. An overview of different optimization approaches and algorithms can be found in literature (e.g. [28], chapter 17 and references therein).

In particle radiotherapy, several pristine Bragg peaks (spots) are placed in the target to cover the target homogeneously. An optimization is needed to find the necessary weights of the used spots. The aim of optimization in ion radiotherapy is to find an optimal set of weights for the beam spots to achieve the treatment goal, i.e. to deliver a prescribed dose to the target and preferably spare normal tissue. To translate this objective into a numerical function that can be handled by optimization algorithms, several steps have to be taken. In the next sections the needed physical and biological quantities and their calculation are presented. This is followed by the description of the used objective function and the implementation of additional constraints and objectives. Then the patient case used throughout this thesis is presented along with an exemplified optimization result. The chapter is completed by a short description of the tools implemented for treatment plan evaluation.

7.1. Voxel-wise Calculation of Relevant Physical and Biological Quantities

The concept of the ij-matrices was already introduced in section 5.1. The next equations give an overview of the implemented matrices as well as the physical and biological quantities that can be calculated in every voxel (i) for a given set of weights ω_j. The calculation of *LET* is described in [3], the calculation of $\alpha_{p,i}$ and $\beta_{p,i}$ in [42].

$$d_i = \sum_j d_{ij} \cdot \omega_j \tag{7.1}$$

$$\mathit{LET}_i = \frac{1}{d_i} \sum_j \mathit{LET}_{ij} \cdot d_{ij} \cdot \omega_j \tag{7.2}$$

$$\alpha_{p,i} = \frac{1}{d_i} \sum_j \alpha_{p,ij} \cdot d_{ij} \cdot \omega_j \tag{7.3}$$

$$\sqrt{\beta_{p,i}} = \frac{1}{d_i} \sum_j \sqrt{\beta_{p,ij}} \cdot d_{ij} \cdot \omega_j \tag{7.4}$$

The RMF model has the very convenient property that α_x and β_x can always be factored out and, hence, even be changed after an optimization without the need for much additional computation time. Using the RMF model, $\alpha_{p,i}$ and $\beta_{p,i}$ can be expressed similar to equations (6.7) and (6.8) on page 29.

$$\alpha_{p,i} = \alpha_{x,i} \cdot c_{1,i} + \beta_{x,i} \cdot c_{2,i} \tag{7.5}$$

$$\beta_{p,i} = \beta_{x,i} \cdot (c_{1,i})^2 \tag{7.6}$$

Solving equations (7.5) and (7.6) for $c_{1,i}$ and $c_{2,i}$ shows how to determine these values from known $\alpha_{p,i}$ and $\beta_{p,i}$ distributions. A change of α_x and β_x can be done very fast. It is based on $\alpha_{p,i}$ and $\beta_{p,i}$ only, without the need to store c_1 and c_2 values.

$$c_{1,i} = \sqrt{\frac{\beta_{p,i}}{\beta_{x,i}}} \tag{7.7}$$

$$c_{2,i} = \frac{\alpha_{p,i} - \alpha_{x,i}\sqrt{\frac{\beta_{p,i}}{\beta_{x,i}}}}{\beta_{x,i}} \tag{7.8}$$

Within the framework of the RMF model, also c_1 and c_2 can be implemented as ij-matrices. Combining equations (7.7) and (7.8) with equations (7.3) and (7.4) demonstrates this. Note, that $\alpha_{x,i}$ and $\beta_{x,i}$ can have a different value in every voxel i but do not depend on the spot j.

$$\begin{aligned} c_{1,i} &= \sqrt{\frac{\beta_{p,i}}{\beta_{x,i}}} \\ &= \sqrt{\frac{1}{\beta_{x,i} d_i^2}\left(\sum_j \sqrt{\beta_{p,ij}} \cdot d_{ij} \cdot \omega_j\right)^2} \\ &= \frac{1}{\sqrt{\beta_{x,i}} \cdot d_i} \sum_j \sqrt{\beta_{x,i}} \cdot c_{1,ij} \cdot d_{ij} \cdot \omega_j \\ &= \frac{1}{d_i} \sum_j c_{1,ij} \cdot d_{ij} \cdot \omega_j \end{aligned} \tag{7.9}$$

$$\begin{aligned} c_{2,i} &= \frac{\alpha_{p,i} - \alpha_{x,i}\sqrt{\frac{\beta_{p,i}}{\beta_{x,i}}}}{\beta_{x,i}} \\ &= \frac{-\alpha_{x,i}\sqrt{\frac{\beta_{p,i}}{\beta_{x,i}}} + \alpha_{p,i}}{\beta_{x,i}} \\ &= \frac{1}{\beta_{x,i}}\left(-\alpha_{x,i} \cdot c_{1,i} + \frac{1}{d_i}\sum_j \alpha_{p,ij} \cdot d_{ij} \cdot \omega_j\right) \\ &= \frac{1}{\beta_{x,i}}\left(-\alpha_{x,i} \cdot c_{1,i} + \frac{1}{d_i}\sum_j \alpha_{x,i} \cdot c_{1,ij} \cdot d_{ij} \cdot \omega_j + \frac{1}{d_i}\sum_j \beta_{x,i} \cdot c_{2,ij} \cdot d_{ij} \cdot \omega_j\right) \\ &= \frac{1}{d_i}\sum_j c_{2,ij} \cdot d_{ij} \cdot \omega_j \end{aligned} \tag{7.10}$$

The list of quantities that are needed in every voxel is completed by RBE, RWD and the equivalent dose in 2 Gy fractions (EQD2) [43] which are calculated for isoeffects in the LQ model framework. The dose d_i is a dose per fraction.

$$\begin{aligned} RBE_i &= \frac{-\alpha_{x,i} + \sqrt{\alpha_{x,i}^2 + 4\beta_{x,i}\left(\alpha_{p,i}d_i + \beta_{p,i}d_i^2\right)}}{2\beta_{x,i}d_i} && (7.11)\\ RWD_i &= RBE_i \cdot d_i && (7.12)\\ EQD2_i &= RBE_i \cdot N \cdot d_i \frac{RBE_i \cdot d_i + \alpha_{x,i}/\beta_{x,i}}{2\text{Gy} + \alpha_{x,i}/\beta_{x,i}} && (7.13) \end{aligned}$$

For the calculation of EQD2 the number of fractions N needs to be specified.

7.2. Cost-Function

Wilkens and Oelfke [42] proposed an optimization routine based on the biological effect.

$$\begin{aligned} F &= \sum_i p_i \left(\varepsilon_i(\omega) - \varepsilon_{i,pres}\right)^2 && (7.14)\\ &= \sum_i p_i \left[\left(\alpha_{p,i} \cdot d_i + \beta_{p,i} \cdot d_i^2\right) - \left(\alpha_{x,i} \cdot d_{x,i} + \beta_{x,i} \cdot d_{x,i}^2\right)\right]^2 && (7.15) \end{aligned}$$

where F is the objective function and p_i the penalty term. This term is the relative importance of the deviation from the prescribed biological effect. The higher p_i, the more important it is to achieve the prescribed biological effect in this voxel. As the biological effect is a less intuitive quantity, RWD values are prescribed for this carbon ion optimization. The RWD can be converted to a biological effect by equation (2.3). The objective function is minimized using the fmincon functionality contained in the Matlab (versions 2012-2014a) optimization toolbox with the constraint that $\omega_j \geq 0 \; \forall j$. For an optimization step, the gradient is needed for all beam spots.

$$\frac{\partial F}{\partial \omega_k} = 2\sum_i p_i \left(\varepsilon_i(\omega) - \varepsilon_{i,pres}\right) \cdot \left[\alpha_{p,ik}d_{p,ik} + 2\left(\sum_j \sqrt{\beta_{p,ij}}d_{p,ij} \cdot \omega_j\right) \cdot \sqrt{\beta_{p,ik}}d_{p,ik}\right] \quad (7.16)$$

The sums in the description of the objective functions include all voxel. This is done for an easier notation. If one voxel should not appear in the objective function, the corresponding penalty term is set as $p_i = 0$. To save computation time and RAM (Random-Access Memory), voxel with $p_i = 0$ are removed before the optimization. The L-BFGS (limited memory-Broyden-Fletcher-Goldfarb-Shanno [44, 42] algorithm is used for the determination of the Hessian matrix. For the sake of completeness, the formulas for the analytical calculation of the Hessians are given in Appendix A.

7.3. Objectives and Constraints

To steer the optimization towards the result desired, additional objectives and constraints can be added to the objective function.

7.3.1. Implemented Objectives

Additional terms for maximum and minimum RWD can be assigned for every voxel and converted to biological effects. Objectives for the maximum RWD are used to spare normal tissue or avoid hot spots in the target, whereas minimum RWD objectives are reasonable only for target structures.

$$F_{objMax} = \sum_i p_{i,objMax} \left[\varepsilon_i(\omega) - \varepsilon_{i,objMax}\right]_+^2 \tag{7.17}$$

$$F_{objMin} = \sum_i p_{i,objMin} \left[\varepsilon_{i,objMin} - \varepsilon_i(\omega)\right]_+^2 \tag{7.18}$$

The $[\,]_+$ operator is short notation for a multiplication by the Heaviside step function $H(x)$, which is 0 for $x < 0$ and 1 for $x \geq 0$. The gradients for the objectives can be calculated similarly to equation (7.16) because the terms with the first derivation of $H(x)$ are 0.

$$\frac{\partial F_{objMax}}{\partial \omega_k} = 2\sum_i p_{i,objMax} \left[\varepsilon_i(\omega) - \varepsilon_{i,objMax}\right]_+ \cdot g(\alpha_p, \beta_p, d, \omega) \tag{7.19}$$

$$\frac{\partial F_{objMin}}{\partial \omega_k} = 2\sum_i p_{i,objMin} \left[\varepsilon_{i,objMin} - \varepsilon_i(\omega)\right]_+ \cdot g(\alpha_p, \beta_p, d, \omega) \tag{7.20}$$

with

$$g(\alpha_p, \beta_p, d, \omega) = \left[\alpha_{p,ik} d_{p,ik} + 2\left(\sum_j \sqrt{\beta_{p,ij}} d_{p,ij} \cdot \omega_j\right) \cdot \sqrt{\beta_{p,ik}} d_{p,ik}\right]$$

Note, that these objectives are minimized too, hence the total cost function for an optimization including objectives is calculated as a sum. Consequently also the gradients are summed up.

$$F_{tot} = F + F_{objMax} + F_{objMin} \tag{7.21}$$

$$\frac{\partial F_{tot}}{\partial \omega_k} = \frac{\partial F}{\partial \omega_k} + \frac{\partial F_{objMax}}{\partial \omega_k} + \frac{\partial F_{objMin}}{\partial \omega_k} \tag{7.22}$$

The calculation of the corresponding Hessian matrices is summarized in Appendix A.2.

7.3.2. Implemented Constraints

Besides the constraint for ω_j ($\omega_j \geq 0$), hard minimum and maximum RWD constraints can be set. Again, using equation (2.3), RWD can be converted into biological effects. Using the feature of the Matlab fmincon function which allows nonlinear constraints in form of $c(\omega) \leq 0$, a hard maximum and minimum biological effect constraint can be added to the optimization for all voxel where desired.

$$c_{i,conMax} = \alpha_{p,i} d_{p,i} + \beta_{p,i} d_{p,i}^2 - \varepsilon_{i,conMax} \leq 0 \tag{7.23}$$

$$c_{i,conMin} = -\alpha_{p,i} d_{p,i} - \beta_{p,i} d_{p,i}^2 + \varepsilon_{i,conMin} \leq 0 \tag{7.24}$$

	p	$\mathrm{RWD_{pres}}$	$\mathrm{p_{objMax}}$	$\mathrm{RWD_{objMax}}$	$\mathrm{p_{objMin}}$	$\mathrm{RWD_{objMin}}$
Target	150	3 Gy(RBE)	150	3.4 Gy(RBE)	300	2.95 Gy(RBE)
non Target	0	—	10	2.5 Gy(RBE)	0	—

Table 7.1.: Default prescribed RWD, penalties and objectives for the optimizations performed for this work. Constraints were not applied.

The corresponding gradients are

$$\frac{\partial c_{i,conMax}}{\partial \omega_k} = \alpha_{p,ik} d_{p,ik} + 2\left(\sum_j \sqrt{\beta_{p,ij}} d_{p,ij} \cdot \omega_j\right) \cdot \sqrt{\beta_{p,ik}} d_{p,ik} \tag{7.25}$$

$$\frac{\partial c_{i,conMin}}{\partial \omega_k} = -\alpha_{p,ik} d_{p,ik} - 2\left(\sum_j \sqrt{\beta_{p,ij}} d_{p,ij} \cdot \omega_j\right) \cdot \sqrt{\beta_{p,ik}} d_{p,ik} \tag{7.26}$$

A further constraint forces the mean RWD inside the target to be the prescribed RWD. It was implemented using the equal constraint of the Matlab fmincon function, which has the general form $ceq(\omega) = 0$. Applying this for the mean prescribed dose in the target we get:

$$ceq_{meanTar} = \frac{1}{N_{tar}} \sum_{i \in tar} \left(\alpha_{p,i} d_{p,i} + \beta_{p,i} d_{p,i}^2 - \varepsilon_{presTar}\right) = 0 \tag{7.27}$$

with N_{tar} being the number of voxel in the target. It is assumed that $\varepsilon_{presTar}$ is constant throughout the target. The gradient can be calculated as follows.

$$\frac{\partial ceq_{meanTar}}{\partial \omega_k} = \frac{1}{N_{tar}} \sum_{i \in tar} \left[\alpha_{p,ik} d_{p,ik} + 2\left(\sum_j \sqrt{\beta_{p,ij}} d_{p,ij} \cdot \omega_j\right) \cdot \sqrt{\beta_{p,ik}} d_{p,ik}\right] \tag{7.28}$$

The calculation of the Hessian of the implemented constraints is presented in Appendix A.3.

7.4. Example of a Treatment Plan Optimization Result

Figure 7.1 shows a result of a treatment plan optimization. This astrocytoma patient was initially treated with photon radiotherapy at the Klinikum rechts der Isar in Munich and is used as the planning and evaluation example throughout this work. For figure 7.1 constant values $\alpha_x = 0.1\,\mathrm{Gy}^{-1}$ and $\beta_x = 0.05\,\mathrm{Gy}^{-2}$ are set throughout the patient. The RMF model is used here. (A similar example using the LEM1 is shown in figure B.1 in Appendix B.) The plan was optimized on RWD = 3 Gy(RBE) in the target region with two carbon beams. These eight panels show the used beam geometry and the calculated biological and physical quantities in color on top of the patient CT. The optimization settings in terms of prescribed RWD, penalties and objectives are summarized in table 7.1. These are the default values, used if not specified otherwise. Constraints were not applied for the optimizations executed for this work.

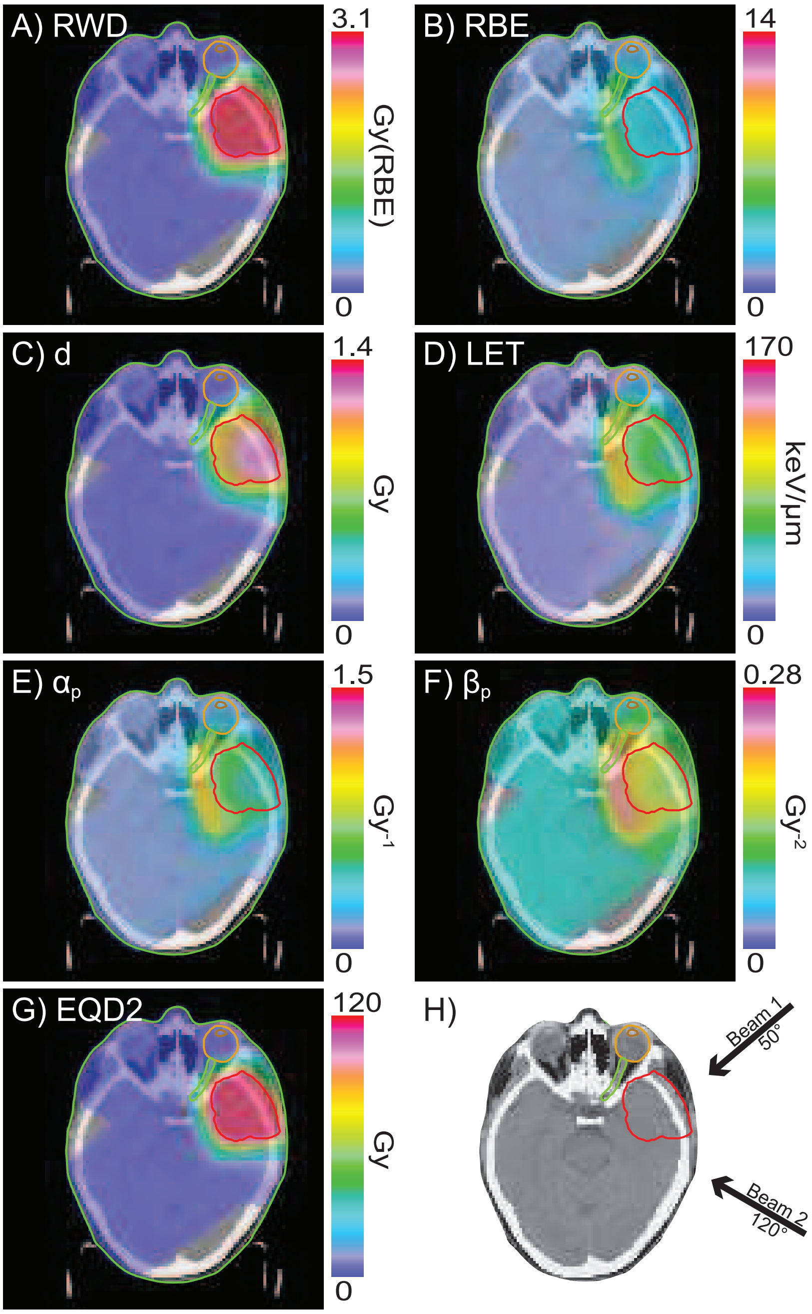

Figure 7.1.: Example of an optimization result with the RMF model showing the optimized RWD (panel A) and the calculated RBE (panel B). Physical dose and dose-weighted LET are plotted in panels C and D. The radiosensitivity parameters α_p and β_p (panels E and F respectively) were obtained with the RMF model and constant values $\alpha_x = 0.1$ Gy^{-1} and $\beta_x = 0.05$ Gy^{-2}. Panel G shows the EQD2 calculated voxel by voxel. The used beam geometry for the astrocytoma patient can be found in panel H. The planning target volume (PTV) is marked in red, the left optical nerve in green together with the left eyeball (orange) and the left lens (brown).

7.5. Treatment Evaluation

In the following sections, treatment plan evaluations are introduced. For evaluation and comparison the information in the three-dimensional maps (cf. figure 7.1) needs to be compressed and visualized. The approaches presented here do not comprise the entire list of tools and values available in radiotherapy. The selection is limited to the approaches implemented in the sensitivity analysis performed in this work.

Referring to the uncertainties in biological dose response models, a further differentiation can be done. Here I want to draw attention to the dimension of the examined treatment evaluation. The three-dimensional maps in the previous chapter are of the highest dimension. This information is reduced to one dimension for dose-volume histograms presented in section 7.5.1. Tumor control probability (TCP, section 7.5.2) and $\mathrm{d}_{\mathrm{Vol}}$ (section 7.5.1) are scalars. The reduction of dimensions results, inevitable, in a loss of information.

7.5.1. Dose-Volume Histogram (DVH) and $\mathrm{d}_{\mathrm{Vol}}$

Dose-volume histograms (DVHs) are commonly used tools for three-dimensional treatment plan evaluation. They convert 3-D dose distributions into histograms, displaying the main features of a treatment plan: maximum, minimum, mean and median dose. Another measure, strongly related to the DVH, is $\mathrm{d}_{\mathrm{Vol}}$. It describes the dose that a part of the volume reaches or exceeds. For example, $\mathrm{d}_{98\%} = 2$ Gy means that at least 2 Gy are delivered to 98% of the volume (cf. reference [45], page 127). Note, that the dose per fraction is used here to be consistent with the calculations in the previous chapters.

DVHs can be presented in both differential and cumulative form. As cumulative DVHs are usually used in clinical routine, this type of histogram is considered in this thesis. A cumulative DVH shows the fraction of the volume of a structure receiving doses of at least a given value [46, 47].

The concept of DVHs and $\mathrm{d}_{\mathrm{Vol}}$ were introduced for photon irradiation, but can applied for ion therapy as well. This leads to the RWDVH (RBE-weighted dose-volume histogram) and $\mathrm{RWD}_{\mathrm{Vol}}$. Figure 7.2 shows the RWDVH of the optimization result in figure 7.1 for two different structures.

7.5.2. Tumor Control Probability (TCP)

The tumor control probability (TCP) was introduced to describe the outcome of a radiotherapy treatment. Several TCP models were developed ([28], page 228 and references therein). TCP modeling is complex, as tumor response is influenced by several factors, which may change dynamically. The response of tumor cells depend for example on oxygenation, angiogenesis and the state of the cell cycle.

Here a simple Poisson statistics based model is used, which is derived from the LQ cell survival description and does not include repopulation, (changing) oxygenation et cetera. Several additional assumptions are made. The main assumption is that a tumor consists of a number of non-interacting, individually responding clonogenic cells. The tumor is locally controlled in case zero clonogenic cells survive [48]. TCP can then be calculated as the probability that all clonogenic cells are killed.

$$TCP = exp\left[-\sum_{i\in PTV}\rho_c\nu_i\cdot exp\left(-\alpha_{p,i}d_iN-\beta_{p,i}d_i^2N\right)\right]. \tag{7.29}$$

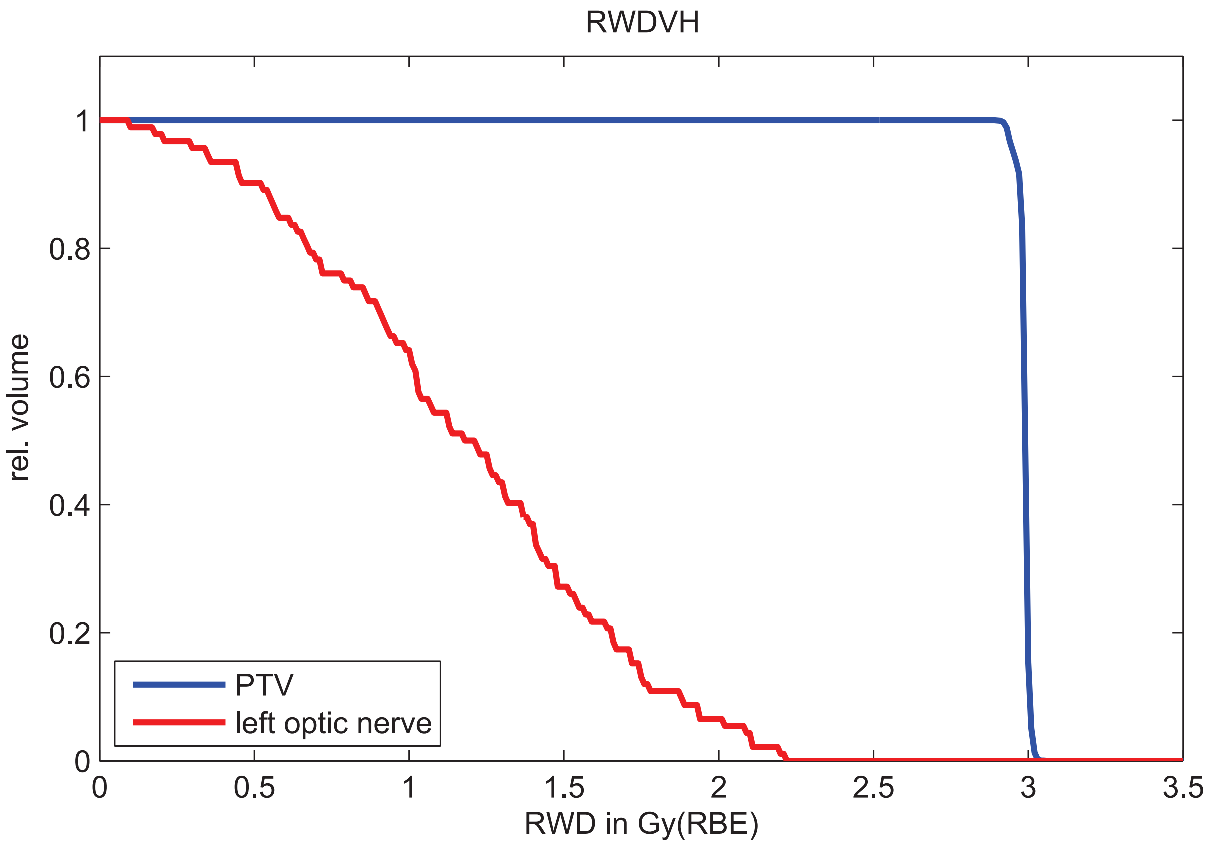

Figure 7.2.: Example of a RWDVH for the RWD distribution shown in figure 7.1 panel A for two structures. Example $\mathrm{RWD}_{\mathrm{Vol}}$ values for the planning target volume (PTV) are: $\mathrm{RWD}_{98\%} = 2.93$ Gy(RBE) and $\mathrm{RWD}_{2\%} = 3.16$ Gy(RBE).

The density of the clonogenic cells ρ_c is set, spatially constant, to 10^7 cm^{-3} cells. In this thesis the volume of a voxel is used for ν_i. In the used patient case this means $\nu_i = (0.2\ \mathrm{cm})^3$.

This is a brief introduction to TCP calculations. This thesis neither aims to predict absolute TCP values, nor does it compare different (competing) treatment plans. TCP is introduced to examine how the calculation itself is subject to changes due to uncertainties in biological parameters. For this, equation (7.29) is adequate. Normal tissue complication probabilities, which limit the maximum achievable dose in the tumor and hence TCP are not evaluated within the scope of this thesis.

Part III.

Sensitivity Analysis

The uncertainties in biological dose response models are investigated with a sensitivity analysis (SA). A sensitivity analysis can be defined as: *The study of how uncertainty in the output of a model (numerical or otherwise) can be apportioned to different sources of uncertainty in the model input.* (Saltelli *et al.* [49]). Two features are important throughout this thesis. First, it is important to calculate and quantify uncertainties in the model output. Second, the composition of this uncertainty in the output is broken down to the different input uncertainties. Without the second feature, the analysis would be better characterized as an uncertainty analysis and not a sensitivity analysis.

The SA applied here demonstrates the impact of uncertainties in the model input, resulting in an uncertainty of the output. In addition, SA aims to tell the relative importance of different model input uncertainties on the output uncertainty. In other words, the uncertainties of the biological dose response models (error bars) are determined, accompanied by the information about its composition. With this, a weighting of the impact of different uncertainties in the model input is achieved.

8. Sensitivity Analysis Methods

In this chapter several well known, basic SA methods are recapitulated followed by a set of more advanced variance (or Monte Carlo)-based approaches. After a short introduction to the method, I will point out the limitations of the basic SA methods and why more advanced methods are needed here. Additionally the drawbacks of the new approaches are discussed together with their implementation into treatment plan evaluation. The end of this chapter links the SA to treatment plan evaluation by showing newly developed visualization methods. These visualizations are essential for analyzing the SA results.

First the SA methods are presented in a general (more mathematical) way. Then they are adapted to the biological methods in carbon ion therapy. As an example function $Y(X_1, ..., X_j, ..., X_m)$ of m input variables can be considered. For a better notation it is assumed that all X_j affect Y (meaning $\partial Y/\partial X_j \neq 0$). For the sake of convenience, the input variables are independent $\partial X_j/\partial X_k = 0$ for $k \neq j$ if not indicated otherwise (the case of dependent variables is discussed briefly for SA approaches where it might be important). The basic motivation of any SA is to evaluate the impact of a change or uncertainty ΔX_j in the inputs X_j on the result Y. This can be done using the following methods.

8.1. Simple Sensitivity Analysis

8.1.1. Method

The simplest and hence extensively used method to access the sensitivity of Y on a change in X_j is to add this change $X_j + \Delta X_j$ and reevaluate the function.

$$\Delta_j Y = Y(X_1, ..., X_j + \Delta X_j, ..., X_m) - Y(X_1, ..., X_j, ..., X_m) \tag{8.1}$$

This way is often used to show a general behavior of a function with changing input. A further step, defining a simple sensitivity value S, is to divide equation (8.1) by the change in one parameter.

$$S_j^{simple} = \frac{Y(X_1, ..., X_j + \Delta X_j, ..., X_m) - Y(X_1, ..., X_j, ..., X_m)}{\Delta X_j} \tag{8.2}$$

Equations (8.1) and (8.2) are strongly related to each other. Most often equation (8.1) is used in literature related to ion therapy. An example is shown in [8] where inputs are changed by ±25%. The definition of S_j^{simple} is added here because it shows the first step towards a mathematical treatment of changes. The difference caused by a changing X_j is normalized by the size of the change and hence better comparable in the mathematical sense. This is not necessarily true for actually applied physical functions and input uncertainties. To demonstrate this, the very simple function $Y = X_1 + X_2$ can be used as an example. In case that the uncertainty in X_1 is small (e.g. $\Delta X_1 = 0.1$) compared to the uncertainty in X_2 (e.g. $\Delta X_2 = 1$), both sensitivities are $S_1^{simple} = S_2^{simple} = 1$, indicating the same impact, whereas Y is changed by $\Delta_1 Y = 0.1$ compared to $\Delta_2 Y = 1$. The normalization to the size of the change is not always useful.

Evaluating either of these two equations systematically for all m input parameters, gives a first impression of the different impacts of changes in different X_j. This method was already applied for SAs of RBE predictions with the LEM (cf. section 6.1) and the dependencies on different model parameters [8, 9]. Note, that in references [8, 9] $Y(X_1, ..., X_j + \Delta X_j, ..., X_m)$ is compared to $Y(X_1, ..., X_k + \Delta X_k, ..., X_m)$ with $k \neq j$. This simple SA method can on the one hand be used for arbitrary numerical and analytical functions and is fast from the computational side. On the other hand it has several drawbacks and limitations to be discuss in the next section.

8.1.2. Limitations

The implementation and execution of this approach appears to be straight forward and fast. Having a closer look, several drawbacks come to mind. First, Y is only evaluated around one point $(X_1, ..., X_m)$. In addition, if the function Y is not linear in X_j, the measure S_j^{simple} is dependent on ΔX_j. $\Delta_j Y$ is always dependent on ΔX_j. This means, for this type of sensitivity approach you need to know (or guess) how much a parameter has to be changed. This is inevitable. However other SA approaches are able to handle an assumed distribution for all ΔX_j automatically. A third main drawback is the difficulty to obtain interplay effects (cross terms) of two input parameters. It is possible to change several parameters and calculate e.g. $Y(X_1 + \Delta X_1, ..., X_j + \Delta X_j, ..., X_m + \Delta X_m) - Y(X_1, ..., X_m)$. For biological dose response modeling, this is done with two input parameters by Böhlen *et al.* [8].

Interplay in terms of $\Delta_{jk} Y$ indicate the deviation caused by the combination of two changes.

$$\Delta_{jk} Y = Y(X_1, ..., X_j + \Delta X_j, X_k + \Delta X_k, ..., X_m) - Y(X_1, ..., X_m) - \Delta_j Y - \Delta_k Y \quad (8.3)$$

Consequently the calculation effort grows very fast in this approach, if more than two input parameters are considered. An example demonstrating this interplay effect is presented in Appendix C.

Even if this SA approach was executed systematically, it becomes very difficult to evaluate the SA result. Already at one point in the $(X_1, ..., X_m)$ space, it gets very complex (or impossible) to visualize changes in several input parameters, including cross terms.

8.2. Gaussian Error Propagation

The Gaussian error propagation is the best known error propagation in physics. It is called Gaussian, because the uncertainties in the input parameters are assumed to be normally (Gaussian) distributed. These distributions are described by a mean value $\bar{X}_j$ and the standard deviation σ_j. The general $X_j + \Delta X_j$ can hence be described as $\bar{X}_j + \sigma_j$. The evaluated function Y must be analytical.

8.2.1. Method

The Gaussian error propagation evaluates a numerical function around the mean values $\bar{X}_j$ of the input. A Taylor series is expanded around the result of these mean values (cf. e.g. reference [50]).

$$Y_{Tay} \approx Y(\bar{X}_1, ..., \bar{X}_m) + \sum_{j=1}^{m} \Delta X_j \left[\frac{\partial Y}{\partial X_j}\right]_{\bar{X}_1,...,\bar{X}_m} \tag{8.4}$$

By setting $\Delta X_j = \sigma_j$ the assumed normal distributions for the uncertainty in the input parameters can be propagated to the result of the function. Their combination allows to determine the standard deviation of the result.

$$\sigma_Y = \sqrt{\sum_{j=1}^{m} \sigma_j^2 \left[\frac{\partial Y}{\partial X_j}\right]^2_{\bar{X}_1,...,\bar{X}_m}} \tag{8.5}$$

A sensitivity value can be defined as

$$S_j^{gauss} = \sigma_j^2 \left[\frac{\partial Y}{\partial X_j}\right]^2_{\bar{X}_1,...,\bar{X}_m} \tag{8.6}$$

indicating the composition of σ_Y and hence the sensitivity of the result on an uncertainty in X_j. For equations (8.4)-(8.6) it is necessary that $\partial X_j/\partial X_k = 0$, meaning independent inputs. There are ways to include dependencies within input parameters into this approach. In the next section, it is explained why the Gaussian error propagation is not suitable for the biology of carbon ion therapy. That is why dependent input parameters are not further introduced here. Note the link in-between equation (8.2) and (8.4). The limit $\Delta X_j \rightarrow 0$ transfers equation (8.2) to $\partial Y/\partial X_j$. For analytical functions, the Gaussian error propagation overcomes some of the limitations discussed for the simple SA (cf. section 8.1.2). In the Gaussian error propagation the partial derivation is multiplied by the standard deviation. Thus uncertainty distributions in the inputs can be combined in a consistent way, resulting in a standard deviation and hence, a distribution in the result.

8.2.2. Limitations

Only analytical functions can be evaluated with a Gaussian error propagation. Most of the methods of treatment plan evaluation cannot be described reasonably by analytical functions, as they are based on the distribution throughout the patient geometry (cf. chapter 7.5). The Gaussian error propagation is consequently not suitable for the SA of biological model processes in carbon ion therapy. Further general limitations of this approach are the goodness of the approximation with a Taylor series expansion. The linear terms considered here, describe the function well only in the region around the expansion (here $\bar{X}_1, ..., \bar{X}_m$). The linearity should be a good approximation at least $\pm\sigma_j$ from the mean values [50]. Additionally the uncertainty distribution of the input parameters needs to be Gaussian, or at least of a very similar shape.

8.3. Factor Prioritization

Factor Prioritization (FP) is a SA approach that is able to rank (prioritize) the impact of uncertainties on a result of a function. It overcomes most of the drawbacks mentioned for the simple SA (cf. section 8.1.2) and the Gaussian error propagation (cf. section 8.2.2).

FP is a variance-based Monte Carlo approach. It is described by A. Saltelli *et al.* [51] in the book *"Global Sensitivity Analysis, The Primer"*. The method can be explicitly used for any numerical or analytical function. It is possible to assign uncertainties of different shape (not only Gaussian) and evaluate the function over a range in the whole $(X_1, ..., X_m)$ space. In this section I describe the method itself and its implementation for biological modeling of carbon ion therapy (compare to Kamp *et al.* [21]), followed by the discussion of its limitations and challenges.

8.3.1. Method

In this Monte Carlo approach a function is evaluated $n = 10^3$ to 10^6 times, depending on the number of input parameters. For each run all parameters are changed simultaneously, using random numbers according to their associated uncertainties. To describe the uncertainty in an input variable any random number distribution can be assigned. This includes the common normal, uniform, asymmetrical (e.g. Beta distribution) or discontinuous (e.g. Poisson) distributions. The distribution should be chosen to best describe the uncertainty.

Consequently the result of the function Y needs to be written as a vector $\boldsymbol{Y}$ of length n, where each entry is calculated with the corresponding entries of the randomly changed input parameters $(\boldsymbol{X_1}, ..., \boldsymbol{X_m})$ of the same length n. Variance-based statistic formalisms rank the input parameter-uncertainty pairs according to their impact on the result of the function. This sensitivity S_j (first order sensitivity index) on the j-th input parameter X_j is defined as:

$$S_j = \frac{var\left(mean\left(\boldsymbol{Y}|X_j \approx const\right)\right)}{var\left(\boldsymbol{Y}\right)} \tag{8.7}$$

The numerator is calculated following reference [51] by first sorting the n $(X_j; Y)$ pairs by increasing X_j. The sorted pairs are divided into n_{par} equally sized partitions containing n/n_{par} entries with increasing X_j. The mean value is taken from these partitions, the variance from the n_{par} mean values. Within the scope of this work, n_{par} was set to 256. Calculated this way, the sensitivity ranges from $S = 0$ (no influence) to $S = 1$ (only influential part).

8.3.2. Implementation

Computation time and memory are the most crucial factors for the implementation of a FP into carbon ion treatment planning. For instance, in case of the astrocytoma patient discussed earlier (cf. figure 7.1, page 42) the dose was calculated in almost $3 \cdot 10^5$ voxel. Combining this calculation with $n = 10^6$ runs in every voxel it becomes obvious why it is necessary to consider computation time and memory.

The implementation strongly depends on the nature of the measure. On the one hand there are voxel based quantities like RBE_i, RWD_i, $EQD2_i$, $\alpha_{p,i}$ and $\beta_{p,i}$ which are calculated in every voxel i (cf. section 7.1). On the other hand there are structure-based quantities like (RW-)DVH, $\mathrm{d_{Vol}}$ or TCP (cf. section 7.5) calculated based on all voxel in a certain structure.

Figure 8.1 illustrates the two different approaches. For a voxel-wise SA, the voxel are grouped into subgroups of e.g. 1000 voxel (panel A) and the S values are calculated in parallel at the same time for one subgroup. The number of voxel in one subgroup is selected to use the available memory most efficiently. Computation time can be decreased

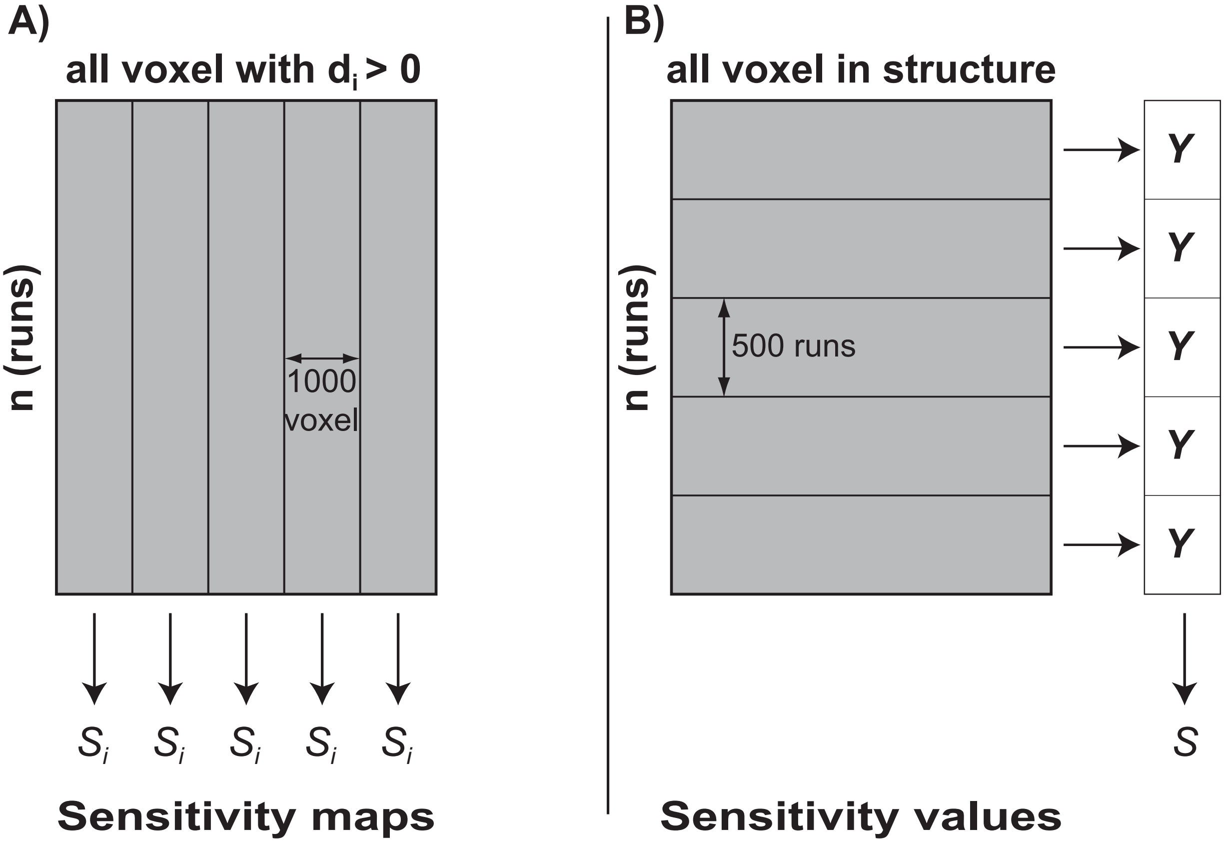

Figure 8.1.: Schematic representation of the memory saving SA implementation. Panel A depicts the approach for a voxel-wise SA, as it is done for RBE, RWD or EQD2 resulting in sensitivity maps. A subgroup of e.g. 1000 voxel can be calculated at once (parallelization). In contrast to this, panel B shows the structure-based implementation. Measures like (RW-)DVH, d_{Vol} or TCP combine all RWD information of a structure to one value. First this result vector $\boldsymbol{Y}$ is calculated, then the sensitivity. The calculation is grouped in the direction of the number of runs, e.g. 500 runs can be executed simultaneously (parallelization). Typical values for the number of runs, number of voxel (panel A) and number of voxel in a target (panel B) are $n = 10^5$, $3 \cdot 10^5$ and $3.5 \cdot 10^4$ respectively.

by calculating e.g. $S(RBE)$, $S(RWD)$ and $S(EQD2)$ one after each other for one subgroup, because in this case indexing and parameter changing have to be done only once. Resulting S_i maps for all X_j can be displayed similarly to the color wash of the dose maps on patient geometries.

Panel B shows the second approach, needed to efficiently calculate sensitivities of structure based values. For the assessment of measures like (RW-)DVHs, d_{Vol} and TCP the complete information of all voxel in the structure have to be available. These measures are parallelized in the direction n, e.g. 500 runs at once. This number of runs is selected to use the available memory most efficiently. The sensitivity is calculated once all n runs are completed. Several of the structure-based measures can again be executed successively for the same subset of runs.

In general, the same set of random numbers is used for every voxel. This can be done if relative uncertainties are assigned for every input parameter. Unnecessary sorting of the same random numbers repeatedly is prevented by storing and reusing the indexing after sorting it the first time in one X_j.

An extensive testing was done for the necessary size of n and n_{par}. They were set to $n = 131072 = 2^{17}$ and $n_{par} = 256 = 2^8$. It resulted in 5-9 h computational time for a comprehensive FP for all mentioned voxel and structure-based measures and five changed input parameters. The exact time depends on the used beam geometry. The calculations were done on a 8 core 2.66 GHz workstation with 32 GB RAM (Random-Access Memory). The calculation of a subset has the potential to be faster. For example a FP of five $\mathrm{RWD}_{\mathrm{Vol}}$ values and the (RW-)DVHs of the PTV and some structures is done in few minutes.

8.3.3. Limitations

The FP approach has its main limitation in computational time and the required memory capacity. When applying it to the biology of carbon ions, those limitations have to be considered simultaneously. Due to the high grade of parallelization, computation time is accelerated best by a higher number of cores. The memory available must be above a certain threshold to allow the allocation of every necessary array once. Then, the more memory is available, the larger are possible subgroups (cf. figure 8.1). For instance, this saves up to e.g. 15 % computational time for a step from 500 to 10^4 voxel per subgroup. A further limitation of the FP approach is the requirement for independent input parameters ($\partial X_j/\partial X_k = 0$ for $k \neq j$). The consequences of this requirement are discussed later on in chapter 11.

8.4. Cross Terms and Factor Fixation

The approach of the FP is extended by adding interplay effects in terms of higher-order sensitivity values (also called cross terms). The resulting methods of total sensitivity (TS) and the factor fixation (FF) approach are adapted from the book *"Global Sensitivity Analysis, The Primer"* by Andrea Saltelli *et al.* [51]. The assessment of cross terms is necessary in case $(X_1, ...X_m)$ are not combined linearly, meaning for functions that $\partial^2 Y/\partial X_j \partial X_k \neq 0$ for any $j \neq k$. The FF method offers a criterion to remove an input parameter from the SA. If a change in an input has no impact on the result, it can be set constant.

8.4.1. Method

Higher-order sensitivity parameters can be calculated similarly to S_j in equation (8.7) combined with equation (8.3). For the second-order this means:

$$S_{jk} = \frac{var\left(mean\left(\boldsymbol{Y}|X_j \approx const, X_k \approx const\right)\right)}{var\left(\boldsymbol{Y}\right)} - S_j - S_k \tag{8.8}$$

The numerator is calculated by first sorting the n $(X_j; Y)$ pairs with increasing X_j. The sorted pairs are divided into $n_{par,j}$ equally sized partitions containing $n/n_{par,j}$ entries with increasing X_j. Within these $n_{par,j}$ partitions, the $(X_k; Y)$ pairs are sorted with increasing X_k and divided in $n_{par,k}$ parts. The mean value is then taken over each of the $n_{par,j} \cdot n_{par,k}$ parts. Higher-order terms, e.g. S_{jkl}, can be calculated accordingly. It is obvious that with increasing number of evaluated inputs m this method becomes more and more computationally intensive. First of all the number of runs n must be large enough to have a reasonable mean value in case the highest-order is calculated ($n/(n_{par,1} \cdot ... \cdot n_{par,m}) \geq 64$). In addition, the possible combinations grow with the m^2.

Combining all possible cross terms which include a sensitivity on X_j, leads to the total sensitivity value TS_j.

$$TS_j = S_j + \sum_{k \neq j} S_{jk} + \sum_{k \neq j, l \neq j, l \neq k} S_{jkl} + ... + S_{1...m} \tag{8.9}$$

With equation (8.9) the factor fixation method can be defined. If $TS_j \approx 0$ then the parameter X_j has no influence on the change in Y. The parameter can be fixed to an arbitrary value within the simulated random number distribution. The number of input parameters can be reduced by one. Note, that the mathematical condition $TS_j = 0$ was adapted to $TS_j \approx 0$ as it is numerically not possible to achieve $TS_j = 0$.

There are several properties associated with the cross terms and the TS. They are derived and motivated in reference [51]. They become true for a large n.

$$S_{ij} = S_{ji} \tag{8.10}$$

$$S_j \leq TS_j \tag{8.11}$$

$$\sum_j S_j + \sum_j \sum_{k>j} S_{jk} + \sum_j \sum_{k>j} \sum_{l>k} S_{jkl} + ... + S_{1...m} = 1 \tag{8.12}$$

A set of useful consequences can be obtained from these relations. In case $\sum_j S_j = 1$, none of the higher-order sensitivity values is nonzero. Hence, $TS_j = S_j$ for all j. Consequently, in case $TS_j = S_j$ for X_j, all cross terms containing it are zero. This can be reverted as well. In case $TS_j > S_j$ there are nonzero cross terms for the input X_j.

The full potential of these relations is explained in the next section. It is possible to determine S_j and TS_j directly, without calculating all higher-order S values explicitly.

8.4.2. Implementation

Computation time for all cross terms in equation (8.9) and all voxel is not feasible in biological modeling in carbon ion treatment planning (even for $m = 3$). For structure-based measures it is possible but still very computationally intense. This is further discussed in the next section considering the limitations of this SA approach. Saltelli *et al.* [51] described a faster method to calculate S_j and TS_j. Here, the initial set of $(\boldsymbol{X_1}, ..., \boldsymbol{X_m})$ of size n is extended as shown in figure 8.2. This leads to $\boldsymbol{Y}$ being of length $n(m+2)$. Combined with the description of the variance as scalar products, S_j and TS_j can be determined (cf. [51], page 165).

$$S_j = \frac{\boldsymbol{Y_A} \circ \boldsymbol{Y_{C_j}} - mean\,(\boldsymbol{Y_A})}{\boldsymbol{Y_A} \circ \boldsymbol{Y_A} - mean\,(\boldsymbol{Y_A})} \tag{8.13}$$

$$TS_j = 1 - \frac{\boldsymbol{Y_B} \circ \boldsymbol{Y_{C_j}} - mean\,(\boldsymbol{Y_A})}{\boldsymbol{Y_A} \circ \boldsymbol{Y_A} - mean\,(\boldsymbol{Y_A})} \tag{8.14}$$

The scalar product is indicated by "$\circ$", the derivation of the random number sets $\boldsymbol{A}, \boldsymbol{B}$ and $\boldsymbol{C_j}$, based on which $\boldsymbol{Y_A}, \boldsymbol{Y_B}$ and $\boldsymbol{Y_{C_j}}$ are calculated, is shown in figure 8.2. The implementation, especially the differentiation between voxel-wise and structure-based SA, is done in the same way as for the FP in section 8.3. Note, that in figure 8.1 on page 53 the number of runs n needs to be substituted by $n(m+2)$. As the number of runs is increased here, the size of the subgroups that can be executed simultaneously for an optimal use of memory, is smaller than for FP.

Using the above mentioned consequences of equations (8.11) and (8.12), after calculating only S_j and TS_j, it is possible to tell whether higher-order sensitivity values for X_j do exist or not.

$$\begin{bmatrix} \color{red}{X_1^{(1)}} & \dots & \color{red}{X_j^{(1)}} & \dots & \color{red}{X_m^{(1)}} \\ \color{red}{\vdots} & & \color{red}{\vdots} & & \color{red}{\vdots} \\ \color{red}{X_1^{(n)}} & \dots & \color{red}{X_j^{(n)}} & \dots & \color{red}{X_m^{(n)}} \end{bmatrix} = \boldsymbol{A}$$

$$\begin{bmatrix} X_1^{(n+1)} & \dots & X_j^{(n+1)} & \dots & X_m^{(n+1)} \\ \vdots & & \vdots & & \vdots \\ X_1^{(2n)} & \dots & X_j^{(2n)} & \dots & X_m^{(2n)} \end{bmatrix} = \boldsymbol{B}$$

$$\begin{bmatrix} \color{red}{X_1^{(1)}} & \dots & X_j^{(n+1)} & \dots & X_m^{(n+1)} \\ \color{red}{\vdots} & & \vdots & & \vdots \\ \color{red}{X_1^{(n)}} & \dots & X_j^{(2n)} & \dots & X_m^{(2n)} \end{bmatrix} = \boldsymbol{C_1}$$

$$\vdots$$

$$\begin{bmatrix} X_1^{(n+1)} & \dots & \color{red}{X_j^{(1)}} & \dots & X_m^{(n+1)} \\ \vdots & & \color{red}{\vdots} & & \vdots \\ X_1^{(2n)} & \dots & \color{red}{X_j^{(n)}} & \dots & X_m^{(2n)} \end{bmatrix} = \boldsymbol{C_j}$$

$$\vdots$$

$$\begin{bmatrix} X_1^{(n+1)} & \dots & X_j^{(n+1)} & \dots & \color{red}{X_m^{(1)}} \\ \vdots & & \vdots & & \color{red}{\vdots} \\ X_1^{(2n)} & \dots & X_j^{(2n)} & \dots & \color{red}{X_m^{(n)}} \end{bmatrix} = \boldsymbol{C_m}$$

Figure 8.2.: Composition of $\boldsymbol{A}$, $\boldsymbol{B}$ and $\boldsymbol{C_j}$ from a set on $2n$ random numbers. The additional $\boldsymbol{C_j}$ are derived by substituting the values for $\boldsymbol{X_j}$ in $\boldsymbol{B}$ by the entries from $\boldsymbol{A}$ (shown in red). All sets are of size $(n \times m)$.

8.4.3. Limitations

For this SA approach computation time and memory become even more crucial. The evaluation of all cross terms for this SA is very time consuming. This is only partly due to the rise with m^2. Additionally, to calculate a reasonable mean value for the last term $S_{1\dots m}$ the number of runs must be at least $n = 64 \cdot (n_{par,1} \cdot \dots \cdot n_{par,m})$. This value grows very fast in m, considering that $n_{par,j}$ should be at least 8, even better 16. For a single value, with $m = 3$, $n_{par,j} = 16$ for all j and $n = 1.04 \cdot 10^6$ a full determination of all cross terms takes about 0.2 min. If $m = 4$ this value already increases to 5 min, for $m = 5$ to 11 h on a 8 core 2.66 GHz workstation with 32 GB RAM.

The fast method based on the scalar product is less computationally intensive but still grows with $n(m+2)$. The long computation time might be reduced by reducing n. The disadvantage is that the TS result appears very noisy in case of too small n. Calculating S and TS for a plan with two fields, as e.g. shown in figure 7.1 takes around 10 h for one standard evaluation with $n = 131072 = 2^{17}$ on the 8 core 2.66 GHz workstation with 32 GB RAM. Such a standard evaluation consists of $m = 4$ and a SA of several voxel and structure based quantities.

It has to be concluded that FF and TS are not fully suitable for voxel-wise calculations, however they can be reasonably used for structure-based values. Computation time in this case is approximately 1-2 h. The advantage is that a FP can be done first. If $\sum_j S_j$ is close to 1, the cross terms are not important and a calculation of TS is not necessary.

8.5. Visualizations

In this section the visualization tools developed for the SA analysis of biological models in carbon ion therapy are presented. In the previous sections it became obvious that one of the main challenges is a clear visualization. Each of the tools presented in the following allows a different access to the SA result. The combination of these methods facilitates the understanding of the consequences of uncertainties in the biological modeling process. The visualizations are based on the same example SA. The changed parameters and uncertainties are introduced with the scatterplots in the next section.

8.5.1. Scatterplots

Scatterplots result directly from the n executions of a function. The structure of figure 8.3 [21] is adapted from reference [51]. It is used to explain and access S_j values. Here, RBE is modeled with the repair-misrepair-fixation (RMF) model and is hence a function of α_x/β_x, c_1 and c_2. Uncertainties in these three input parameters are simulated with normal distributions, displayed in the histograms. Every dot in the scatterplots represents one RBE calculation, each with a different set of randomly generated input parameters. The uncertainty in the result is displayed in the horizontal histogram in the upper left frame.

Using scatterplots, the meaning of S can be explained in terms of correlation. There are three different S values in figure 8.3. The smallest is $S(\alpha_x/\beta_x) \approx 0.03$. A change in this parameter has almost no impact on the uncertainty of RBE. There is no correlation in the corresponding scatterplot. For the next $S(c_2) \approx 0.17$, there is already a small trend: A change to higher c_2 is more probable to result in a higher RBE. In this example, c_1 has the highest impact on the uncertainty in RBE. There is a clear correlation that higher c_1 results in higher RBE. This is also reflected in the large $S(c_1) \approx 0.80$. In addition, $S(\alpha_x/\beta_x) + S(c_1) + S(c_2) \approx 1$. This indicates that there are no cross terms for this example.

Scatterplots are an intuitive way to access sensitivity values. Due to the fact that they can represent only limited amount of data at once, scatterplots are most useful in case of structure-based measures. Nevertheless, the detail which they provide is also useful for voxel-wise SAs. One scenario for example is to evaluate 3-D maps, as it is done in the next section and then “zoom in” for detailed, scatterplot-based representation for selected voxel.

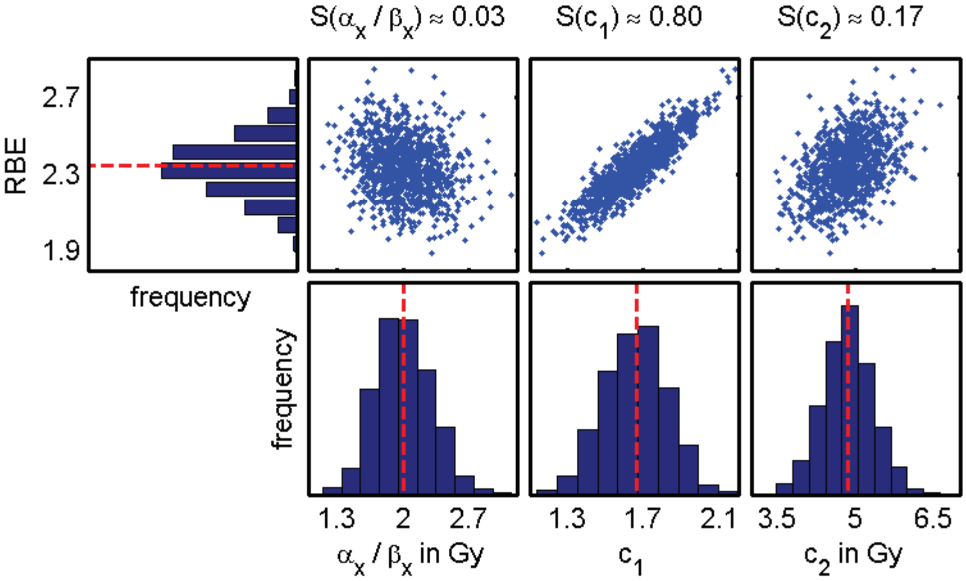

Figure 8.3.: Scatterplot illustration of an example SA of RBE as a function of α_x/β_x, c_1 and c_2. Their uncertainty is simulated using normal distributions with a standard deviation of 15% for α_x/β_x and of 10% for c_1 and c_2 respectively. The standard deviations are relative to the mean value, which is marked with a dashed red line in the histograms. The here indicated mean values are the unchanged results of a biological optimization. A subset of 1000 runs is displayed in the scatter plots. The sensitivity S of RBE on the three input parameters is marked on top of the respective scatter plot. The physical dose is kept constant at $d = 1.28$ Gy.

8.5.2. 3-D Sensitivity Analysis

Figure 8.4 shows axial slices of a 3-D map displaying the SA result. Similar to the dose distribution, S and TS values are displayed in color maps on top of the patient CT. Here RWD was calculated as a function of α_x/β_x, c_1 and c_2. The treatment plan is the same as in figure 7.1 on page 42. Several structures are drawn in the figures: the planning target volume (PTV) in red, the left optic nerve in green, the left eyeball in orange and left lens in brown.

In addition to the RWD distribution (panel A in figure 8.4), its uncertainty is shown in terms of a standard deviation in panel B. The spatial distributions of the unchanged input parameters are shown in panels D-F. For these sensitivity maps, S and TS are calculated voxel-wise. This offers the potential to see spatial distributions in S and TS. If a voxel of interest is selected, it is always possible to “zoom in” to a scatterplot representation, providing more detailed information.

Note the effect of noise for the TS values. If TS is small (in the PTV in panel J, distal to the PTV in panel K and in the end of the fragmentation tail in panel L), TS might numerically be negative and not displayed in the color maps, as they are limited to $0 \leq TS \leq 1$. Typically, the negative values range in the order of 0 to -0.05. Using higher n could solve this problem, but this approach is limited by computation time.

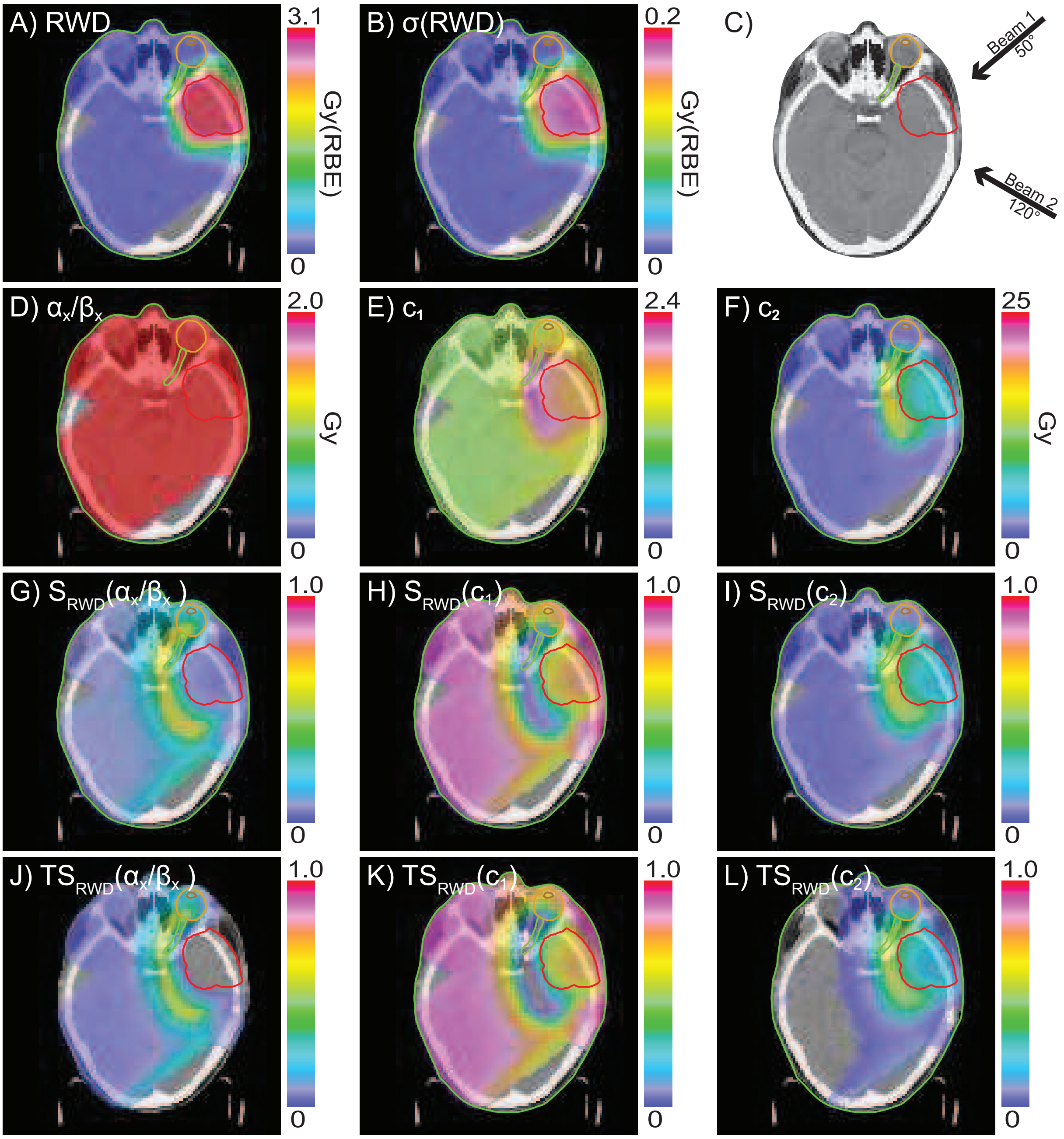

Figure 8.4.: Axial slice of a voxel-wise SA. The optimization of this astrocytoma tumor case was described in section 7.4 on page 41. The panels depict: the optimization result (A), its uncertainty in terms of a standard deviation (B), the beam geometry (C) and the three (unchanged) distributions of the input parameters (D-F). The voxel-wise S maps (G-I) are displayed together with the TS maps (J-L). Several structures are marked in colors (cf. panel C): PTV(red), left optic nerve (green), left eyeball (orange) and left lens (brown). The sensitivities are calculated with $n = 1.04 \cdot 10^6$ and normally distributed random numbers for the input parameters. A standard deviation of 15% was used for α_x/β_x and of 10% for c_1 and c_2 respectively.

8.5.3. Sensitivity-Volume Histograms

In the previous section, axial slices of 3-D sensitivity maps were shown. Similar to the DVH approach, described in section 7.5.1 on page 43, the 3-D information for one structure can be compressed. This is possible for both S and TS (Sensitivity-Volume Histogram (SVH) and Total Sensitivity-Volume Histogram (TSVH) respectively). Figure 8.5 shows an example of a SVH (panel A) and a TSVH (panel B) for uncertainties in RWD. The SVH is obtained for the PTV. It contains the information about the frequency of the S values for all voxel in the structure. Hence, the SVH can reveal, which input uncertainty affects the result of a structure the most. In the example SVH (panel A), the change of c_1 has the greatest impact on the RWD distribution inside the PTV.

The TSVH (panel B) is plotted for the left lens. The lens is shown in brown in figure 8.4. It is a small structure, but illustrates best one of the advantages of the FF approach. The TSVH shows that $TS_{RWD}(c_2) < 0.05$ in all voxel inside this structure. Hence c_2 could be set constant in these voxel as the change in the RWD is not caused by this input uncertainty. TSVHs can be analyzed for every structure. Due to limited n and the resulting noise in TS, there might be negative values in some voxel (cf. figure 8.4 panel J-L). Here the structure of the left lens was chosen, because it illustrates the possibility of FF and all $TS > 0$ for all voxel in this structure.

Similar to the DVHs in section 7.5.1, the SVHs and TSVHs contain basic information like minimum, maximum, median and mean (total) sensitivity for a structure.

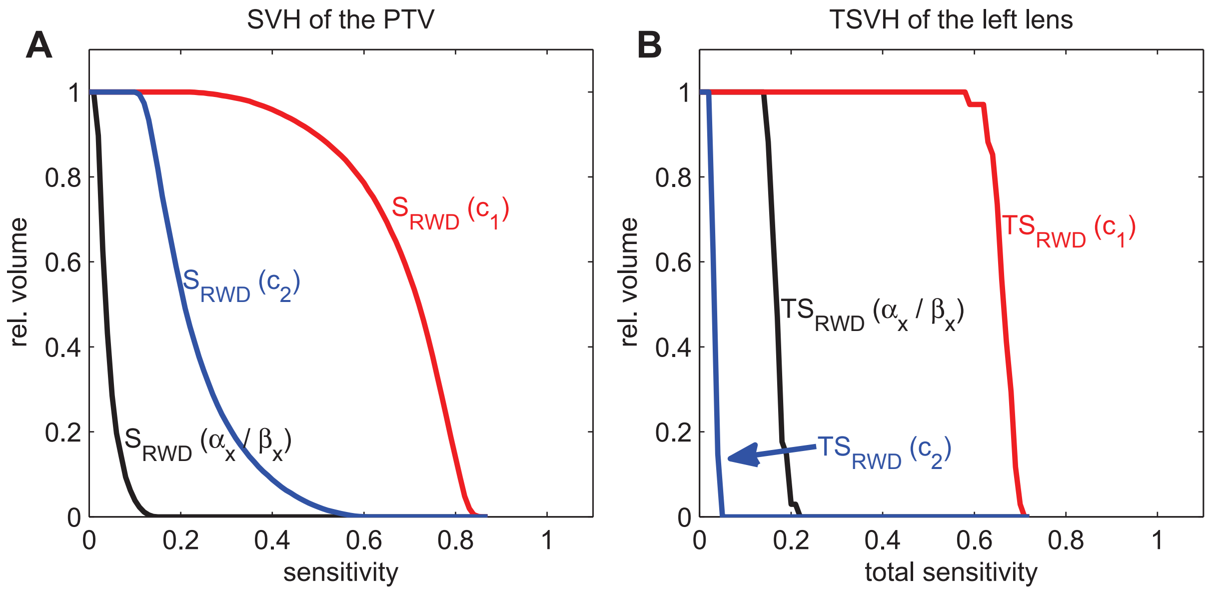

Figure 8.5.: Sensitivity- and total sensitivity-volume histograms. The SVH in panel A is evaluated for the PTV. The uncertainty in input parameter c_1 has the greatest impact throughout all voxel contained in the PTV. The TSVH in panel B is shown for the left lens. It illustrates the FF approach. $TS_{RWD}(c_2) < 0.05$ for all voxel in this structure. The uncertainty in c_2 has no impact on the uncertainty in the RWD, hence c_2 can be set constant for this OAR. The shown histograms are derived from the example sensitivity analysis shown in figure 8.4 page 59. The color maps there show the spatial variation of S and TS.

8.5.4. DVH-Probability Plots

The Monte Carlo execution of treatment plans in the FP and FF approach makes it possible to add probability statements to RWDVHs. An example is shown in figure 8.6. The RWDVH is calculated individually for every run. Based on this data, standard deviations can be added to the RWDVH of the optimized treatment result. Using standard deviations, the probability that the RWDVH of a treatment plan lies in a particular area is added to the RWDVH. In this case, 68.3% of the treatments lie in the dark area, 95.4% in the combination of light and dark areas.

To demonstrate their uncertainties, the RWDVHs of the PTV and the left optic nerve are extended by these probability statements. Both structures are drawn in figure 8.4. Panel A of this figure depicts the optimization result. Its RWDVH is shown in black in figure 8.6. The left optic nerve is chosen as a representative OAR. It lies distal to the PTV in an area with a relatively high RWD. With the given uncertainties in the input parameters, uncertainties are added to RWDVHs. It is desirable to see uncertainties in a RWDVH as the concept of RWDVH is the most common tool for treatment plan evaluation.

The measure $\mathrm{RWD}_{\mathrm{Vol}}$ allows to examine the composition of the standard deviation in the RWDVH-probability plots. An example of a SA result for $\mathrm{RWD}_{98\%}$ is shown in figure 8.6. It shows the composition of the uncertainty in the minimum RWD which 98% of the structure receive. In the PTV an uncertainty in c_1 has the greatest impact, whereas in the optic nerve the uncertainty in α_x/β_x is the most prominent. The SA of $\mathrm{RWD}_{\mathrm{Vol}}$ can be done for arbitrary relative volumes. This includes 0 and 100%, representing maximum and minimum RWD respectively.

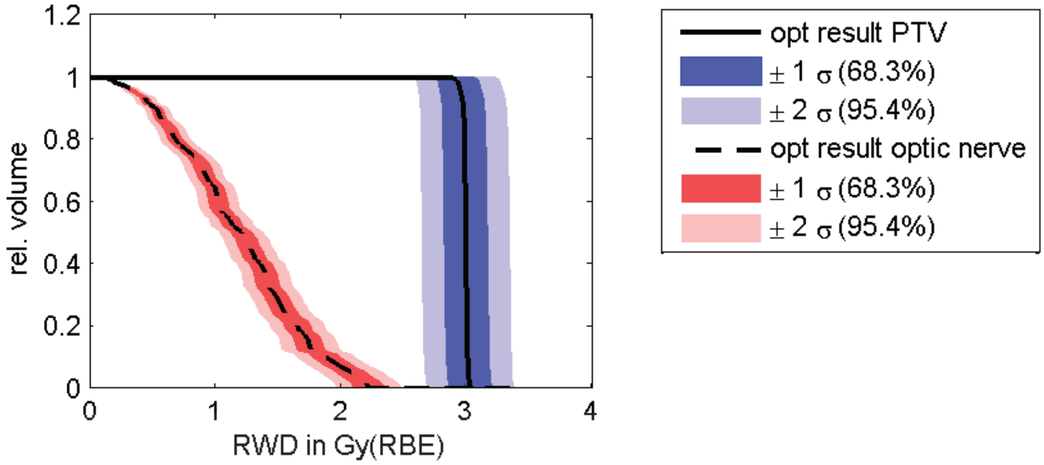

	α_x/β_x	c_1	c_2
PTV $\mathrm{S}_{\mathrm{RWD}_{98\%}}$	0.06	0.60	0.32
opt nerve $\mathrm{S}_{\mathrm{RWD}_{98\%}}$	0.55	0.10	0.29

	α_x/β_x	c_1	c_2
PTV $\mathrm{TS}_{\mathrm{RWD}_{98\%}}$	0.06	0.60	0.32
opt nerve $\mathrm{TS}_{\mathrm{RWD}_{98\%}}$	0.57	0.11	0.30

Figure 8.6.: RWDVH-probability plot for two representative structures. This plot combines the RWDVH from the optimization result with its uncertainty, caused by uncertain input parameters. The colored areas represent probabilities that a RWDVH line is contained in it. They are determined with the standard deviation. 68.3% of the RWDVHs lie in the dark area ($\pm 1\sigma$), 95.4% in the union of the light and the dark area ($\pm 2\sigma$). S and TS for the $\mathrm{RWD}_{98\%}$ are tabulated for both structures. The SA of $\mathrm{RWD}_{\mathrm{Vol}}$ describes the composition of the uncertainty. It can be calculated for arbitrary relative volumes.

Part IV.

Impact of Uncertainties in Biological Dose Response Models on Carbon Ion Treatment Plans

In this part the SA is applied to the uncertainties in biological response modeling for carbon ion therapy. Based on the sensitivity approaches and their visualization, RMF model and LEM1 predictions are analyzed. To perform these analyses, first the sets of default uncertainty distributions are summarized in chapter 9. The distributions are assigned to the uncertain input parameters. SA results are presented for several biological models, treatment scenarios and measures for treatment plan evaluation. In chapter 10 a comprehensive SA for the RMF model is presented. This includes the evaluation of reductions and increases in the assigned uncertainties. The SAs of LEM1 and RMF model based treatment plans are compared for different scenarios in chapter 11. The SA for the calculation of tumor control probabilities is presented in chapter 12. The consequences on carbon ion treatment planning and evaluation are concluded in the chapter 13.

9. Evaluated Uncertainty Settings

Several uncertainty sets are evaluated within the scope of this work. The decision which set is used depends on the objective of the evaluation and the biological model used. For example, it is possible to perform a comprehensive SA for the repair-misrepair-fixation (RMF) model. This means, uncertainties can be assigned to x-ray reference parameters as well as to the biological modeling process. Throughout this work only tabulated data for the local effect model (LEM1) predictions are available and not the source code itself. Thus only a subset of parameters can be changed consistently. Note, that the implemented sensitivity approaches can in general be applied to a comprehensive analysis of LEM1 predictions, presuming the modeling process itself is available and not the tabulated results. Default values for the uncertainties are shown here. In certain cases the effect of changing uncertainties is evaluated. Deviations from these default values are indicated if applied.

The same set of relative random numbers is used for all voxel during the execution of the SA. This can be achieved by normally distributed random numbers with a mean value of one. The resulting random numbers are multiplied by the chosen parameters. Consequently, the mean value of the uncertain input parameter is the value used for the optimization. An example explaining these relative random numbers is shown later in section 12. For the demonstration of the SA, all uncertainties are modeled as normally distributed within the scope of this thesis.

Table 9.1 displays the default uncertainties for different evaluated functions types. The function Y represents the examined values which are influenced by a set of input parameters. The first two columns are only applicable for the RMF model, as c_1 and c_2 are unique for it (cf. section 6.2 on page 28). In the framework of the RMF model, RBE is a function of α_x/β_x. Column two of table 9.1 shows that the two uncertainties in α_x and β_x are combined to an uncertainty of their ratio. The division of two normal distributions needed here can be done as e.g. shown in the Appendix of Friedrich *et al.* [52]. The used standard deviation of 15% for α_x/β_x within the scope of his SA is a sufficiently good approximation.

The LEM1 data available for this work are tabulated for only a small number of combinations of α_x and β_x. This limits the possibility of the variance-based SA approaches. The used uncertainty sets for a SA of LEM1 based treatment plans are shown in columns three, four and five. Several assumptions need to be made for these partial SAs as the Monte Carlo SA approaches FP and FF need independent input variables. This is in general not the case for biological models, as α_p and β_p depend on α_x and β_x. The assumptions needed for columns three, four and five are further explained when they are applied in chapter 11.

$Y(\alpha_x, \beta_x, d, c_1, c_2)$	$Y(\alpha_x/\beta_x, d, c_1, c_2)$	$Y(\alpha_x, \beta_x, d)$	$Y(\alpha_p, \beta_p, d)$	$Y(\alpha_x, \beta_x, \alpha_p, \beta_p, d)$
$\sigma(\alpha_x) = 10\%$	$\sigma(\alpha_x/\beta_x) = 15\%$	$\sigma(\alpha_x) = 10\%$	$\sigma(\alpha_p) = 10\%$	$\sigma(\alpha_x) = 10\%$
$\sigma(\beta_x) = 10\%$		$\sigma(\beta_x) = 10\%$	$\sigma(\alpha_p) = 10\%$	$\sigma(\beta_x) = 10\%$
$\sigma(d) = 5\%$	$\sigma(d) = 5\%$	$\sigma(d) = 5\%$	$\sigma(d) = 5\%$	$\sigma(\alpha_p) = 10\%$
$\sigma(c_1) = 10\%$	$\sigma(c_1) = 10\%$			$\sigma(\beta_p) = 10\%$
$\sigma(c_1) = 10\%$	$\sigma(c_1) = 10\%$			$\sigma(d) = 5\%$

Table 9.1.: Default uncertainties assigned to the input parameters. Column one and two are only applicable for the RMF model. A typical measure for the first column is the tumor control probability $TCP(\alpha_x, \beta_x, d, c_1, c_2)$. With the second column RBE, RWD and EQD2 can be evaluated. The standard deviation $\sigma(\alpha_x/\beta_x) = 15\%$ is derived from $\sigma(\alpha_x) = 10\%$ and $\sigma(\beta_x) = 10\%$. Columns three, four and five can be used for both LEM1 and RMF model calculations. Additional assumptions need to be made. They are introduced in chapter 11 where they are applied. Note, that there are cases where the dependency of Y on the dose or further parameters is not necessary. This is for instance the case in section 10.1. Here the first column is reduced to $Y\,(\alpha_x, \beta_x, c_1, c_2)$ or $Y\,(\beta_x, c_1)$. The corresponding uncertainties in e.g. d, α_x or c_2 are neglected if necessary.

10. Comprehensive SA for RMF Model Predictions

The RMF model is suitable for a comprehensive SA, because the biological modeling process is very fast. This feature has already been described by introducing c_1 and c_2 in section 7.1 on page 37. It facilitates the high number of executions of the biological modeling process, needed for the SA. RBE and hence RWD calculations are very fast in every voxel. Several examples for a comprehensive SA with the RMF model are discussed in the next sections. The SA for the result of the biological modeling ($\alpha_p\left(\alpha_x, \beta_x, c_1, c_2\right)$ and $\beta_p\left(\beta_x, c_1\right)$) is presented in section 10.1. The comprehensive SA, including uncertainties in α_x, β_x, c_1, c_2 and d is discussed in section 10.2. The influence of reduced or increased uncertainties is evaluated in section 10.3.

10.1. Sensitivity Analysis for α_p and β_p

The first step towards a comprehensive SA for RMF model based RBE predictions is to analyze the biological modeling process itself. This means to examine α_p and β_p in respect to their dependencies on input parameters. According to equations (7.5) and (7.6) on page 38, $\alpha_p\left(\alpha_x, \beta_x, c_1, c_2\right)$ and $\beta_p\left(\beta_x, c_1\right)$ can be written as functions of four or two input parameters respectively. Relative standard deviations of 10% are assigned to the four input parameters.

Figure 10.1 shows the result for this SA in case of x-ray reference parameters $\alpha_x = 0.1$ Gy^{-1} and $\beta_x = 0.05$ Gy^{-2} as used for chordoma of the skull base [30]. The modeled unchanged α_p and β_p are shown in panels A and B. Both increase with increasing LET. The spatial distribution of LET is shown in panel C of figure 10.1. The resulting standard deviations of α_p and β_p (panels D and E) show the same behavior as α_p (panel A) and β_p (panel B) respectively. Their relative standard deviation (derived by “dividing panel D by panel A” or “panel E by panel B”) ranges from 10.1% to 12.4% for α_p and is spatially constant at 22.6% for β_p respectively. Together with the spatial sensitivity distribution, these aspects are explained in the following.

Panels G, H, J and K show the corresponding sensitivity maps for α_p. Several relations can be observed directly. $S_{\alpha_p}\left(\alpha_x\right)$ is equal to $S_{\alpha_p}\left(c_1\right)$ and $S_{\alpha_p}\left(\beta_x\right)$ is equal to $S_{\alpha_p}\left(c_2\right)$. This is a direct consequence of the assigned relative standard deviations and the calculation of $\alpha_{p,i} = \alpha_{x,i} \cdot c_{1,i} + \beta_{x,i} \cdot c_{2,i}$ in equation (7.5). For example, considering the first term of the sum, a relative change of +10% in either α_x or c_1 results in a multiplication by 1.1. Changes in the second term of the sum can be explained analogously with β_x and c_2. The spatial distribution in the sensitivity maps is different for panels G and J (or H and K). α_p is more dependent on changes in α_x and c_1 in voxel with lower LET (compare also to the c_1 and c_2 panels displayed in figure 8.4 on page 59). For high LET regions, uncertainties in β_x and c_2 have a higher impact. The combination of multiplications and a sum in the

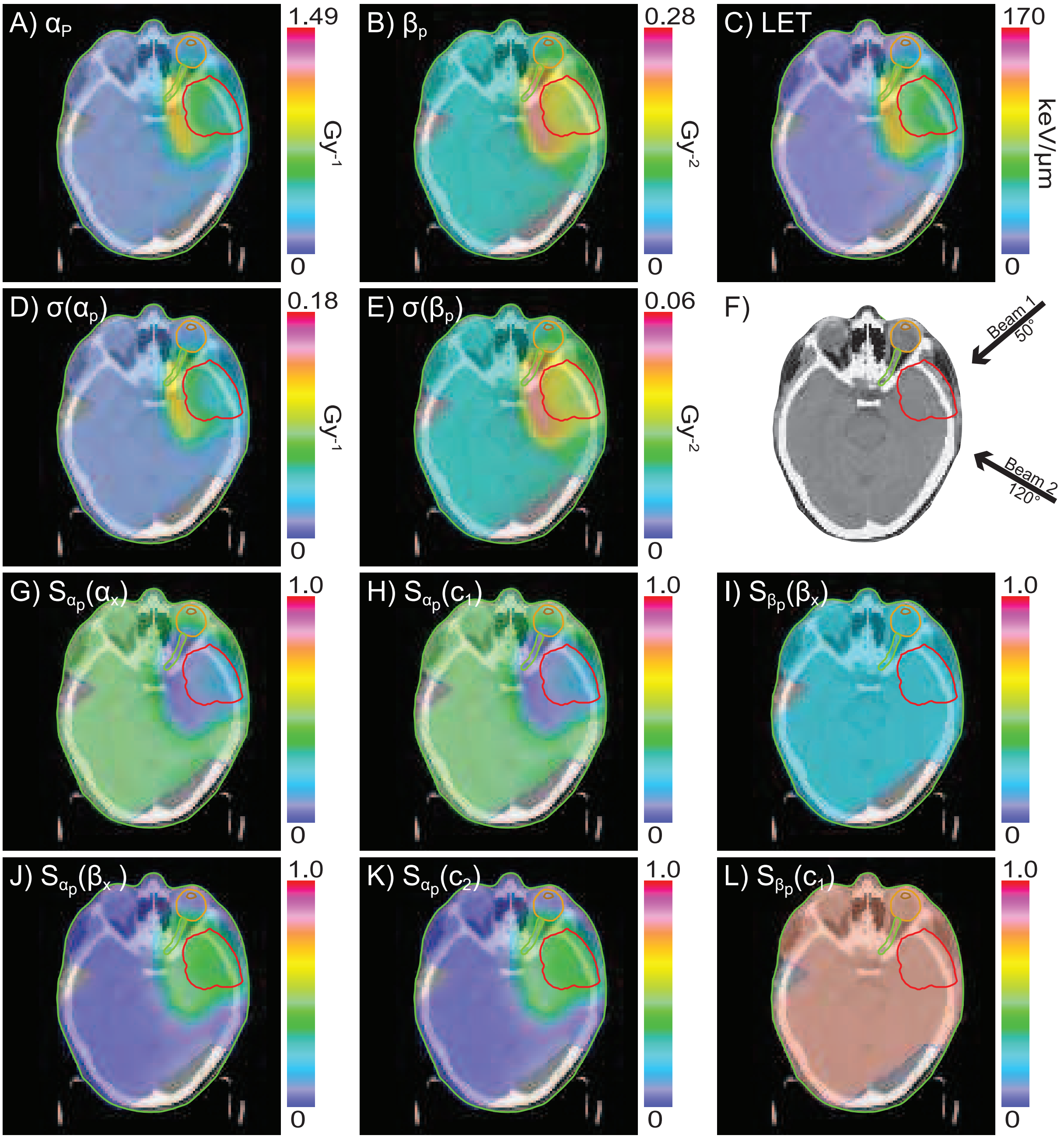

Figure 10.1.: SA of α_p and β_p for RMF model predictions. The panels show the modeled α_p and β_p together with their resulting standard deviation (panels A, B, D and E). Panels C and F show a LET map and the simulated beam geometry respectively. The six sensitivity maps, four for α_p and two for β_p, are shown in panels G-L. The underlying treatment plan, including a spatial distribution of c_1 and c_2, is displayed in figure 8.4 on page 59. The relative standard deviation of the input parameter distributions are 10% for each of the four changed inputs parameters. The planning target volume (PTV) is marked in red, the left optical nerve in green together with the left eyeball (orange) and the left lens (brown).

calculation of α_p also leads to spatial variations in the relative change ($\sigma\left(\alpha_p\right)/\alpha_p$ ranges from 10.1% to 12.4%).

The SA of β_p is shown in panels I and L. The uncertainty in c_1 has a higher impact on the uncertainty in β_p. Considering equation (7.6), β_p can be calculated as $\beta_{p,i} = \beta_{x,i} \cdot \left(c_{1,i}\right)^2$. The square of c_1 results in the higher impact of changes in c_1. The spatially constant sensitivity values result from the relative changes, which are applied to all voxel in the same way. Nevertheless this allows spatial variations of $\sigma\left(\beta_p\right)$ (panel E). Only the relative change $\sigma\left(\beta_p\right)/\beta_p$ and the sensitivity of this change in β_p are spatially constant.

10.2. Comprehensive Sensitivity Analysis

The RMF model predictions allow a comprehensive SA. Comprehensive in this context means, that in total three sources of uncertainty are considered: first, biological uncertainties in the reference x-ray parameters α_x and β_x, second, uncertainties in the biological modeling process represented by c_1 and c_2 and third, an uncertainty in the physical dose d. Within the scope of this thesis, this comprehensive SA can only be performed for the RMF model, due to the advantages of the c_1 and c_2 formalism. This formalism allows very fast RBE predictions with changing parameters. Similar comprehensive SA approaches for the LEM1 and the reason why it was not feasible to implement them are topic of chapter 11.

The comprehensive SA is demonstrated based on two different cell lines. One has a small $\alpha_x/\beta_x = 2$ Gy ($\alpha_x = 0.1$ Gy^{-1} and $\beta_x = 0.05$ Gy^{-2}). This cell line is commonly used for chordoma of the scull base [30]. The second cell line has a greater $\alpha_x/\beta_x = 9.2$ Gy ($\alpha_x = 0.184$ Gy^{-1}, $\beta_x = 0.02$ Gy^{-2}). These values were obtained for Chinese hamster fibroblast, V79 [41].

In the framework of the RMF model, RWD can be calculated as a function of α_x/β_x, d, c_1 and c_2. The next double page shows axial slices of the 3-D sensitivity maps for a comprehensive SA of two exemplified cell lines. Figure 10.2 shows the result for $\alpha_x/\beta_x = 2$ Gy, figure 10.3 for $\alpha_x/\beta_x = 9.2$ Gy. In both figures the optimized RWD (panel A) is displayed together with its uncertainty (panel D). The LET (panel B) and the beam geometry (panel E) are shown together with the four unchanged input parameter maps (panels C, G-I). The four corresponding sensitivity maps are shown in panels F, J-L.

Considering the small $\alpha_x/\beta_x = 2$ Gy in figure 10.2 several relations can be observed. The impact of changing d is almost constant spatially with $S_{RWD}\left(d\right) \approx 0.3$. The $S_{RWD}\left(\alpha_x/\beta_x\right)$ is small throughout the patient except in the region 1 to 2.5 cm distal to the PTV. In this region $S_{RWD}\left(\alpha_x/\beta_x\right)$ reaches values up to 0.5. This means that the uncertainty in α_x/β_x has the greatest impact on the uncertainty in RWD in this region. The sensitivity maps of the two biological modeling parameters c_1 and c_2 show opposite behavior: $S_{RWD}\left(c_1\right)$ is up to 0.7 in the PTV and in the fragmentation tail far from the PTV. In the region 0 to 2.5 cm distal to the PTV it drops to very small values $S_{RWD}\left(c_1\right) \leq 0.05$, whereas $S_{RWD}\left(c_2\right)$ is small everywhere except the PTV $S_{RWD}\left(c_2\right) \approx 0.15$ and the mentioned region from 0 to 2.5 cm distal to the PTV ($S_{RWD}\left(c_2\right) \approx 0.4$).

The high values in $S_{RWD}\left(\alpha_x/\beta_x\right)$ and $S_{RWD}\left(c_2\right)$ and the corresponding low $S_{RWD}\left(c_1\right)$ are in regions of high LET. A strong LET dependency can already be seen for the unchanged c_1 and c_2. This dependency on LET in combination with the changing sensitivity is of interest, especially if an organ at risk (OAR) lies in this region. In the presented patient case the left optic nerve, marked in green in the panels, is located in the region of high LET. The uncertainty in the α_x/β_x is more crucial for this OAR than for the PTV. The

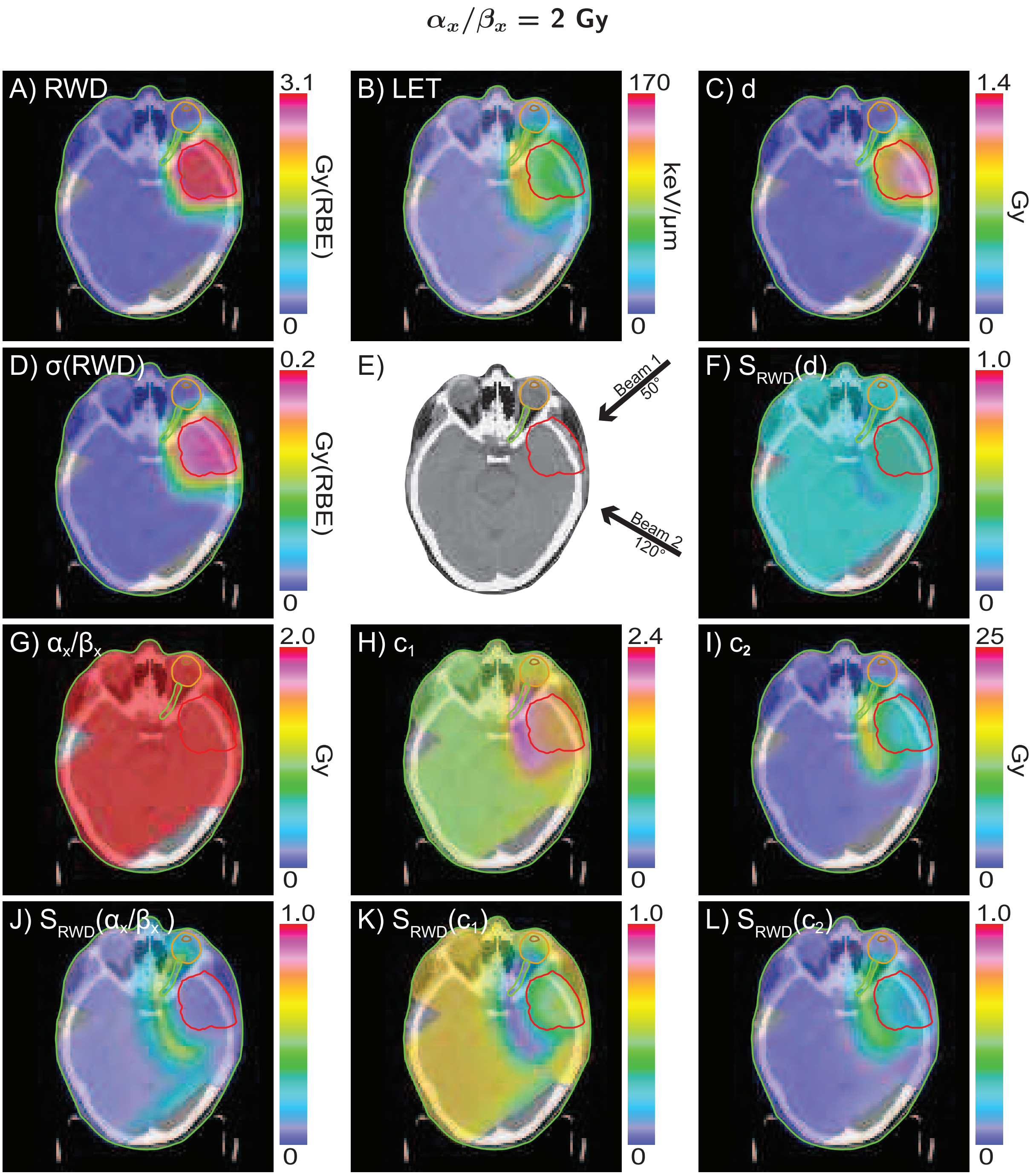

Figure 10.2.: Comprehensive SA for $\alpha_x/\beta_x = 2$ Gy. RWD is a function of α_x/β_x, d, c_1 and c_2. The optimized RWD (panel A) is displayed together with its uncertainty $\sigma\,(RWD)$ (panel D). The LET (panel B) and the beam geometry (panel E) are shown together with the four unchanged input parameter maps (panels C, G-I). The four sensitivity maps are shown in panels F, J-L. The planning target (PTV) volume is marked in red, the left optical nerve in green together with the left eyeball (orange) and the left lens (brown).

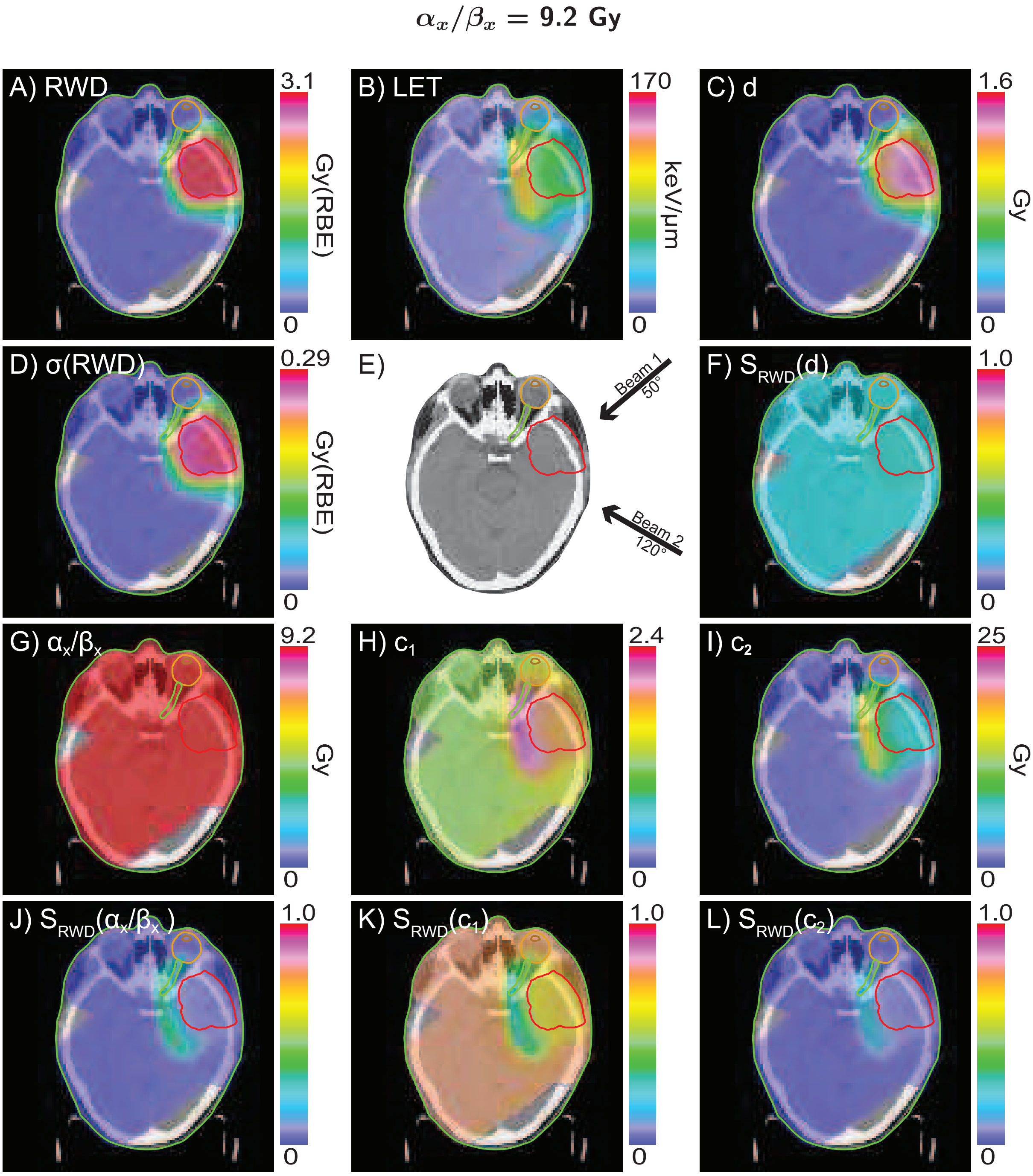

Figure 10.3.: Comprehensive SA for $\alpha_x/\beta_x = 9.2$ Gy. RWD is a function of α_x/β_x, d, c_1 and c_2. The optimized RWD (panel A) is displayed together with its uncertainty $\sigma\,(RWD)$ (panel D). The LET (panel B) and the beam geometry (panel E) are shown together with the four unchanged input parameter maps (panels C, G-I). The four sensitivity maps are shown in panels F, J-L. The planning target volume (PTV) is marked in red, the left optical nerve in green together with the left eyeball (orange) and the left lens (brown).

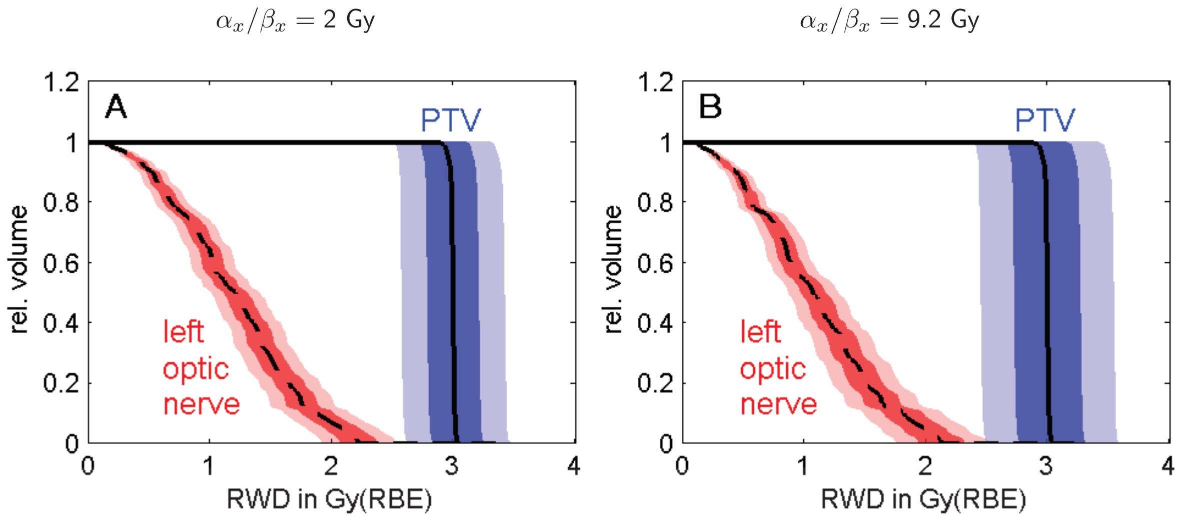

PTV	α_x/β_x	d	c_1	c_2
$S_{RWD\,2\%}$	0,04	0,31	0,43	0,21
$S_{RWD_{50\%}}$	0,03	0,31	0,49	0,17
$S_{RWD_{98\%}}$	0,05	0,31	0,42	0,23

optic nerve	α_x/β_x	d	c_1	c_2
$S_{RWD\,2\%}$	0,14	0,28	0,17	0,42
$S_{RWD_{50\%}}$	0,29	0,22	0,08	0,42
$S_{RWD_{98\%}}$	0,49	0,16	0,09	0,25

PTV	α_x/β_x	d	c_1	c_2
$S_{RWD\,2\%}$	0,06	0,27	0,62	0,06
$S_{RWD_{50\%}}$	0,04	0,26	0,66	0,04
$S_{RWD_{98\%}}$	0,05	0,26	0,63	0,06

optic nerve	α_x/β_x	d	c_1	c_2
$S_{RWD\,2\%}$	0,15	0,27	0,47	0,12
$S_{RWD_{50\%}}$	0,25	0,25	0,37	0,14
$S_{RWD_{98\%}}$	0,19	0,23	0,47	0,08

Figure 10.4.: Probability RWDVH for the PTV and the left optic nerve for two different α_x/β_x values: $\alpha_x/\beta_x = 2$ Gy panel A and $\alpha_x/\beta_x = 9.2$ Gy panel B. In these plots, uncertainties are added to the optimization result (solid and dashed black lines). The uncertainties in the RWDVH are indicated as $\pm\sigma$ (68.3% lie inside the dark area) and $\pm 2\sigma$ (95.4% lie inside the combination of light and dark area). The tables present the SA result for $S_{RWD_{Vol}}$. The PTV and the left optic nerve are evaluated for three representative relative volumes. An axial slice of the shown example SA is presented in figure 10.2 for $\alpha_x/\beta_x = 2$ Gy and in figure 10.3 for $\alpha_x/\beta_x = 9.2$ Gy.

part of the biological modeling represented by c_1 on the other hand shows the highest impact on the uncertainty of RWD in the PTV but only a small impact on the uncertainty of RWD in the left optic nerve.

The corresponding SA for $\alpha_x/\beta_x = 9.2$ Gy with the same set of relative uncertainties in the input parameters is shown in figure 10.3. This SA has the same trends as the ones described for $\alpha_x/\beta_x = 2$ Gy. The main deviations are a generally higher uncertainty in the RWD and a greater $S_{RWD}\,(c_1)$. The sensitivity values for α_x/β_x and c_2 are accordingly smaller.

The differences between $\alpha_x/\beta_x = 2$ Gy and $\alpha_x/\beta_x = 9.2$ Gy are further examined in figure 10.4. Here the probability RWDVHs of both SA are shown. The uncertainty for $\alpha_x/\beta_x = 2$ Gy (panel A) is smaller than for $\alpha_x/\beta_x = 9.2$ Gy (panel B). The tables show $S_{RWD_{Vol}}$ values. In this example three representative relative volumes were chosen. Comparing the values for the PTV, one can see the above described observation that c_1 becomes more important for $\alpha_x/\beta_x = 9.2$ Gy, whereas the uncertainty of c_2 is less important.

Comparison of the $S_{RWD_{Vol}}$ values for PTV and the left optic nerve demonstrates that different structures can have very different SA results. Depending on the location of the structure, different input parameter uncertainties might have a different impact. In this case, α_x/β_x and c_2 are more important for the left optic nerve than for the PTV. For c_1 and d it is the opposite. This is valid for both cell lines and was already observed in the axial slices of the 3-D sensitivity maps in figures 10.2 and 10.3.

Summing up $S\left(\alpha_x/\beta_x\right) + S\left(d\right) + S\left(c_1\right) + S\left(c_2\right) \approx 1$ for all $S_{RWD_{Vol}}$ and both cell lines. This means, that there are no cross terms in this case. The total sensitivity is equal to the first order sensitivity values ($TS = S$).

10.3. Influences of Reduced or Increased Uncertainties

In this section the influence of an uncertainty reduction or increase is demonstrated. The SA is executed with changed uncertainty distributions for the four input parameters α_x/β_x, d, c_1 and c_2. Their default uncertainties were introduced in chapter 9 on page 67. There are many possibilities to change the uncertainties in the input parameters. Independent of each other, each of them can be lower or higher than their default values. In addition, any input parameter can be removed from the SA by assigning no uncertainty to it. In figure 10.5 the probability RWDVH of the default uncertainty setting (panel A) is shown together with the result of three representative scenarios.

The first scenario is the reduction of all four input uncertainties by a factor of two ($\sigma\left(\alpha_x/\beta_x\right) = 7.5\%$, $\sigma\left(d\right) = 2.5\%$, $\sigma\left(c_1\right) = 5\%$ and $\sigma\left(c_2\right) = 5\%$) which is shown in panel B. A 5% relative standard deviation might not represent the actual uncertainties of the biological parameters (cf. chapter 3 on page 11). Nevertheless, this scenario shows the potential of more precise determination of biological parameters. There is a considerable decrease in the uncertainty of the RWDVH for the reduced uncertainties (panel B) compared to the default uncertainties in (panel A). The smaller the input uncertainties the less uncertain is the result.

The second scenario (panel C), is the opposite of the first scenario. The default uncertainty values are doubled ($\sigma\left(\alpha_x/\beta_x\right) = 30\%$, $\sigma\left(d\right) = 10\%$, $\sigma\left(c_1\right) = 20\%$ and $\sigma\left(c_2\right) = 20\%$). This results in a much higher uncertainty in the RWDVHs. Cross terms also known as higher order sensitivity values do not occur in this scenario, although their appearance is more likely for larger input uncertainties. These higher order sensitivity values describe the interplay effect of two input uncertainties. They were introduced along with the total sensitivity analysis in section 8.4. $\mathrm{RWD_{Vol}}$ values (data not shown) are similar to the values of the default settings (cf. figure 10.4, panel A).

In the third scenario the uncertainty in the dose is removed (panel D). This can be interpreted as the assumption that the delivered dose is exactly equal to the planned (optimized) dose. The uncertainty of the RWDVH of panel D is only slightly smaller than the default values. Thus eliminating all physical dose uncertainties will not lead to a precise treatment result. The uncertainties in the biological parameters have a large impact on the uncertainty in the RWD distribution and hence on general treatment outcome. Note, that this third scenario is equivalent to the SA shown in the visualization example in section 8.5. Figure 8.4 on page 59 shows the corresponding axial slices of the 3-D maps.

A further scenario, in which $\sigma\left(c_1\right) = 0$ and $\sigma\left(c_2\right) = 0$ is discussed in the next chapter. There $\sigma\left(c_1\right)$ and $\sigma\left(c_2\right)$ are removed from the SA in order to compare SAs for treatment plans based on both LEM1 and RMF model predictions.

default uncertainties

reduced uncertainties (halved)

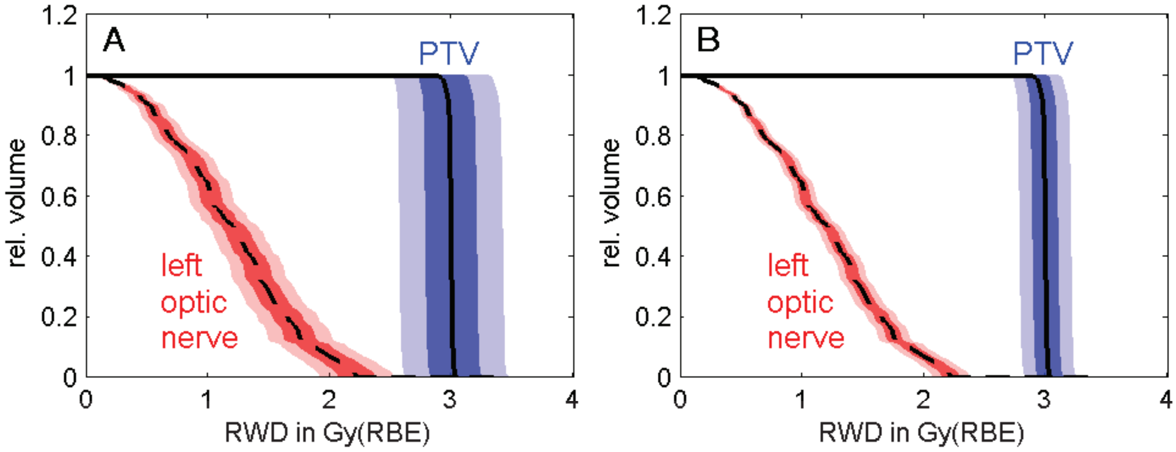

increased uncertainties (doubled)

no uncertainty in d $(\sigma(d) = 0)$

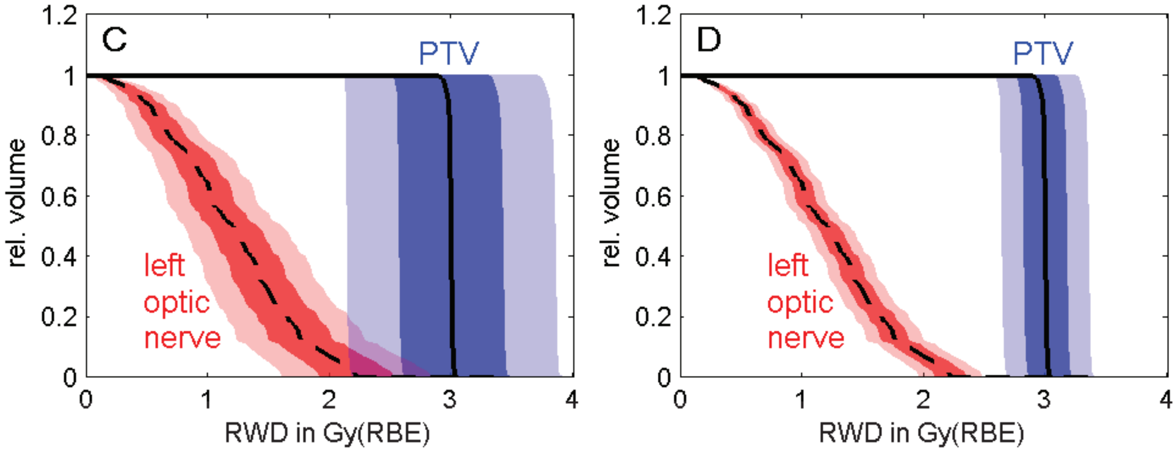

Figure 10.5.: This figure demonstrates the impact of changes in the uncertainty distributions. The optimization result shown by a solid and a dashed black line is calculated with unchanged input parameters. The uncertainties in the RWDVH of the left optic nerve and the planning target volume (PTV) are indicated as $\pm\sigma$ (68.3% lie inside the dark area) and $\pm 2\sigma$ (95.4% lie inside the combination of light and dark area). Panel A shows the result for the default uncertainty set ($\sigma(\alpha_x/\beta_x) = 15\%$, $\sigma(d) = 5\%$, $\sigma(c_1) = 10\%$ and $\sigma(c_2) = 10\%$). In panel B the uncertainties are halved ($\sigma(\alpha_x/\beta_x) = 7.5\%$, $\sigma(d) = 2.5\%$, $\sigma(c_1) = 5\%$ and $\sigma(c_2) = 5\%$). In panel C they are doubled ($\sigma(\alpha_x/\beta_x) = 30\%$, $\sigma(d) = 10\%$, $\sigma(c_1) = 20\%$ and $\sigma(c_2) = 20\%$). Panel D shows the probability plots in case that no uncertainty is assigned to the dose d ($\sigma(\alpha_x/\beta_x) = 15\%$, $\sigma(d) = 0$, $\sigma(c_1) = 10\%$ and $\sigma(c_2) = 10\%$).

11. Partial Sensitivity Analysis for LEM1 and RMF Model Predictions

In this chapter, the SA is applied to the LEM1 as well. Within the scope of this thesis, LEM1 predictions of α_p and β_p are obtained from the implementation by INFN (Istituto Nazionale di Fisica Nucleare) and I-SEE (Internet - Simulation, Evaluation, Envision) which are available online* [32]. In this database, tabulated α_p and β_p are available for 15 different α_x and β_x values. Due to this tabulation it is not possible to change α_x and β_x by arbitrary uncertainties and obtain a new set of α_p and β_p values for the LEM1. Note, that if for instance the source code of the LEM1 is available, it is possible to perform a comprehensive SA for LEM1 predictions. Computation time is likely to be a limiting factor in this scenario.

The executed variance-based SA requires independent input parameters (cf. section 8.3 on page 51). The consequence within the scope of this thesis is that the general function $RBE\left(\alpha_x, \beta_x, \alpha_p\left(\alpha_x, \beta_x\right), \beta_p\left(\alpha_x, \beta_x\right), d\right)$ is not suitable for SAs based on LEM1 predictions. The dependencies written as $\alpha_p\left(\alpha_x, \beta_x\right)$ and $\beta_p\left(\alpha_x, \beta_x\right)$ need to be omitted. With the available tabulated LEM1 data this can be done in three different ways: $RBE\left(\alpha_x, \beta_x, d\right)$ discussed in section 11.1, $RBE\left(\alpha_p, \beta_p, d\right)$ discussed in section 11.2 and $RBE\left(\alpha_x, \beta_x, \alpha_p, \beta_p, d\right)$ discussed in section 11.3. In addition, these steps mean that any further parameter used by the LEM is set constant to the value used for the creation of the database and is not affected by uncertainties. The effect of uncertainties in a subset of the LEM parameters are discussed by Friedrich *et al.* [9].

The LEM1 is currently used for patient treatment planning [30], therefore the partial SAs are already of great use. Although they do not represent comprehensive SAs, they provide a first insight to the size of uncertainties caused by the biological modeling process. The partial SAs for the LEM1 based treatments are compared to the corresponding partial SA for treatment plans based on RMF model predictions.

11.1. Partial SA: $RBE\left(\alpha_x, \beta_x, d\right)$

In this partial SA approach the general $RBE\left(\alpha_x, \beta_x, \alpha_p\left(\alpha_x, \beta_x\right), \beta_p\left(\alpha_x, \beta_x\right), d\right)$ is reduced to $RBE\left(\alpha_x, \beta_x, d\right)$. This means, the conditions $\alpha_p\left(\alpha_x, \beta_x\right) = const$ and $\beta_p\left(\alpha_x, \beta_x\right) = const$ are applied.

Axial slices of the 3-D maps of the partial SA result are shown in figure 11.1 for RMF model based treatment plans and in figure 11.2 for LEM1 based treatment plans. Three cell lines are evaluated. Their α_x/β_x ratios are marked above the first row in the figures. The small $\alpha_x/\beta_x = 2$ Gy ($\alpha_x = 0.1$ Gy^{-1} and $\beta_x = 0.05$ Gy^{-2}) is commonly used for chordoma of the scull base [30]. The intermediate $\alpha_x/\beta_x = 5.1$ Gy ($\alpha_x = 0.313$ Gy^{-1} and $\beta_x = 0.0615$ Gy^{-2}) is obtained for human submandibular gland (HSG) cells [41]. The

---

[*] *http://totlxl.to.infn.it/lem*

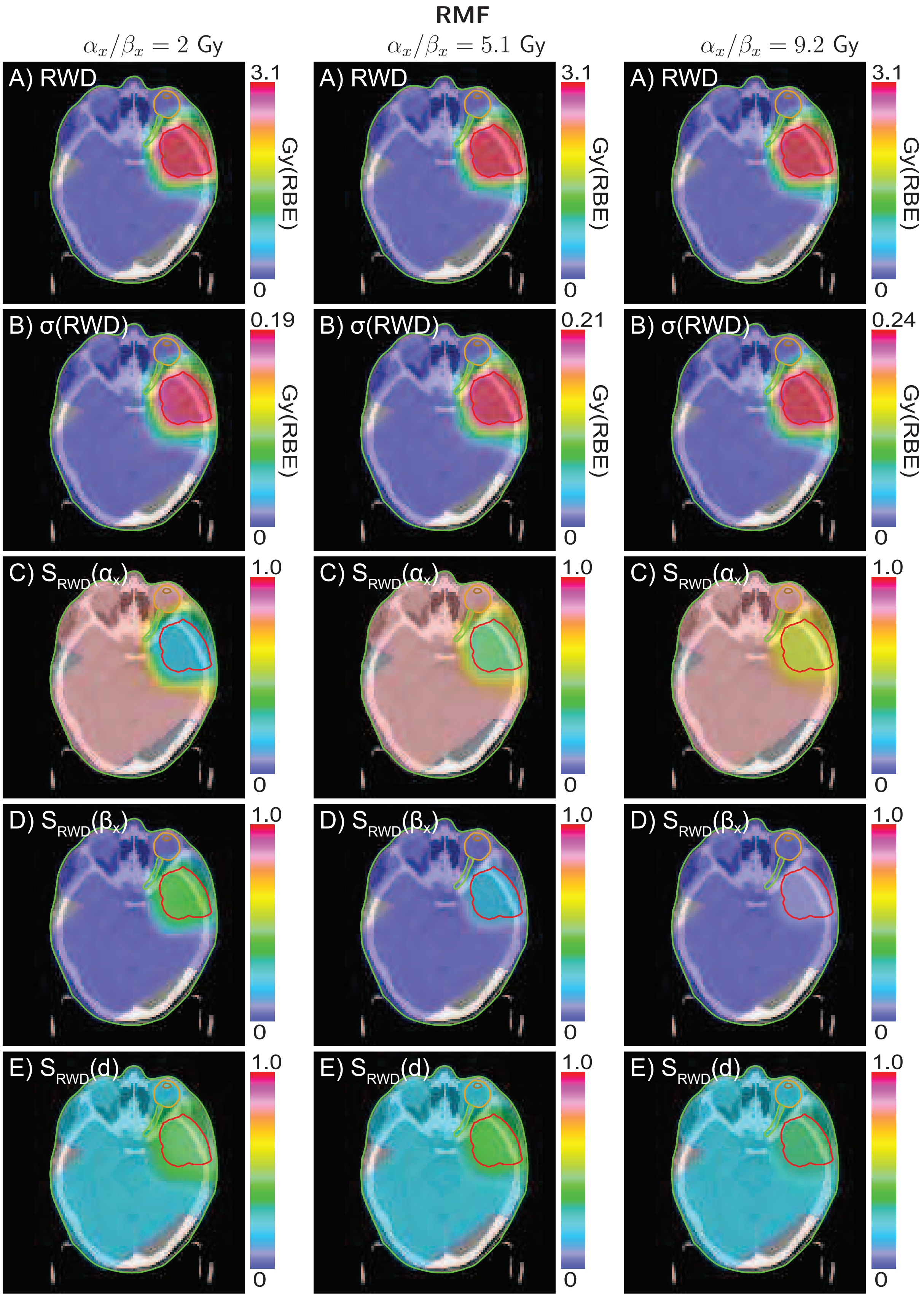

Figure 11.1.: Partial SA result for RMF model based treatment plans, uncertainties in α_x, β_x and d and three different α_x/β_x ratios. The panels show the optimized RWD (panels A) together with its uncertainty (panels B). Panels C-E show the sensitivity maps.

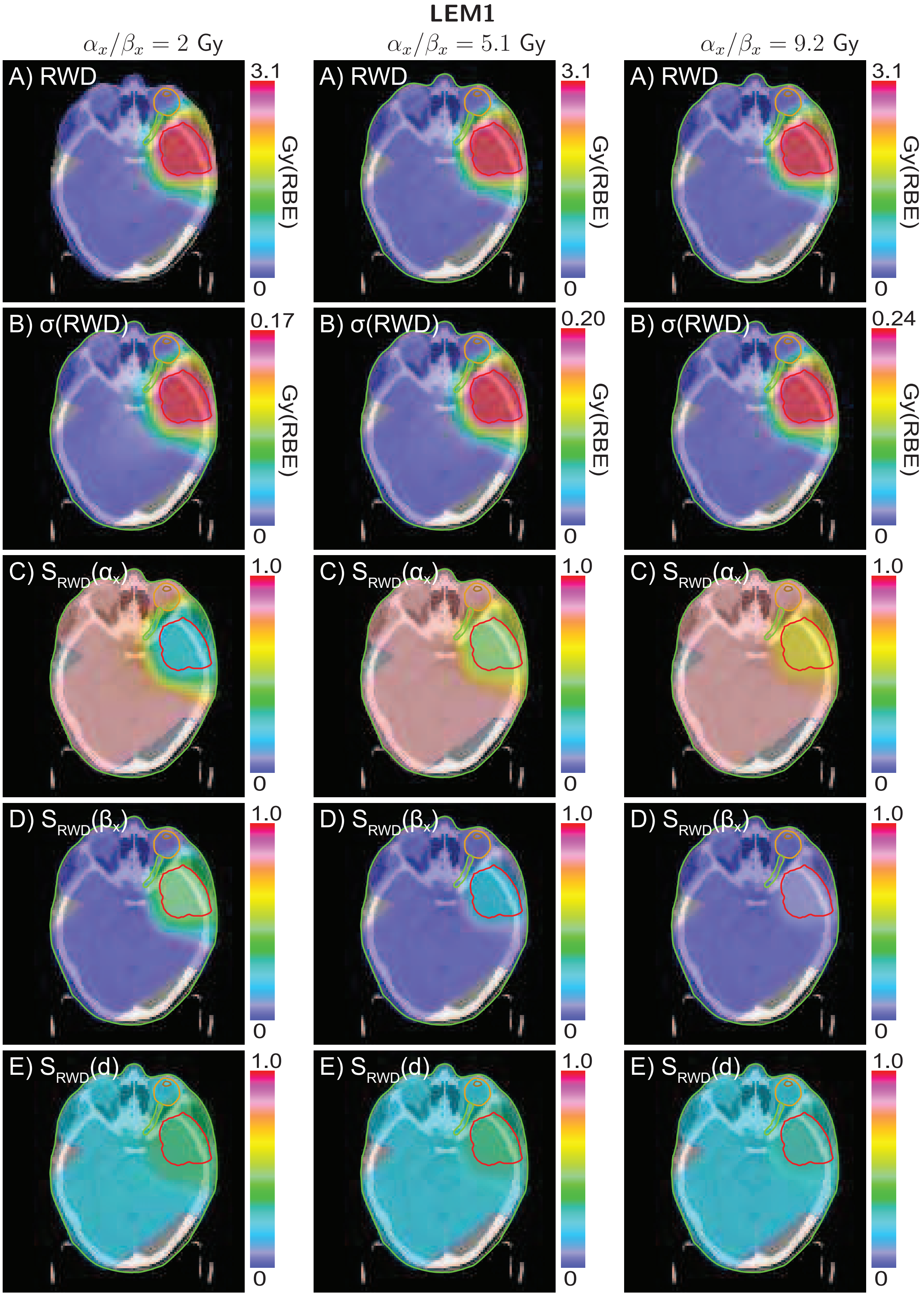

Figure 11.2.: Partial SA result for LEM1 based treatment plans, uncertainties in α_x, β_x and d and three different α_x/β_x ratios. The panels show the optimized RWD (panels A) together with its uncertainty (panels B). Panels C-E show the sensitivity maps.

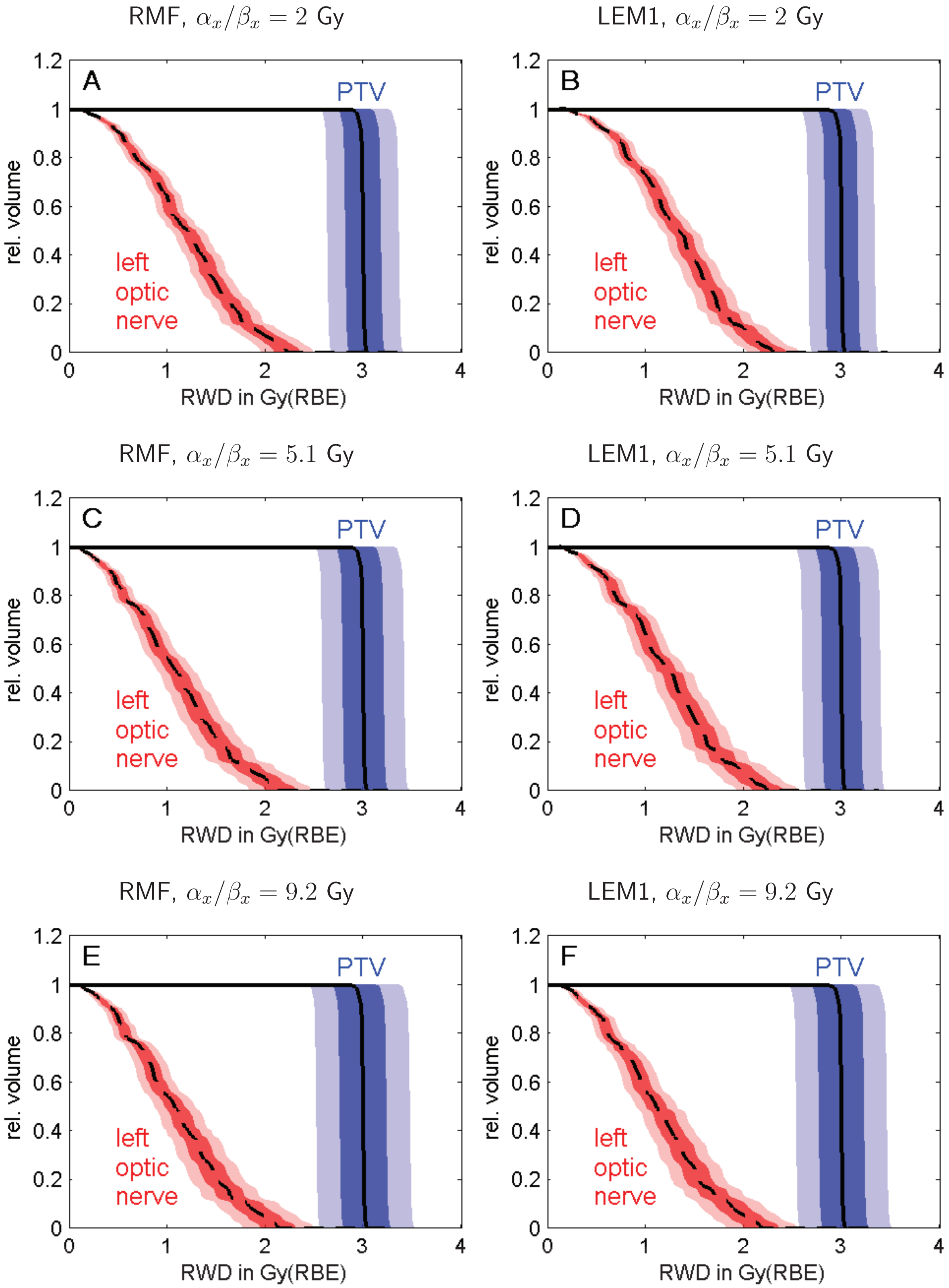

Figure 11.3.: This figure shows the probability RWDVHs for the partial SA applied to both RMF model and LEM1 based treatment plans and a range of α_x/β_x. The partial SA is based on the assumption that $RBE\,(\alpha_x, \beta_x, d)$. The unchanged optimization result is displayed in solid black for the planning target volume (PTV) and in dashed black for the left optical nerve. The uncertainties in the RWDVHs are indicated as $\pm\sigma$ (68.3% lie inside the dark area) and $\pm 2\sigma$ (95.4% lie inside the combination of light and dark area).

third cell line has the greatest $\alpha_x/\beta_x = 9.2$ Gy ($\alpha_x = 0.184$ Gy^{-1}, $\beta_x = 0.02$ Gy^{-2}). These values were obtained for Chinese hamster fibroblast, V79 [41]. The default input parameter uncertainties are used: $\sigma(\alpha_x) = 10\%$, $\sigma(\beta_x) = 10\%$ and $\sigma(d) = 5\%$.

The rows of figure 11.1 and figure 11.2 show the optimized RWDs (panels A) together with their resulting uncertainties (panels B). The sensitivity maps are displayed in panels C-E. Several structures are marked in the plots: the planning target volume (PTV) in red, the left optical nerve (green) as well as the left eyeball (orange) and the left lens (brown).

The optimization results of the six considered optimizations are comparable (panels A in the figures). In the corresponding uncertainties (panels B) two trends are observed. The uncertainty increases with increasing α_x/β_x and the uncertainty is in general slightly higher for the RMF model.

The partial SA for both models are very similar. $S_{RWD}(\alpha_x)$ (panels C) shows the highest values. The only exception is the region of the PTV in case of the small $\alpha_x/\beta_x = 2$ Gy. In this case $S_{RWD}(\alpha_x) \leq 0.2$. $S_{RWD}(\beta_x)$ (panels D) is only high inside the PTV, where $S_{RWD}(\alpha_x)$ decreases at the same time. This is more pronounced for small α_x/β_x than for large α_x/β_x. The uncertainty in d (panels E) has a sensitivity value $S_{RWD}(\alpha_x) \approx 0.2$, only in the PTV it increases to $S_{RWD}(\alpha_x) \approx 0.4$.

The sensitivity maps (panels C-E) can be explained with the calculation of the RWD (cf. equations (2.5) and (7.12)).

$$RWD = RBE(\alpha_x, \beta_x, d) \cdot d = 0.5\left(-\alpha_x/\beta_x + \sqrt{(\alpha_x/\beta_x)^2 + 4d(\alpha_p + \beta_p d)/\beta_x}\right) \tag{11.1}$$

The dose d is high in the PTV as the tumor is located there. The second term in the square root $(4d(\alpha_p + \beta_p d)/\beta_x)$ is relatively large, hence all three input uncertainties contribute to the uncertainty in the result.

The dose d is small in the regions where $S_{RWD}(\alpha_p)$ dominates. Small d allows to expand the square root in equation (11.1) with a Taylor series.

$$\begin{aligned}
RWD &= 0.5\left(-\alpha_x/\beta_x + \sqrt{(\alpha_x/\beta_x)^2 + 4d(\alpha_p + \beta_p d)/\beta_x}\right) && (11.2)\\
&= 0.5(\alpha_x/\beta_x) \cdot \left(-1 + \sqrt{1 + \frac{4d\beta_x(\alpha_p + \beta_p d)}{\alpha_x^2}}\right) && (11.3)\\
&\approx 0.5(\alpha_x/\beta_x) \cdot \left(-1 + 1 + 0.5\frac{4d\beta_x(\alpha_p + \beta_p d)}{\alpha_x^2}\right) && (11.4)\\
&= \frac{d(\alpha_p + \beta_p d)}{\alpha_x} && (11.5)
\end{aligned}$$

The requirement for this Taylor expansion $\sqrt{1+x} \approx 1 + 0.5x$ is that $|x| \leq 1$ [53]. In the Taylor expansion done here, $x = 4d\beta_x(\alpha_p + \beta_p d)/\alpha_x^2$. This shows that the β_x terms are canceled out for small d. The parameters α_x and d remain along with their uncertainties. For the shown examples, this is true in regions where $d \leq 0.25$ Gy. This region is identical to the region where $S_{RWD}(\alpha_p) \geq 0.75$. $S_{RWD}(\alpha_p) > S_{RWD}(d)$ in the regions with small d, due to the fact that the assigned uncertainties are different ($\sigma(\alpha_p) = 10\%$ and $\sigma(d) = 5\%$).

The small differences in the PTV region between the LEM1 and RMF model based partial SA can be explained with equation (11.1) and the general behavior of α_p and β_p. For the RMF model, both α_p and β_p increase with increasing LET (cf. figure 7.1, page 42), whereas for the LEM1, only α_p increases with LET and β_p decreases (cf. figure B.1, in Appendix B). The part $4d\left(\alpha_p + \beta_p d\right)/\beta_x$ of equation (11.1) shows, why a larger β_p results in a larger sensitivity value of d and β_x. This effect is the greatest for $\alpha_x/\beta_x = 2$ Gy.

Figure 11.3 shows the corresponding probability RWDVHs for the partial SA discussed, based on figures 11.1 and 11.2. In this partial SA, the RMF model based treatment plans have a slightly higher uncertainty in the RWDVHs. All displayed combinations show significant uncertainties in the RWDVHs. A consideration of uncertainties in the biological modeling of carbon ion therapy is necessary, independent of the applied α_x/β_x or the used biological model.

11.2. Partial SA: $RBE\left(\alpha_p, \beta_p, d\right)$

In this partial SA approach the general $RBE\left(\alpha_x, \beta_x, \alpha_p\left(\alpha_x, \beta_x\right), \beta_p\left(\alpha_x, \beta_x\right), d\right)$ is reduced to $RBE\left(\alpha_p, \beta_p, d\right)$. This means, the conditions $\alpha_x = const$, $\beta_x = const$ together with $\partial\alpha_p/\partial\alpha_x = \partial\alpha_p/\partial\beta_x = 0$ and $\partial\beta_p/\partial\alpha_x = \partial\beta_p/\partial\beta_x = 0$ are applied. This evaluation is very similar to the one presented in the previous section. The same three α_x/β_x values are evaluated for both the RMF model and the LEM1. The default uncertainties are assigned to the input parameters: $\sigma\left(\alpha_p\right) = 10\%$, $\sigma\left(\beta_p\right) = 10\%$ and $\sigma\left(d\right) = 5\%$.

In Appendix D.1 axial slices of the 3-D SA for the three α_x/β_x values and the two biological models are shown. Based on these figures a similar discussion as in the previous section is done (Appendix D.1).

Figure 11.4 shows the probability RWDVHs for the three α_x/β_x values and the two biological models. The higher the α_x/β_x value is, the larger are the resulting uncertainties. The LEM1 based treatment plans have a slightly higher uncertainty than the corresponding RMF model based plans. Compared to figure 11.3, figure 11.4 shows larger uncertainties in all six panels. Note, that this does not directly mean that the uncertainties in α_p and β_p are more crucial than the uncertainties in α_x and β_x. The biological modeling for both the RMF model and the LEM1, predict α_p and β_p as functions of α_x and β_x. This was omitted here, but needs to be considered for a comprehensive SA. Nevertheless, this partial SA provides important information: all displayed combinations show significant uncertainties in the RWDVHs. Hence, also this partial SA shows that a consideration of uncertainties in the biological modeling of carbon ion therapy is necessary, independent of the applied α_x/β_x or the used biological model.

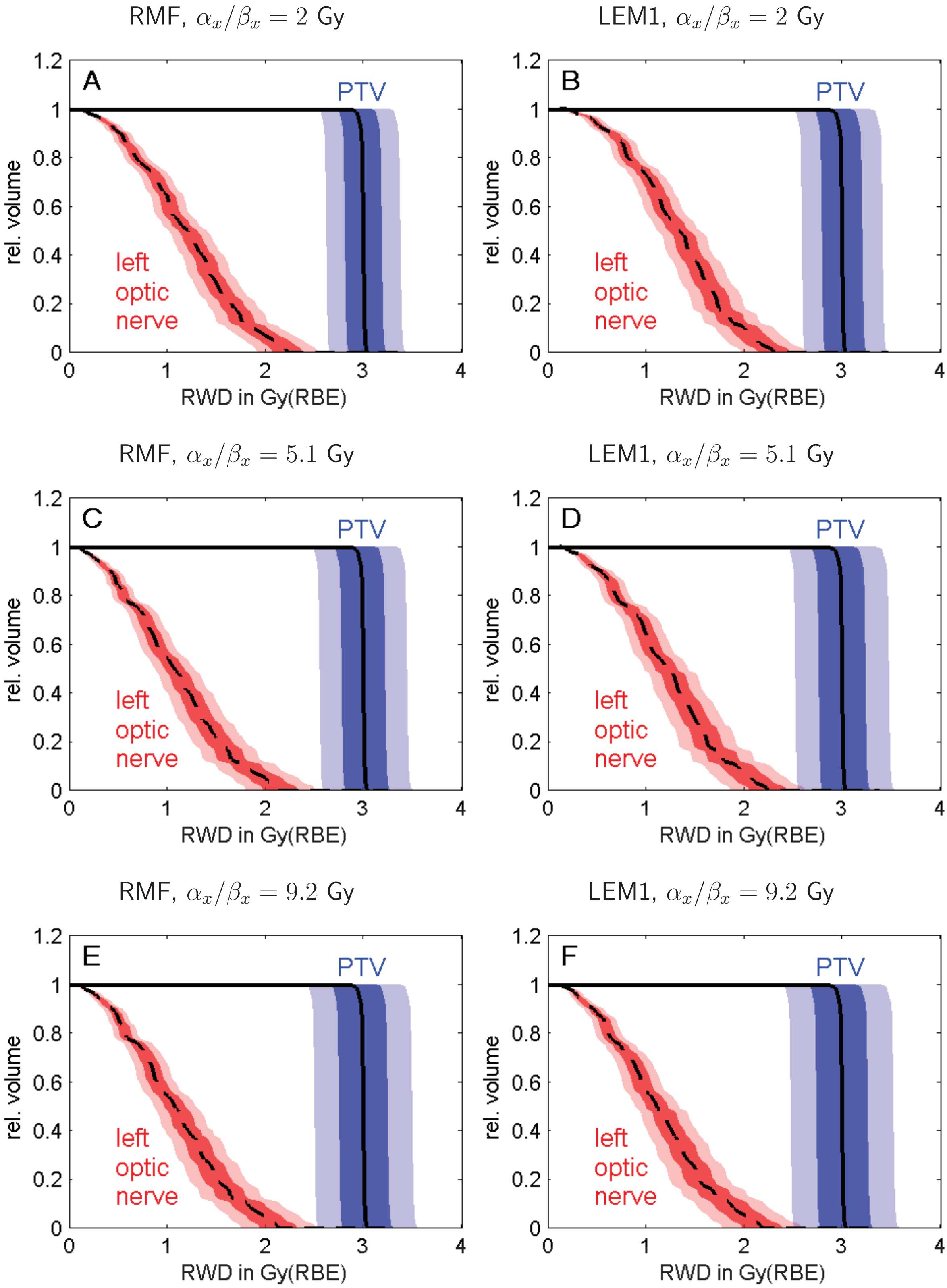

Figure 11.4.: This figure shows the probability RWDVHs for the partial SA applied to both RMF model and LEM1 based treatment plans and a range of α_x/β_x. The partial SA is based on the assumption that $RBE\,(\alpha_p, \beta_p, d)$. The unchanged optimization result is displayed in solid black for the planning target volume (PTV) and in dashed black for the left optical nerve. The uncertainties in the RWDVHs are indicated as $\pm\sigma$ (68.3% lie inside the dark area) and $\pm 2\sigma$ (95.4% lie inside the combination of light and dark area).

11.3. Partial SA: $RBE\left(\alpha_x, \beta_x, \alpha_p, \beta_p, d\right)$

In this partial SA approach the general $RBE\left(\alpha_x, \beta_x, \alpha_p\left(\alpha_x, \beta_x\right), \beta_p\left(\alpha_x, \beta_x\right), d\right)$ is reduced to $RBE\left(\alpha_x, \beta_x, \alpha_p, \beta_p, d\right)$. This means the conditions $\partial\alpha_p/\partial\alpha_x = \partial\alpha_p/\partial\beta_x = 0$ and $\partial\beta_p/\partial\alpha_x = \partial\beta_p/\partial\beta_x = 0$ are applied. Note, that this does not reflect biological modeling as it is done by the RMF model or the by LEM1. The biological model is executed once to obtain a set of α_p and β_p. To perform the SA, independent uncertainties are assigned to α_x, β_x, α_p, β_p and d. The simulated changes in α_p and β_p do not depend on changes in α_x and β_x. Nevertheless this partial SA is presented in this thesis to demonstrate the necessity to include $\alpha_p\left(\alpha_x, \beta_x\right)$ and $\beta_p\left(\alpha_x, \beta_x\right)$ into a comprehensive SA for the biological modeling of carbon ion therapy. This is done by comparing the partial SA presented here with the comprehensive SA presented in section 10.2 on page 71.

The default uncertainties are assigned to the five input parameters: $\sigma\left(\alpha_x\right) = 10\%$, $\sigma\left(\beta_x\right) = 10\%$, $\sigma\left(\alpha_p\right) = 10\%$, $\sigma\left(\beta_p\right) = 10\%$ and $\sigma\left(d\right) = 5\%$. Figure 11.5 shows the result for $\alpha_x/\beta_x = 2$ Gy modeled with the RMF model. The partial SA results for $\alpha_x/\beta_x = 9.2$ Gy are shown in Appendix D.2. The small $\alpha_x/\beta_x = 2$ Gy ($\alpha_x = 0.1$ Gy^{-1} and $\beta_x = 0.05$ Gy^{-2}) is commonly used for chordoma of the scull base [30]. The second, larger $\alpha_x/\beta_x = 9.2$ Gy ($\alpha_x = 0.184$ Gy^{-1}, $\beta_x = 0.02$ Gy^{-2}) is obtained for Chinese hamster fibroblast, V79 [41].

Panel A of figure 11.5 shows the standard deviation of the RWD distribution. The RWD itself did not change for this partial SA and is equivalent to panel A in figure 10.2 on page 72. Panels B-F in figure 11.5 show the five corresponding sensitivity maps. The planning target volume (PTV) is marked in red, the left optical nerve in green together with the left eyeball (orange) and the left lens (brown).

$S_{RWD}\left(\alpha_x\right) \approx 0.45$ outside the PTV and declines $S_{RWD}\left(\alpha_x\right) < 0.1$ inside the PTV (panel B). $S_{RWD}\left(\alpha_p\right) \approx 0.40$ throughout the whole patient (panel D). $S_{RWD}\left(\beta_x\right)$ and $S_{RWD}\left(\alpha_p\right)$ are very low outside the PTV and reach values up to $S_{RWD}\left(\beta_x\right) \approx 0.24$ and $S_{RWD}\left(\beta_p\right) \approx 0.05$ in the PTV (panels C and E respectively). $S_{RWD}\left(d\right)$ ranges from 0.10 outside the PTV to 0.26 in the PTV (panel F). The results for the corresponding partial SA based on LEM1 predictions are very similar and not shown here.

The comparison with the comprehensive SA for the RMF model (figure 10.2 on page 72) demonstrates the drawbacks of the partial SA. The spatial changes of the S_{RWD} values are not reproduced. This is especially crucial for changes distal to the PTV, which depend on the LET and are caused by the high LET values occurring there (cf. section 10.1 on page 69 and section 10.2 on page 71). This region is of special interest, as OARs (organs at risk) are potentially located there (for example the left optical nerve in the discussed treatment scenario).

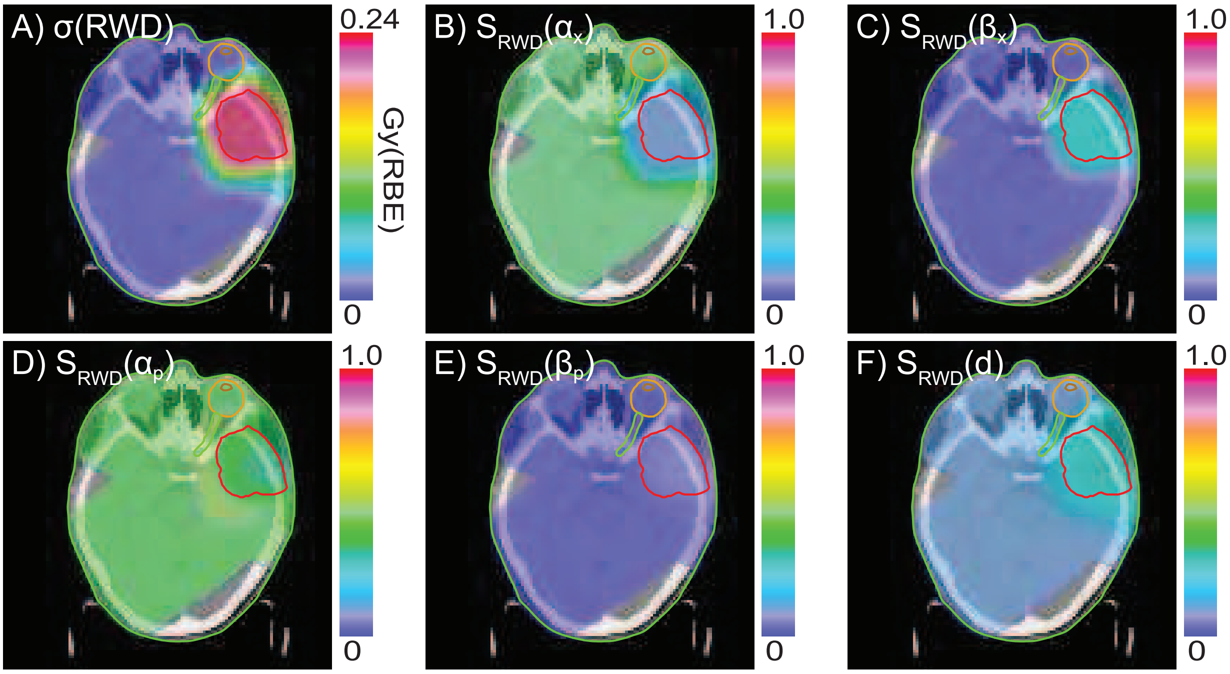

Figure 11.5.: Result of the partial SA for a treatment plan based on the RMF model with $\alpha_x/\beta_x = 2$ Gy. Panel A shows the uncertainty in the RWD distribution, panels B-F the sensitivity maps for the partial SA of $RBE\left(\alpha_x, \beta_x, \alpha_p, \beta_p, d\right)$. The dependencies of α_p and β_p on α_x and β_x are omitted. The assigned uncertainties of the input parameter are: $\sigma\left(\alpha_x\right) = 10\%$, $\sigma\left(\beta_x\right) = 10\%$, $\sigma\left(\alpha_p\right) = 10\%$, $\sigma\left(\beta_p\right) = 10\%$ and $\sigma\left(d\right) = 5\%$. The planning target volume (PTV) is marked in red, the left optical nerve in green together with the left eyeball (orange) and the left lens (brown).

12. Uncertainties in Tumor Control Probability (TCP) Calculation

In this chapter a comprehensive SA of the tumor control probability (TCP) is analyzed. In the framework of the RMF model, TCP can be expressed as a function of the biological modeling parameters c_1 and c_2 instead of α_p and β_p. Equation (12.1) is derived from $TCP\left(\alpha_x, \beta_x, d, \alpha_p, \beta_p\right)$ (cf. equation (7.29) on page 43) combined with $\alpha_p = \alpha_x c_1 + \beta_x c_2$ and $\beta_p = \beta_x c_1^2$ (cf. equations (7.5) and (7.6) on page 38).

$$\begin{aligned} &TCP\left(\alpha_x, \beta_x, d, c_1, c_2\right) = \\ &\qquad exp\left[-\sum_{i \in PTV} \rho_c \nu_i \cdot exp\left(-\left(\alpha_{x,i} c_{1,i} + \beta_{x,i} c_{2,i}\right) d_i N - \beta_{x,i} c_{1,i}^2 d_i^2 N\right)\right] \end{aligned} \tag{12.1}$$

In the following section a comprehensive SA is presented for TCP (section 12.1). A total sensitivity analysis result along with its composition out of higher order sensitivities is discussed in section 12.2.

12.1. Comprehensive SA of TCP

The results of the comprehensive SA for two representative cell lines are presented by the scatterplots in figure 12.1. The first cell line has a small $\alpha_x/\beta_x = 2$ Gy ($\alpha_x = 0.1$ Gy^{-1} and $\beta_x = 0.05$ Gy^{-2}) as used for chordoma of the skull base [30]). The comprehensive SA for this cell line is shown in panel A. In addition panel B displays a similar comprehensive SA for the larger $\alpha_x/\beta_x = 9.2$ Gy ($\alpha_x = 0.184$ Gy^{-1}, $\beta_x = 0.02$ Gy^{-2}). These values are used for Chinese hamster fibroblast, V79 [41]. The needed number of fractions was set to $N = 32$ for both α_x/β_x ratios.

The default uncertainties are assigned to the five input parameters: $\sigma\left(\alpha_x\right) = 10\%$, $\sigma\left(\beta_x\right) = 10\%$ $\sigma\left(d\right) = 5\%$, $\sigma\left(c_1\right) = 10\%$ and $\sigma\left(c_2\right) = 10\%$. In figure 12.1 these uncertainty distributions are displayed in five histograms (second row in both panels). Here the relative uncertainties (e.g. $1 + \Delta\alpha_x$) are displayed. Absolute values are not suitable for the visualization because the same random numbers are applied in every voxel and the input parameters change spatially. The calculation of TCP combines all voxel in the PTV to a single value (equation (12.1)). The changed values in every voxel i for one run n_r of the SA are derived by multiplications (cf. equations (12.2) to (12.6)).

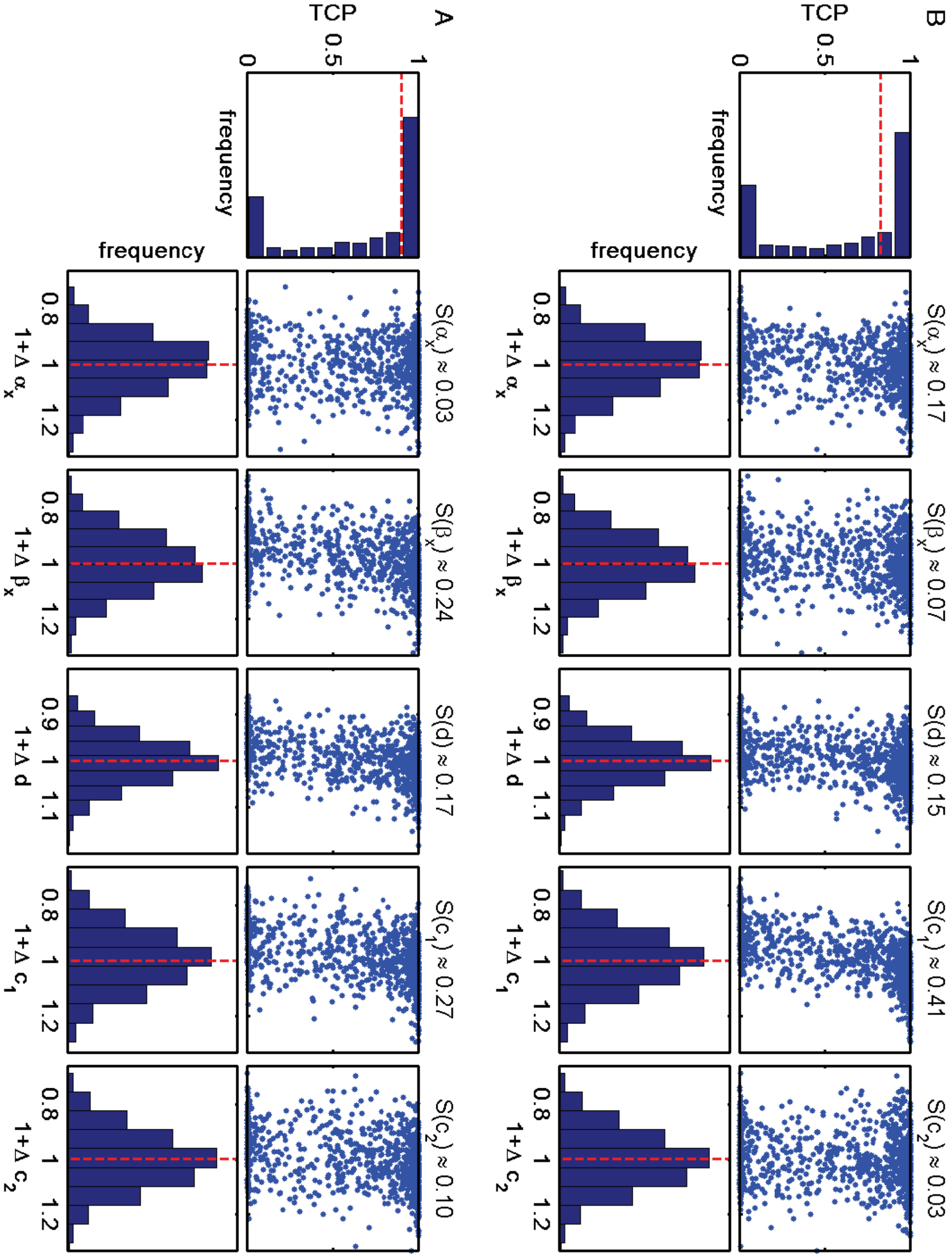

Figure 12.1.: This figure shows scatterplot representations of two SA results for the tumor control probability (TCP). Two α_x/β_x values are evaluated: $\alpha_x/\beta_x = 2$ Gy (panel A) and $\alpha_x/\beta_x = 9.2$ Gy (panel B). Comprehensive SAs are shown. This means that the $TCP(\alpha_x, \beta_x, d, c_1, c_2)$ is calculated based on RMF model predictions. The histograms show the relative uncertainties of the input parameters and the uncertainty in TCP. The red dashed lines indicate the initial unchanged values. To provide an optimal visualization the scatterplots display 10^3 out of $1.3 \cdot 10^5$ runs. Obtained sensitivity values S are shown above the respective scatterplots.

$$\alpha_{x,i}^{(n_r)} = \left(1 + \Delta\alpha_x^{(n_r)}\right)\alpha_{x,i} \tag{12.2}$$

$$\beta_{x,i}^{(n_r)} = \left(1 + \Delta\beta_x^{(n_r)}\right)\beta_{x,i} \tag{12.3}$$

$$d_i^{(n_r)} = \left(1 + \Delta d^{(n_r)}\right)d_i \tag{12.4}$$

$$c_{1,i}^{(n_r)} = \left(1 + \Delta c_1^{(n_r)}\right)c_{1,i} \tag{12.5}$$

$$c_{2,i}^{(n_r)} = \left(1 + \Delta c_2^{(n_r)}\right)c_{2,i} \tag{12.6}$$

Note, that the multiplication separates the spatial distribution in the voxel i from the changes in every run n_r. For instance the normal distribution indicated by $\sigma(\alpha_x) = 10\%$ is consequently assigned to $\Delta\alpha_x$. This is done accordingly for all other presented SAs (cf. chapter 9 on page 67). It is emphasized here, as the relative uncertainty distributions are necessary to display the SA result in the scatterplots.

Figure 12.1 shows large uncertainties in TCP. Both optimizations resulted initially in a TCP value above 80 % (red dashed line in the TCP histogram). The simulated values achieve every possible TCP value from $TCP = 0$ (tumor not controlled) to $TCP = 1$ (tumor controlled). As a consequence the measure TCP has to be interpreted cautiously when it is applied to carbon therapy.

The sensitivity values above the scatter plots in figure 12.1 show that the assigned uncertainties in the input parameters have different impacts for different α_x/β_x values. $S(c_1) \approx 0.27$ and $S(\beta_x) \approx 0.24$ have the highest values for $\alpha_x/\beta_x = 2$ Gy (panel A), whereas $S(c_1) \approx 0.41$ and $S(\alpha_x) \approx 0.17$ are the two main sensitivities for $\alpha_x/\beta_x = 9.2$ Gy (panel B). The impact of an uncertainty in the dose d is similar for both α_x/β_x.

The sensitivity values indicate the presence of correlation (cf. the discussion of scatterplots as a visualization tool for variance-based SA approaches in section 8.5.1 on page 57). This correlation is difficult to observe in the scatterplots of figure 12.1, as the resulting uncertainty of TCP cannot be described with a standard deviation. The largest sensitivity value is $S(c_2) \approx 0.41$ for $\alpha_x/\beta_x = 9.2$ Gy (panel B). This scatterplot shows the best visualization of the correlation: the higher c_1 is, the higher becomes the probability to achieve a high TCP value.

Summing $S(\alpha_x)+S(\beta_x)+S(d)+S(c_1)+S(c_2)$ results in 0.81 and 0.83 for $\alpha_x/\beta_x = 2$ Gy and $\alpha_x/\beta_x = 9.2$ Gy respectively. This means that there are nonzero higher order sensitivities in this analysis. They are discussed in the next section along with the total sensitivities TS.

Partial SAs, as analyzed for the LEM1 in chapter 11, were also adapted to TCP calculations. They showed similar large uncertainties in TCP ranging from $TCP = 0$ to $TCP = 1$ (data not shown). A comprehensive SA for other structure-based measures can be done accordingly. For example, the equivalent uniform dose (EUD) has been implemented as well. Variations in EUD are also large (data not shown). The computational time for a comprehensive SA of EUD is similar to the computation of the SAs of the $\mathrm{RWDVH}_{\mathrm{Vol}}$ which takes few hours. A comprehensive SA of TCP is faster, because only the voxel located in the target need to be considered.

12.2. Total Sensitivity Analysis and Higher Order Sensitivity Values

In this section the total sensitivity analysis and its composition of higher order sensitivity values is discussed. Summing the first order sensitivity values shown in figure 12.1 results in $S(\alpha_x)+S(\beta_x)+S(d)+S(c_1)+S(c_2) = 0.81$ and 0.83 for $\alpha_x/\beta_x = 2$ Gy and $\alpha_x/\beta_x = 9.2$ Gy respectively. If this sum is below one, higher order sensitivity values are present and the total sensitivity $TS > S$ for all or a subset of the input parameters (cf. equations (8.9) and (8.11) and their discussion on page 55).

The analysis is demonstrated for the small $\alpha_x/\beta_x = 2$ Gy (cf. panel A of figure 12.1). Table 12.1 shows the complete sensitivity information. The sensitivity values were obtained in three different ways: by calculating all cross terms, by the Factor Prioritization (FP) approach and by the Factor Fixation (FF) approach. The five columns show the sensitivity values for the five input parameters. The corresponding inputs are highlighted in bold in every column.

The cross terms in lines 2-16, as well as S and TS in lines 1a and 17a are calculated for $n = 1.05 \cdot 10^6$ by executing and sorting them gradually. The number of parts in which the sorted result is divided has the size $n_{par} = 8$. This means that for the fifth order term, there are 8^5 subdivisions each with 32 runs. The order of the sorting is indicated by the order in the sensitivity values. For instance $S(\boldsymbol{\beta_x}, d)$ is calculated by first sorting in β_x and then in d in the next step. The exact procedure has been introduced in section 8.4 on page 54. The total sensitivity values TS are calculated as sum over all possible combinations containing one input parameter (cf. equation (8.9) on page 55). This corresponds to a summation of one column (lines 1a and 2-16) in table 12.1. Note, that equation (8.10) holds for large enough n. The sorting, which is done in this SA, becomes independent of the order of the input parameters ("The result does not change if for example the sorting is done first along α_x and then in β_x or vice versa"). Hence, the cross terms that depend on the same set of input parameters result in the same value. The cross terms in table 12.1 are independent of the order within the input parameters. This holds for all combinations (for instance, in line 3: $S(\boldsymbol{\beta_x}, d) = S(\boldsymbol{d}, \beta_x)$ or in line 9: $S(\boldsymbol{\beta_x}, d, c_1) = S(\boldsymbol{d}, \beta_x, c_1) = S(\boldsymbol{c_1}, \beta_x, d)$). Although all cross terms in table 12.1 are smaller than 0.03, they result in substantially greater TS than S values.

The results for both the Factor Prioritization (FP, cf. section 8.3 on page 51) and the Factor Fixation (FF, cf. section 8.4 on page 54) are based on $n = 1.3 \cdot 10^5$ runs. The FP approach calculates the first order sensitivities (S_{FP}), whereas the FF approach is a fast approximation to calculate S_{FF} and TS_{FF}.

Table 12.1 facilitates to compare the first order sensitivity values S and S_{FP} with the approximation S_{FF}. All three values agree well for the five input parameters (lines 1a-1c in table 12.1). Note, that S and S_{FP} are calculated in exactly the same way. The values are not equal as the number of runs is different. Due to the needed statistic for all cross terms, S is calculated based on $n = 1.05 \cdot 10^6$ whereas S_{FP} only on $n = 1.3 \cdot 10^5$. The small deviation is not caused by the seed of the random numbers. Executing the same SA a second time, with a different seed of random numbers but same n, has the same result.

The two calculations of the total sensitivity values in lines 17a and 17b of table 12.1 have relatively high differences (up to 18 %). The approximation of TS_{FF} (line 17b) is greater than the actual sum over the cross terms TS (line 17a). The main question for the total sensitivity analysis is how reliable all the small cross terms can be calculated or

	first order				
1a	$S\left(\boldsymbol{\alpha_x}\right) = 0.028$	$S\left(\boldsymbol{\beta_x}\right) = 0.231$	$S\left(\boldsymbol{d}\right) = 0.159$	$S\left(\boldsymbol{c_1}\right) = 0.253$	$S\left(\boldsymbol{c_2}\right) = 0.095$
1b	$S_{FP}\left(\boldsymbol{\alpha_x}\right) = 0.031$	$S_{FP}\left(\boldsymbol{\beta_x}\right) = 0.245$	$S_{FP}\left(\boldsymbol{d}\right) = 0.166$	$S_{FP}\left(\boldsymbol{c_1}\right) = 0.266$	$S_{FP}\left(\boldsymbol{c_2}\right) = 0.104$
1c	$S_{FF}\left(\boldsymbol{\alpha_x}\right) = 0.026$	$S_{FF}\left(\boldsymbol{\beta_x}\right) = 0.243$	$S_{FF}\left(\boldsymbol{d}\right) = 0.157$	$S_{FF}\left(\boldsymbol{c_1}\right) = 0.266$	$S_{FF}\left(\boldsymbol{c_2}\right) = 0.096$
	second order				
2	$S\left(\boldsymbol{\alpha_x}, \beta_x\right) = 0.002$	$S\left(\boldsymbol{\beta_x}, \alpha_x\right) = 0.002$	$S\left(\boldsymbol{d}, \alpha_x\right) = 0.001$	$S\left(\boldsymbol{c_1}, \alpha_x\right) = 0.002$	$S\left(\boldsymbol{c_2}, \alpha_x\right) = 0.001$
3	$S\left(\boldsymbol{\alpha_x}, d\right) = 0.002$	$S\left(\boldsymbol{\beta_x}, d\right) = 0.014$	$S\left(\boldsymbol{d}, \beta_x\right) = 0.014$	$S\left(\boldsymbol{c_1}, \beta_x\right) = 0.025$	$S\left(\boldsymbol{c_2}, \beta_x\right) = 0.006$
4	$S\left(\boldsymbol{\alpha_x}, c_1\right) = 0.002$	$S\left(\boldsymbol{\beta_x}, c_1\right) = 0.026$	$S\left(\boldsymbol{d}, c_1\right) = 0.015$	$S\left(\boldsymbol{c_1}, d\right) = 0.015$	$S\left(\boldsymbol{c_2}, d\right) = 0.005$
5	$S\left(\boldsymbol{\alpha_x}, c_2\right) = 0.001$	$S\left(\boldsymbol{\beta_x}, c_2\right) = 0.006$	$S\left(\boldsymbol{d}, c_2\right) = 0.005$	$S\left(\boldsymbol{c_1}, c_2\right) = 0.010$	$S\left(\boldsymbol{c_2}, c_1\right) = 0.010$
	third order				
6	$S\left(\boldsymbol{\alpha_x}, \beta_x, d\right) = 0.002$	$S\left(\boldsymbol{\beta_x}, \alpha_x, d\right) = 0.002$	$S\left(\boldsymbol{d}, \alpha_x, \beta_x\right) = 0.002$	$S\left(\boldsymbol{c_1}, \alpha_x, \beta_x\right) = 0.003$	$S\left(\boldsymbol{c_2}, \alpha_x, \beta_x\right) = 0.001$
7	$S\left(\boldsymbol{\alpha_x}, \beta_x, c_1\right) = 0.003$	$S\left(\boldsymbol{\beta_x}, \alpha_x, c_1\right) = 0.003$	$S\left(\boldsymbol{d}, \alpha_x, c_1\right) = 0.002$	$S\left(\boldsymbol{c_1}, \alpha_x, d\right) = 0.002$	$S\left(\boldsymbol{c_2}, \alpha_x, d\right) = 0.001$
8	$S\left(\boldsymbol{\alpha_x}, \beta_x, c_2\right) = 0.001$	$S\left(\boldsymbol{\beta_x}, \alpha_x, c_2\right) = 0.001$	$S\left(\boldsymbol{d}, \alpha_x, c_2\right) = 0.001$	$S\left(\boldsymbol{c_1}, \alpha_x, c_2\right) = 0.001$	$S\left(\boldsymbol{c_2}, \alpha_x, c_1\right) = 0.001$
9	$S\left(\boldsymbol{\alpha_x}, d, c_1\right) = 0.002$	$S\left(\boldsymbol{\beta_x}, d, c_1\right) = 0.021$	$S\left(\boldsymbol{d}, \beta_x, c_1\right) = 0.021$	$S\left(\boldsymbol{c_1}, \beta_x, d\right) = 0.021$	$S\left(\boldsymbol{c_2}, \beta_x, d\right) = 0.006$
10	$S\left(\boldsymbol{\alpha_x}, d, c_2\right) = 0.001$	$S\left(\boldsymbol{\beta_x}, d, c_2\right) = 0.006$	$S\left(\boldsymbol{d}, \beta_x, c_2\right) = 0.006$	$S\left(\boldsymbol{c_1}, \beta_x, c_2\right) = 0.012$	$S\left(\boldsymbol{c_2}, \beta_x, c_1\right) = 0.012$
11	$S\left(\boldsymbol{\alpha_x}, c_1, c_2\right) = 0.001$	$S\left(\boldsymbol{\beta_x}, c_1, c_2\right) = 0.012$	$S\left(\boldsymbol{d}, c_1, c_2\right) = 0.007$	$S\left(\boldsymbol{c_1}, d, c_2\right) = 0.007$	$S\left(\boldsymbol{c_2}, d, c_1\right) = 0.007$
	fourth order				
12	$S\left(\boldsymbol{\alpha_x}, \beta_x, d, c_1\right) = 0.003$	$S\left(\boldsymbol{\beta_x}, \alpha_x, d, c_1\right) = 0.003$	$S\left(\boldsymbol{d}, \alpha_x, \beta_x, c_1\right) = 0.003$	$S\left(\boldsymbol{c_1}, \alpha_x, \beta_x, d\right) = 0.003$	$S\left(\boldsymbol{c_2}, \alpha_x, \beta_x, d\right) = 0.001$
13	$S\left(\boldsymbol{\alpha_x}, \beta_x, d, c_2\right) = 0.001$	$S\left(\boldsymbol{\beta_x}, \alpha_x, d, c_2\right) = 0.001$	$S\left(\boldsymbol{d}, \alpha_x, \beta_x, c_2\right) = 0.001$	$S\left(\boldsymbol{c_1}, \alpha_x, \beta_x, c_2\right) = 0.001$	$S\left(\boldsymbol{c_2}, \alpha_x, \beta_x, c_1\right) = 0.001$
14	$S\left(\boldsymbol{\alpha_x}, \beta_x, c_1, c_2\right) = 0.001$	$S\left(\boldsymbol{\beta_x}, \alpha_x, c_1, c_2\right) = 0.001$	$S\left(\boldsymbol{d}, \alpha_x, c_1, c_2\right) = 0.001$	$S\left(\boldsymbol{c_1}, \alpha_x, d, c_2\right) = 0.001$	$S\left(\boldsymbol{c_2}, \alpha_x, d, c_1\right) = 0.001$
15	$S\left(\boldsymbol{\alpha_x}, d, c_1, c_2\right) = 0.001$	$S\left(\boldsymbol{\beta_x}, d, c_1, c_2\right) = 0.013$	$S\left(\boldsymbol{d}, \beta_x, c_1, c_2\right) = 0.013$	$S\left(\boldsymbol{c_1}, \beta_x, d, c_2\right) = 0.013$	$S\left(\boldsymbol{c_2}, \beta_x, d, c_2\right) = 0.013$
	fifth order				
16	$S\left(\boldsymbol{\alpha_x}, \beta_x, d, c_1, c_2\right) = 0.003$	$S\left(\boldsymbol{\beta_x}, \alpha_x, d, c_1, c_2\right) = 0.003$	$S\left(\boldsymbol{d}, \alpha_x, \beta_x, c_1, c_2\right) = 0.003$	$S\left(\boldsymbol{c_1}, \alpha_x, \beta_x, d, c_2\right) = 0.003$	$S\left(\boldsymbol{c_2}, \alpha_x, \beta_x, d, c_1\right) = 0.002$
	total sensitivity				
17a	$TS\left(\boldsymbol{\alpha_x}\right) = 0.055$	$TS\left(\boldsymbol{\beta_x}\right) = 0.346$	$TS\left(\boldsymbol{d}\right) = 0.255$	$TS\left(\boldsymbol{c_1}\right) = 0.374$	$TS\left(\boldsymbol{c_2}\right) = 0.163$
17b	$TS_{FF}\left(\boldsymbol{\alpha_x}\right) = 0.065$	$TS_{FF}\left(\boldsymbol{\beta_x}\right) = 0.384$	$TS_{FF}\left(\boldsymbol{d}\right) = 0.291$	$TS_{FF}\left(\boldsymbol{c_1}\right) = 0.411$	$TS_{FF}\left(\boldsymbol{c_2}\right) = 0.192$

Table 12.1.: This table summarizes the full (total) sensitivity analysis including all higher order sensitivities. $TCP(\alpha_x, \beta_x, d, c_1, c_2)$ is analyzed for $\alpha_x/\beta_x = 2$ Gy. The five columns show the values for the five input parameters. The corresponding input parameter is highlighted in bold in the columns. The results for both the Factor Prioritization (FP, line 1b) and the Factor Fixation (FF, lines 1c and 17b) are based on $n = 1.3 \cdot 10^5$ runs. The cross terms in lines 2-16, as well as S and TS in lines 1a and 17a, are calculated for $n = 1.05 \cdot 10^6$.

approximated. The reliability of both approaches increases with number of runs.

This comparison shows that the first order sensitivity values have good agreement, whereas the total sensitivity analysis and the resulting Factor Fixation approach defer noteworthy. A higher number of runs might result in better statistics and more reliable results. This is not feasible due to the increased computation time.

13. Sensitivity Analysis: Summary and Conclusion

In the previous chapters the variance-based sensitivity analysis (SA) methods were applied to the uncertainties in biological dose response models. The key results are summarized here. First general conclusions regarding the SA approaches and their implementation into carbon ion treatment planning are given. The second part is related to the SAs performed and evaluated within this thesis.

It was shown throughout the previous chapters that the variance-based SA can be adapted to carbon ion treatment planning. With the used formalisms it is possible to calculate $1.3 \cdot 10^5$ carbon ion treatment plans in few hours. This allows voxel-wise and structure-based SAs of real patient cases. Up to five independent input parameters were evaluated simultaneously, the extension to a sixth parameter or even more is straight forward.

The sensitivity analysis allows to prioritize the uncertainty in different input parameters (Factor Prioritization). The Factor Fixation approach, which allows to remove uninfluential input uncertainties, does not have sufficient statistics for a voxel-wise total SA. The calculation of structure-based measures requires less computation time. In this case it is possible to increase the number of runs and consequently to provide sufficient statistics for total sensitivity analyses. Due to computational limits a complete total SA, including all cross terms is applicable only for structure-based measures like the tumor control probability (TCP, chapter 12). Nevertheless the implemented SAs proved to be a powerful tool for the evaluation of biological uncertainties in dose response models for carbon ion therapy.

Comprehensive SAs were performed for relative biological effectiveness (RBE) predictions based on the repair-misrepair-fixation (RMF) model. This included uncertainties in the reference radiosensitivity parameters (α_x and β_x), the biological modeling process and the physical dose. Obtained uncertainties in the resulting RBE-weighted dose (RWD) turned out to be large. It was shown that the impact of different uncertainties on the RWD changes spatially throughout a patient (cf. chapter 10). This issue is crucial, as the impact of biological uncertainties differs for the tumor and organs at risk, depending on their location. The large uncertainties in the RWD result in a large spread in tumor control probability (cf. chapter 12).

The assumption of a precise physical dose delivery (without uncertainty) nevertheless resulted in a considerable uncertainty in the RWD due to the uncertainties in the biological modeling process (cf. section 10.3). This finding justifies the need to consider biological uncertainties, regardless of the achieved precision and accuracy in the physical dose delivery.

The partial sensitivity analyses for the first version of the local effect model (LEM1) and the repair-misrepair-fixation (RMF) model indicate that the evaluation of uncertainties in a subset of parameters only is not sufficient (cf. chapter 11). A comprehensive SA is needed, as it includes all dependencies ($\alpha_p(\alpha_x, \beta_x)$ and $\beta_p(\alpha_x, \beta_x)$) in the biological modeling process. Similar to the comprehensive SA, the partial SAs showed large variations in RWD. The spatial variations inside a patient are not reproduced by the partial SAs.

Variance-based sensitivity approaches were successfully implemented in carbon ion treatment planning. The resulting uncertainties of the RBE-weighted dose are considerable and need to be included into treatment planning and evaluation. The shown SAs facilitates the examination and comparison of the impacts of biological uncertainties in dose response models and hence further improve the accuracy and reliability of carbon ion radiotherapy.

Part V.

Summary and Conclusion

14. Summary

In this chapter the main parts and developments of this work are recapitulated. In order to evaluate the impact of uncertainties in biological dose response models a variance-based sensitivity analysis was developed and implemented into carbon ion therapy.

The implementation of three-dimensional carbon ion treatment planning was described in part II. The work was focused on the used biological models and their implementation. The repair-misrepair-fixation (RMF) model was successfully combined with carbon ion fragment spectra and validated within the scope of this thesis (cf. chapter 6 and reference [17]). The RMF model proved to be advantageous for fast biological modeling in carbon ion therapy.

Variance-based sensitivity methods were adapted to three-dimensional carbon ion treatment planning (chapter 8). These methods add error bars to a result and allow to examine the composition of its uncertainty originating from different input uncertainties (cf. reference [21]). The application of this sensitivity approach to treatment planning in carbon ion therapy leads to several important results:

- The uncertainties in biological parameters and the physical dose result in large uncertainties of the RBE-weighted dose RWD ("RWD = relative biological effectiveness (RBE) multiplied by physical dose") and hence in potential under- or overdosage (chapter 10). This bears the risk of lower tumor control probability or higher complication rates in normal tissue.

- Large uncertainties in the RWD persist even in case the uncertainty in the physical dose is removed (ideally precise planning and delivery of the physical dose). This proves that the consideration of biological uncertainties in carbon ion treatment planning is essential for the assessment of treatment outcome (section 10.3).

- Inclusion of the biological modeling process into the sensitivity analysis is necessary. Although partial sensitivity approaches, excluding parts of the biological modeling process, showed large uncertainties in the result similar to the comprehensive sensitivity analysis, the spatial distributions could not be reproduced with the partial sensitivity approaches (chapter 11).

- Uncertainties have a high impact on calculated tumor control probabilities (TCP) for carbon ion treatment plans (chapter 12). Absolute TCP values and the comparison of TCP need to be interpreted cautiously in carbon ion therapy.

The presented work provides powerful tools to evaluate the impact of uncertainties in biological dose response modeling for carbon ion therapy. Besides the possibility to add error bars to treatment plan evaluation, it assess which input uncertainties are the crucial factors for the resulting uncertainty of RWD. Now the possibility is given to evaluate the potential of uncertainty reductions due to further development in radiation biology. The presented methods can be used to enhance the accuracy of the biological modeling process and to increase robustness of carbon ion treatment plans, leading to increased reliability.

15. Conclusion

Throughout this thesis it was shown how to include uncertainties in biological dose response models into carbon ion therapy treatment planning and evaluation. This was done by a sensitivity analysis approach. Besides the uncertainty in the result of the treatment plan it provides the ranking of the impacts of uncertainties in different input parameters. Based on this sensitivity analysis, clear visualization tools were developed to examine biological uncertainties of carbon ion treatment planning. The introduced approach is suitable for comprehensive sensitivity analyses accounting for the main uncertainties in the biological dose response modeling for carbon ion therapy.

The results of performed sensitivity analyses show large uncertainties in the treatment plans. They are mainly caused by uncertainties in the biological modeling. This leads to the conclusion that precise physical dose application and planning is only half way to reliable carbon ion treatment planning. Carbon ion treatment planning must account for biological uncertainties in dose response modeling. The developed tools add the mentioned biological uncertainties to the treatment planning process and rank them by their impact. This ranking shows which uncertainty should be reduced to gain the most precision in a treatment plan.

The developed methods provide efficient tools to examine and compare the impacts of biological uncertainties in dose response models and hence further improve the accuracy and reliability of carbon ion radiotherapy. This approach is an important contribution to the general attempt to provide save and accurate patient treatment with carbon ion therapy.

Part VI.

Appendix

A. Hessians for the Optimization

In this chapter the calculations of the Hessian matrices for the optimization (cf. chapter 7) are given. In the implemented optimization Hessian matrices were approximated with the L-BFGS (limited memory-Broyden-Fletcher-Goldfarb-Shanno [44]) algorithm. The approximation is considerably faster than the exact calculation. The equations for the exact calculation of the Hessian matrices are listed for the sake of completeness.

A.1. Hessian of the Cost-Function

The Hessian matrix of the standard cost function can be written as [42]:

$$\begin{aligned}\frac{\partial^2 F}{\partial\omega_k\partial\omega_l} =& 2\sum_i \Bigg[p_i \left(\alpha_{p,il} d_{p,il} + 2\left(\sum_j \sqrt{\beta_{p,ij}} d_{p,ij}\cdot\omega_j \right) \cdot \sqrt{\beta_{p,il}} d_{p,il} \right) \\ & \cdot \left(\alpha_{p,ik} d_{p,ik} + 2\left(\sum_j \sqrt{\beta_{p,ij}} d_{p,ij}\cdot\omega_j \right) \cdot \sqrt{\beta_{p,ik}} d_{p,ik} \right) \\ & + 2p_i \left(\varepsilon_i\left(\omega\right) - \varepsilon_{i,pres} \right) \sqrt{\beta_{p,il}} d_{p,il} \cdot \sqrt{\beta_{p,ik}} d_{p,ik} \Bigg]. \end{aligned} \tag{A.1}$$

The used variables are introduced along with the calculation of the cost function F and its gradient $\partial F/\partial\omega_k$ in chapter 7. In this chapter, starting on page 37, the implementation of the optimization is described.

A.2. Hessian of the Objectives

Here the Hessian matrices of the implemented objectives are described. A total Hessian matrix as combination of the standard cost function (cf. equations (7.14) and (A.1)) and the objectives (cf. equations (A.2) and (A.3)) is a simple sum. The contribution of a voxel i to the calculation is only nonzero, if in this voxel the condition $\left(\varepsilon_i\left(\omega\right) - \varepsilon_{i,objMax}\right) \geq 0$ is fulfilled for the maximum objective or, correspondingly, $\left(\varepsilon_{i,objMin} - \varepsilon_i\left(\omega\right)\right) \geq 0$ is fulfilled for the minimum objective. These conditions can be implemented by assigning $p_{i,objMax} = 0$ or $p_{i,objMin} = 0$ in the needed voxel. The Hessian matrices for the objectives can be calculated:

$$\begin{aligned}\frac{\partial^2 F_{objMax}}{\partial\omega_k\partial\omega_l} =&2\sum_i \Bigg[p_{i,objMax}\left(\alpha_{p,il}d_{p,il}+2\left(\sum_j\sqrt{\beta_{p,ij}}d_{p,ij}\cdot\omega_j\right)\cdot\sqrt{\beta_{p,il}}d_{p,il}\right)\\ &\cdot\left(\alpha_{p,ik}d_{p,ik}+2\left(\sum_j\sqrt{\beta_{p,ij}}d_{p,ij}\cdot\omega_j\right)\cdot\sqrt{\beta_{p,ik}}d_{p,ik}\right)\\ &+2p_{i,objMax}\left(\varepsilon_i\left(\omega\right)-\varepsilon_{i,objMax}\right)\sqrt{\beta_{p,il}}d_{p,il}\cdot\sqrt{\beta_{p,ik}}d_{p,ik}\Bigg] \qquad \text{(A.2)}\end{aligned}$$

$$\begin{aligned}\frac{\partial^2 F_{objMin}}{\partial\omega_k\partial\omega_l} =&2\sum_i \Bigg[p_{i,objMin}\left(\alpha_{p,il}d_{p,il}+2\left(\sum_j\sqrt{\beta_{p,ij}}d_{p,ij}\cdot\omega_j\right)\cdot\sqrt{\beta_{p,il}}d_{p,il}\right)\\ &\cdot\left(\alpha_{p,ik}d_{p,ik}+2\left(\sum_j\sqrt{\beta_{p,ij}}d_{p,ij}\cdot\omega_j\right)\cdot\sqrt{\beta_{p,ik}}d_{p,ik}\right)\\ &+2p_{i,objMin}\left(\varepsilon_{i,objMin}-\varepsilon_i\left(\omega\right)\right)\sqrt{\beta_{p,il}}d_{p,il}\cdot\sqrt{\beta_{p,ik}}d_{p,ik}\Bigg]. \qquad \text{(A.3)}\end{aligned}$$

The used variables are introduced along with the calculation of the cost functions (F_{objMax} and F_{objMin}) and their gradients ($\partial F_{objMax}/\partial\omega_k$ and $\partial F_{objMin}/\partial\omega_k$) in chapter 7. In this chapter 7, starting on page 37, the implementation of the optimization is described.

A.3. Hessian of the Constraints

The Hessian matrix of the hard maximum and minimum constraints can be calculated as follows:

$$\frac{\partial^2 c_{i,conMax}}{\partial\omega_k\partial\omega_l} = 2\sqrt{\beta_{p,il}}d_{p,il}\cdot\sqrt{\beta_{p,ik}}d_{p,ik} \qquad \text{(A.4)}$$

$$\frac{\partial^2 c_{i,conMin}}{\partial\omega_k\partial\omega_l} = -2\sqrt{\beta_{p,il}}d_{p,il}\cdot\sqrt{\beta_{p,ik}}d_{p,ik}. \qquad \text{(A.5)}$$

The used variables are introduced in chapter 7, starting on page 37. The Hessian matrix of the mean RWD is:

$$\frac{\partial^2 ceq_{meanTar}}{\partial\omega_k\partial\omega_l} = \frac{1}{N_{tar}}\sum_{i\in tar}\left(2\sqrt{\beta_{p,il}}d_{p,il}\cdot\sqrt{\beta_{p,ik}}d_{p,ik}\right). \qquad \text{(A.6)}$$

The calculation and explanation of these hard maximum and minimum constraints and the constraint for the mean RWD in the target are presented in section 7.3 on page 39.

B. Example of a Treatment Plan Optimization Result for LEM1 Predictions

Figure B.1 shows a result of a treatment plan optimization. This astrocytoma patient was initially treated with photon radiotherapy at the Klinikum rechts der Isar in Munich and is used as the planning and evaluation example throughout this work. For figure B.1 constant values $\alpha_x = 0.1\,\mathrm{Gy}^{-1}$ and $\beta_x = 0.05\,\mathrm{Gy}^{-2}$ are set throughout the patient. The first version of the local effect model (LEM1) is used here. (A similar example using the repair-misrepair-fixation(RMF) model is shown in figure 7.1 on page 42.) The plan was optimized on RWD = 3 Gy(RBE) in the planning target volume (PTV) with two carbon beams. These eight panels show the used beam geometry and the calculated biological and physical quantities in color displayed on top of the patient CT. The optimization settings in terms of prescribed RWD, penalties and objectives are summarized in table 7.1 on page 41.

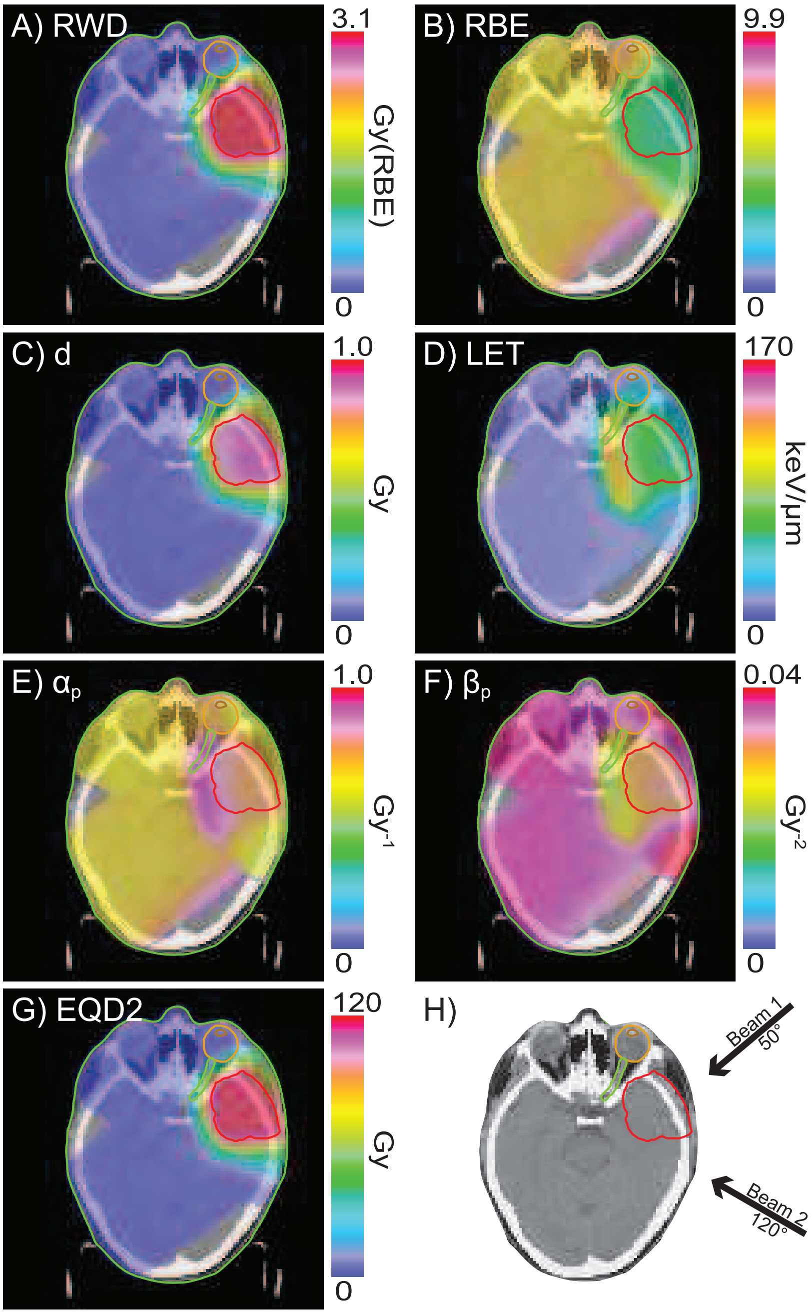

Figure B.1.: Example of an optimization result with the first version of the local effect model (LEM1) showing the optimized RWD (panel A) and the calculated RBE (panel B). Physical dose and dose-weighted LET are plotted in panels C and D. The radiosensitivity parameters α_p and β_p (panels E and F respectively) were obtained with the LEM1 and constant values $\alpha_x = 0.1\text{Gy}^{-1}$ and $\beta_x = 0.05\text{Gy}^{-2}$. Panel G shows the EQD2 calculated voxel by voxel. The used beam geometry for the astrocytoma patient can be found in panel H. The planning target volume (PTV) is marked in red, the left optical nerve in green together with the left eyeball (orange) and the left lens (brown).

C. Sensitivity Analysis, Example of the Interplay Effect of Changes in Two Parameters

Throughout the introduction to sensitivity analysis (cf. chapter 8) the terms “interplay” effect or “cross terms” are used frequently to describe the interaction of changes in two (or more) parameters. Here a short example is given, demonstrating how this term is derived and how it has to be interpreted. Considering a simple function

$$Y(X_1, X_2) = X_1 \cdot X_2 \tag{C.1}$$

evaluated at the point $X_1 = 10$ and $X_2 = 2$ and in addition with $+0.5$ deviation from X_1 and X_2:

$$Y(10.0, 2.0) = 20.00 \tag{C.2}$$
$$Y(10.5, 2.0) = 21.00 \tag{C.3}$$
$$Y(10.0, 2.5) = 25.00 \tag{C.4}$$
$$Y(10.5, 2.5) = 26.25. \tag{C.5}$$

The deviations in Y can be calculated following the simple approach in equation (8.1) and equation (8.3) on pages 49 and 50 respectively.

$$\Delta Y = Y(10.5, 2.5) - Y(10.0, 2.0) = 6.25 \tag{C.6}$$
$$\Delta_1 Y = Y(10.5, 2.0) - Y(10.0, 2.0) = 1 \tag{C.7}$$
$$\Delta_2 Y = Y(10.0, 2.5) - Y(10.0, 2.0) = 5 \tag{C.8}$$
$$\Delta_{12} Y = Y(10.5, 2.5) - Y(10.0, 2.0) - \Delta_1 Y - \Delta_2 Y = 0.25 \tag{C.9}$$

The $\Delta Y = 6.25$ total deviation in the result Y consists of $\Delta_1 Y = 1$ and $\Delta_2 Y = 5$ from X_1 and X_2 respectively and $\Delta_{12} Y = 0.25$ of their interplay. Because X_1 was changed, a change in X_2 has a greater impact and vice versa. Note, that $\Delta_{12} Y = 0$ follows if the two parameters are linked linearly. This is for example the case for $Y = X_1 \pm X_2$. This linear combination has the property $\partial^2 Y / \partial X_1 \partial X_2 = 0$, showing that there is no interplay between X_1 and X_2.

D. Partial SA

D.1. Partial SA: $RBE\left(\alpha_p, \beta_p, d\right)$, 3-D SA

In this section axial slices of the 3-D partial SA (cf. section 11.2, page 82) are presented. The performed partial SA assumes that the relative biological effectiveness is a function of only three input parameters: $RBE\left(\alpha_p, \beta_p, d\right)$.

Figure D.1 shows the results for RMF model based treatment plans and figure D.2 for LEM1 based treatment plans. The figures can be found on the next double page. Three cell lines are evaluated. Their α_x/β_x ratios are marked above the first row in the figures. The small $\alpha_x/\beta_x = 2$ Gy ($\alpha_x = 0.1$ Gy^{-1} and $\beta_x = 0.05$ Gy^{-2}) is commonly used for chordoma of the scull base [30]. The intermediate $\alpha_x/\beta_x = 5.1$ Gy ($\alpha_x = 0.313$ Gy^{-1} and $\beta_x = 0.0615$ Gy^{-2}) is obtained for human submandibular gland (HSG) cells [41]. The third cell line has the greatest $\alpha_x/\beta_x = 9.2$ Gy ($\alpha_x = 0.184$ Gy^{-1}, $\beta_x = 0.02$ Gy^{-2}). These values were obtained for Chinese hamster fibroblast, V79 [41]. The default input parameter uncertainties are used: $\sigma\left(\alpha_p\right) = 10\%$, $\sigma\left(\beta_p\right) = 10\%$ and $\sigma\left(d\right) = 5\%$.

The rows of figures D.1 and D.2 show the optimized RWDs (panels A) together with their resulting uncertainties (panels B). The sensitivity maps are displayed in panels C-E. Several structures are marked in the plots: the planning target volume (PTV) in red, the left optical nerve (green) as well as the left eyeball (orange) and the left lens (brown).

The optimization results of the six considered optimizations are comparable (panels A in the figures). In the corresponding uncertainties (panels B) two trends are observed. The uncertainty increases with increasing α_x/β_x and the uncertainty is in general slightly higher for the LEM1 based treatment plans. $S_{RWD}\left(\alpha_p\right)$ is the highest in the RMF model based SA in figure D.1. Its value decreases in the area of the PTV. The dose d has the second highest impact on the resulting uncertainty in the RWD. $S_{RWD}\left(d\right)$ is higher in the PTV. The trend of higher $S_{RWD}\left(d\right)$ and lower $S_{RWD}\left(\alpha_p\right)$ in the PTV is more pronounced the lower α_x/β_x. The sensitivity on the β_p is the smallest and only reaches values $S_{RWD}\left(\beta_p\right) > 0.05$ in the PTV.

The sensitivity values for the LEM1 based treatment plans, displayed in figure D.2, show constant $S_{RWD}\left(\alpha_p\right)$, $S_{RWD}\left(\beta_p\right)$ and $S_{RWD}\left(d\right)$. The sensitivity on α_p is the highest, followed by the sensitivity on d. $S_{RWD}\left(\beta_p\right) < 0.05$ throughout the patient.

For both models the mentioned trends in panels C-E can be explained with the calculation of $RWD = 0.5\left(-\alpha_x/\beta_x + \sqrt{\left(\alpha_x/\beta_x\right)^2 + 4d\left(\alpha_p + \beta_p d\right)/\beta_x}\right)$ (cf. equation (11.1)). The x-ray parameters are constant for this partial SA, this means that $d\left(\alpha_p + \beta_p d\right)$ is the crucial part for the RWD calculation in this partial SA.

Considering $d\left(\alpha_p + \beta_p d\right)$ explains the spatial distribution of $S_{RWD}\left(\alpha_p\right)$, $S_{RWD}\left(\beta_p\right)$ and $S_{RWD}\left(d\right)$. For both RMF model and LEM1 based treatment plans, the dose d is small outside the PTV. Only the term $\alpha_p \cdot d$ actually influences $d\left(\alpha_p + \beta_p d\right)$, resulting in a very small $S_{RWD}\left(\beta_p\right)$, but high $S_{RWD}\left(\alpha_p\right)$ and $S_{RWD}\left(d\right)$. $S_{RWD}\left(\alpha_p\right) > S_{RWD}\left(d\right)$ as the assigned uncertainties are different ($\sigma\left(\alpha_p\right) = 10\%$ and $\sigma\left(d\right) = 5\%$). In the case of RMF model

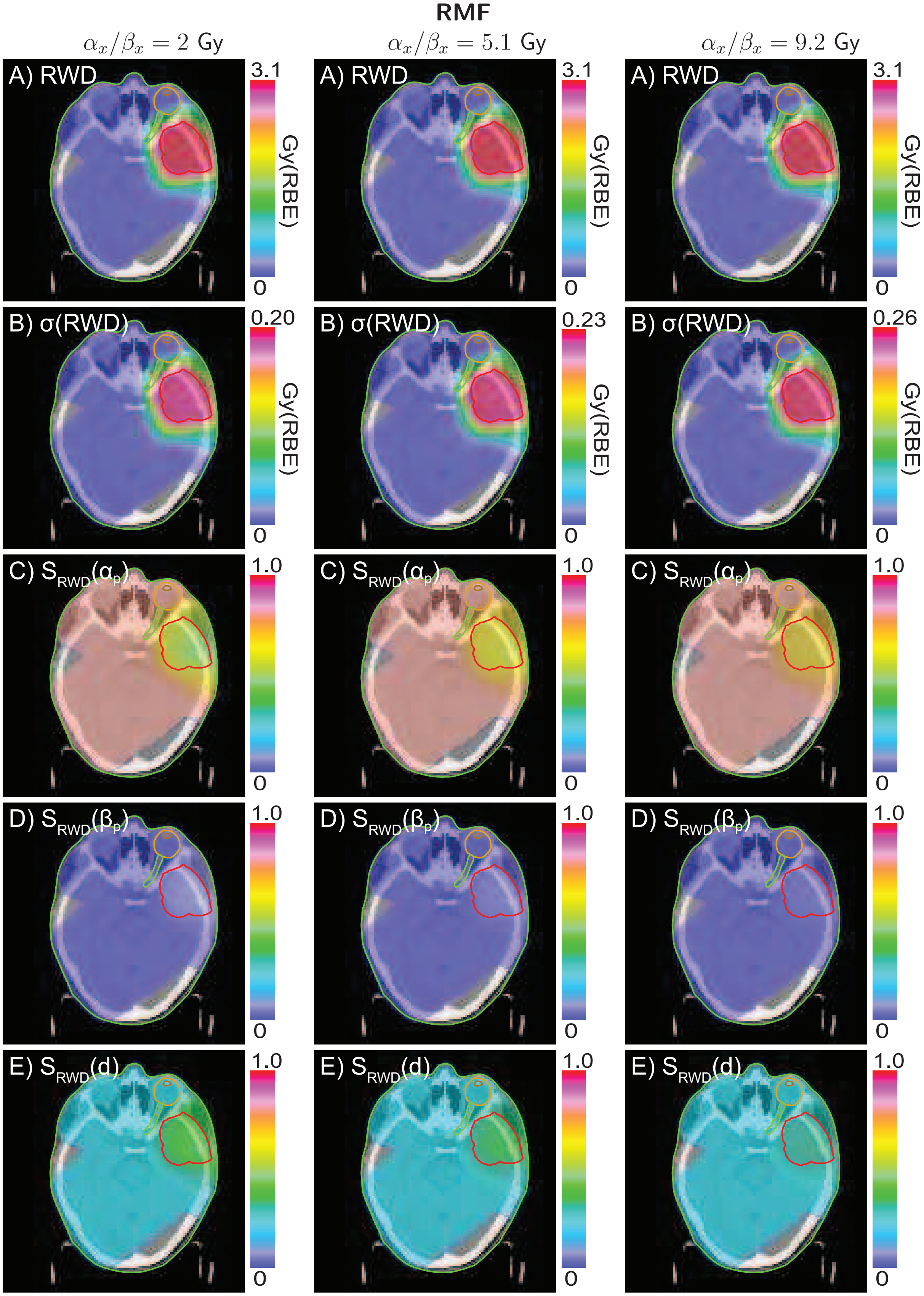

Figure D.1.: Partial SA result for RMF model based treatment plans, uncertainties in α_p, β_p and d and three different α_x/β_x ratios. The panels show the optimized RWD (panels A) together with its uncertainty (panels B). Panels C-E show the sensitivity maps.

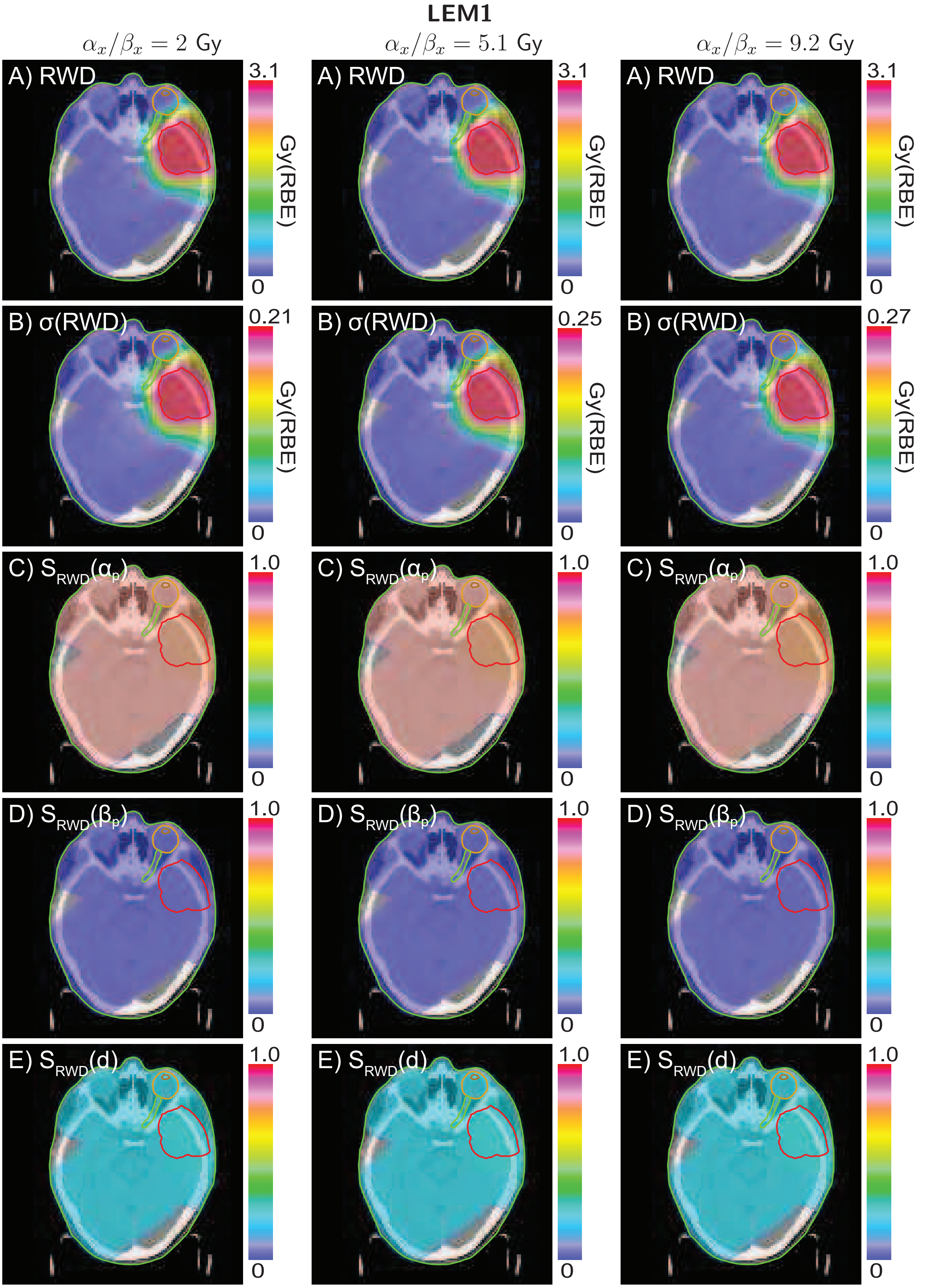

Figure D.2.: Partial SA result for LEM1 based treatment plans, uncertainties in α_p, β_p and d and three different α_x/β_x ratios. The panels show the optimized RWD (panels A) together with its uncertainty (panels B). Panels C-E show the sensitivity maps.

predictions, β_p increases with increasing LET (cf. figure 7.1, page 42). In combination with d^2 this leads to a small increase in $S_{RWD}(\beta_p)$ and a higher $S_{RWD}(d)$ in the PTV. Consequently $S_{RWD}(\alpha_p)$ is reduced in the PTV for RMF model based treatment scenarios. For the LEM1, β_p decreases with increasing LET (cf. figure B.1, in Appendix B). β_p is small inside the PTV. The term $\beta_p d^2$ has no influence on the resulting uncertainty in RWD.

D.2. Partial SA: $RBE\,(\alpha_x, \beta_x, \alpha_p, \beta_p, d)$ for $\alpha_x/\beta_x = 9.2$ Gy

Topic of this section is to give an additional example of the partial SA calculated with $RBE\,(\alpha_x, \beta_x, \alpha_p, \beta_p, d)$. A more detailed description of the approach and its assumptions was given in section 11.3 on page 84. In mentioned section figure 11.5 shows the partial SA result for $\alpha_x/\beta_x = 2$ Gy calculated with the RMF model. Here in figure D.3 a RMF model based treatment plan with $\alpha_x/\beta_x = 9.2$ Gy is evaluated. The results for the corresponding partial SAs based on LEM1 predictions are very similar and not shown here.

Panel A of figure D.3 shows the standard deviation of the RWD distribution. The RWD itself did not change for this partial SA and is equivalent to panel A in figure 10.3 on page 73. Panels B-F in figure D.3 show the five corresponding sensitivity maps. The planning target volume (PTV) is marked in red, the left optical nerve in green together with the left eyeball (orange) and the left lens (brown).

The trends in the sensitivity maps are similar to the partial SA with $\alpha_x/\beta_x = 2$ Gy shown in figure 11.5 on page 85. For $\alpha_x/\beta_x = 9.2$ Gy the changes between sensitivity values inside and outside the PTV are smaller. $S_{RWD}\,(\alpha_x)$ is approximately 0.45 outside the PTV and declines to 0.35 inside the PTV (panel B). $S_{RWD}\,(\beta_x) \approx 0$ outside the PTV and increases to $S_{RWD}\,(\beta_x) \approx 0.03$ in the PTV (panel C). $S_{RWD}\,(\alpha_p) \approx 0.42$ (panel D) and $S_{RWD}\,(\beta_p) \approx 0$ (panel E) throughout the whole patient. $S_{RWD}\,(d)$ ranges from 0.1 outside the PTV to 0.2 in the PTV (panel F).

The comparison of this partial SA with the comprehensive SA for the RMF model (figure 10.3 on page 73) demonstrates again the drawbacks of this partial SA. Like in the example for $\alpha_x/\beta_x = 2$ Gy the spatial changes of the S_{RWD} values are not reproduced for $\alpha_x/\beta_x = 9.2$ Gy. The corresponding example for $\alpha_x/\beta_x = 2$ Gy is shown in section 11.3 on page 84. This is crucial for the changes distal to the PTV, where potentially organs at risk (OAR) are located. In the patient case used here, the left optical nerve is located in this region.

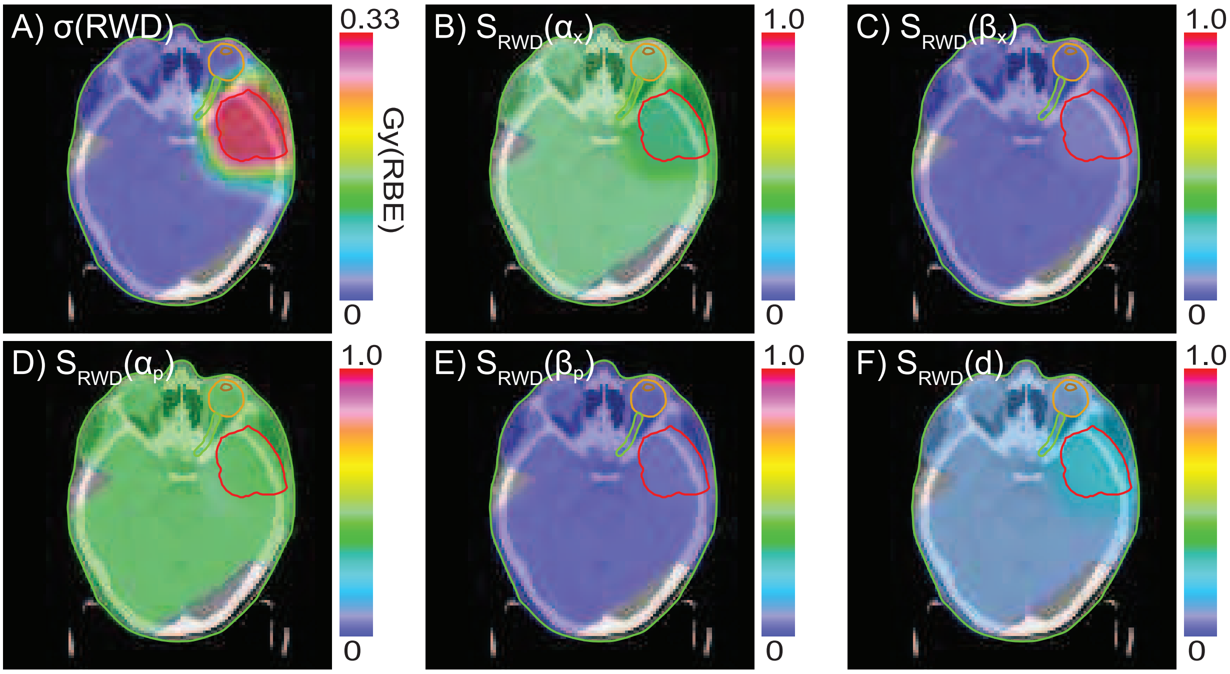

Figure D.3.: Result of the partial SA for a treatment plan based on the RMF model with $\alpha_x/\beta_x = 9.2$ Gy. Panel A shows the uncertainty in the RWD distribution, panels B-F the sensitivity maps for the partial SA of $RBE\,(\alpha_x, \beta_x, \alpha_p, \beta_p, d)$. The dependencies of α_p and β_p on α_x and β_x are omitted. The assigned uncertainties of the input parameter are: $\sigma\,(\alpha_x) = 10\%$, $\sigma\,(\beta_x) = 10\%$, $\sigma\,(\alpha_p) = 10\%$, $\sigma\,(\beta_p) = 10\%$ and $\sigma\,(d) = 5\%$. The planning target volume (PTV) is marked in red, the left optical nerve in green together with the left eyeball (orange) and the left lens (brown).

List of Figures

List of Tables

Bibliography

[1] H. Suit, T. DeLaney, S. Goldberg, H. Paganetti, B. Clasie, L. Gerweck, A. Niemierko, E. Hall, J. Flanz, J. Hallman, and A. Trofimov, "Proton vs carbon ion beams in the definitive radiation treatment of cancer patients," *Radiotherapy and Oncology*, vol. 95, no. 1, pp. 3–22, 2010.

[2] ICRU, "Fundamental quantities and units for ionizing radiation. Report 60," International Commission on Radiation Units and Measurements, Bethesda, MD, 1998.

[3] J. J. Wilkens and U. Oelfke, "Three-dimensional LET calculations for treatment planning of proton therapy," *Zeitschrift für medizinische Physik*, vol. 14, no. 1, pp. 41–46, 2004.

[4] P. Mayles, A. E. Nahum, and J.-C. Rosenwald, *Handbook of radiotherapy physics: Theory and practice.* New York: Taylor & Francis, 2007.

[5] A. M. Kellerer and H. H. Rossi, "A generalized formulation of dual radiation action," *Radiation research*, vol. 75, no. 3, pp. 471–488, 1978.

[6] G. Kraft, "Tumor therapy with heavy charged particles," *Progress in Particle and Nuclear Physics*, vol. 45, pp. 473–544, 2000.

[7] H. Paganetti, A. Niemierko, M. Ancukiewicz, L. E. Gerweck, M. Goitein, J. S. Loeffler, and H. D. Suit, "Relative biological effectiveness (RBE) values for proton beam therapy," *International Journal of Radiation Oncology*Biology*Physics*, vol. 53, no. 2, pp. 407–421, 2002.

[8] T. T. Böhlen, S. Brons, M. Dosanjh, A. Ferrari, P. Fossati, T. Haberer, V. Patera, and A. Mairani, "Investigating the robustness of ion beam therapy treatment plans to uncertainties in biological treatment parameters," *Physics in Medicine and Biology*, vol. 57, no. 23, pp. 7983–8004, 2012.

[9] T. Friedrich, R. Grün, U. Scholz, T. Elsässer, M. Durante, and M. Scholz, "Sensitivity analysis of the relative biological effectiveness predicted by the local effect model," *Physics in Medicine and Biology*, vol. 58, no. 19, pp. 6827–6849, 2013.

[10] E. J. Hall and A. J. Giaccia, *Radiobiology for the radiologist.* Philadelphia: Lippincott Williams & Wilkins, 6th ed ed., 2006.

[11] D. Habermehl, K. Ilicic, S. Dehne, S. Rieken, L. Orschiedt, S. Brons, T. Haberer, K.-J. Weber, J. Debus, S. E. Combs, and M. A. Avila, "The relative biological effectiveness for carbon and oxygen ion beams using the raster-scanning technique in hepatocellular carcinoma cell lines," *PLoS ONE*, vol. 9, no. 12, e113591, 2014.

[12] D. J. Carlson, R. D. Stewart, V. A. Semenenko, and G. A. Sandison, "Combined use of Monte Carlo DNA damage simulations and deterministic repair models to examine putative mechanisms of cell killing," *Radiation research*, vol. 169, no. 4, pp. 447–459, 2008.

[13] W. K. Weyrather, Ritter S., M. Scholz, and G. Kraft, "RBE for carbon track-segment irradiation in cell lines of differing repair capacity," *International Journal of Radiation Biology*, vol. 75, no. 11, pp. 1357–1364, 1999.

[14] J. O. Deasy, A. I. Blanco, and V. H. Clark, "CERR: A computational environment for radiotherapy research," *Medical Physics*, vol. 30, no. 5, pp. 979–985, 2003.

[15] S. Schell and J. J. Wilkens, "Advanced treatment planning methods for efficient radiation therapy with laser accelerated proton and ion beams," *Medical Physics*, vol. 37, no. 10, pp. 5330–5340, 2010.

[16] S. Schell, *Dose delivery and treatment planning methods for efficient radiation therapy with laser-driven particle beams.* PhD thesis, Technische Universität München, München, 2011.

[17] F. Kamp, G. Cabal, A. Mairani, K. Parodi, J. J. Wilkens, and D. J. Carlson, "Fast biological optimization of heavy ion therapy using the mechanisitic repair-misrepair-fixtion (RMF) model and nuclear fragment spectra," *submitted.*

[18] A. Ferrari, P. R. Sala, A. Fasso, and J. Ranft, "FLUKA: A multi-particle transport code," CERN-2005-10 (2005), INFN/TC_05/11, SLAC-R-773, 2005.

[19] T. T. Böhlen, F. Cerutti, M. Chin, A. Fassò, A. Ferrari, P. G. Ortega, A. Mairani, P. R. Sala, G. Smirnov, and V. Vlachoudis, "The FLUKA code: Developments and challenges for high energy and medical applications," *Nuclear Data Sheets*, vol. 120, pp. 211–214, 2014.

[20] K. Parodi, A. Mairani, S. Brons, B. G. Hasch, F. Sommerer, J. Naumann, O. Jäkel, T. Haberer, and J. Debus, "Monte Carlo simulations to support start-up and treatment planning of scanned proton and carbon ion therapy at a synchrotron-based facility," *Physics in Medicine and Biology*, vol. 57, no. 12, pp. 3759–3784, 2012.

[21] F. Kamp, S. C. Brüningk, G. Cabal, A. Mairani, K. Parodi, and J. J. Wilkens, "Variance-based sensitivity analysis of biological uncertainties in carbon ion therapy," *Physica Medica*, vol. 30, no. 5, pp. 583–587, 2014.

[22] S. C. Brüningk, "Integrating the concept of equivalent uniform dose into 3D treatment planning for carbon ion therapy," Master Thesis, Technische Universität München, München, 2014.

[23] F. Kamp, "Comparison of the lateral dose fall-off for proton and ion beams in radiation therapy," Diploma Thesis, Technische Universität München, München, 2011.

[24] M. Goitein and J. M. Sisterson, "The influence of thick inhomogeneities on charged particle beams," *Radiation research*, vol. 74, no. 2, p. 217, 1978.

[25] S. Nill, *Development and application of a multi-modality inverse treatment planning system.* PhD thesis, University of Heidelberg, Heidelberg, 2011.

[26] M. Scholz and G. Kraft, "Calculation of heavy ion inactivation probabilities based on track structure, x ray sensitivity and target size," *Radiation Protection Dosimetry*, vol. 52, no. 1-4, pp. 29–33, 1994.

[27] M. Scholz, A. M. Kellerer, W. Kraft-Weyrather, and G. Kraft, "Computation of cell survival in heavy ion beams for therapy," *Radiation and Environmental Biophysics*, vol. 36, no. 1, pp. 59–66, 1997.

[28] W. Schlegel, T. Bortfeld, and Grosu A.-L., eds., *New technologies in radiation oncology.* Medical radiology, Berlin and Heidelberg: Springer, 2006.

[29] R. Grün, T. Friedrich, T. Elsässer, M. Krämer, K. Zink, C. P. Karger, M. Durante, R. Engenhart-Cabillic, and M. Scholz, "Impact of enhancements in the local effect model (LEM) on the predicted RBE-weighted target dose distribution in carbon ion therapy," *Physics in Medicine and Biology*, vol. 57, no. 22, pp. 7261–7274, 2012.

[30] D. Schulz-Ertner, C. P. Karger, A. Feuerhake, A. Nikoghosyan, S. E. Combs, O. Jäkel, L. Edler, M. Scholz, and J. Debus, "Effectiveness of carbon ion radiotherapy in the treatment of skull-base chordomas," *International Journal of Radiation Oncology*Biology*Physics*, vol. 68, no. 2, pp. 449–457, 2007.

[31] T. Friedrich, U. Scholz, T. Elsässer, M. Durante, and M. Scholz, "Calculation of the biological effects of ion beams based on the microscopic spatial damage distribution pattern," *International Journal of Radiation Biology*, vol. 88, no. 1-2, pp. 103–107, 2012.

[32] G. Russo, *Development of a radiobiological database for carbon ion treatment planning systems: Modelling and simulating the irradiation process.* PhD thesis, Universita degli studi di Torino, Turin, 2011.

[33] M. Zaider and H. H. Rossi, "The synergistic effects of different radiations," *Radiation research*, vol. 83, no. 3, pp. 732–739, 1980.

[34] M. C. Frese, V. K. Yu, R. D. Stewart, and D. J. Carlson, "A mechanism-based approach to predict the relative biological effectiveness of protons and carbon ions in radiation therapy," *International Journal of Radiation Oncology*Biology*Physics*, vol. 83, no. 1, pp. 442–450, 2012.

[35] V. A. Semenenko and R. D. Stewart, "A Fast Monte Carlo algorithm to simulate the spectrum of DNA damages formed by ionizing radiation," *Radiation research*, vol. 161, no. 4, pp. 451–457, 2004.

[36] V. A. Semenenko and R. D. Stewart, "Fast Monte Carlo simulation of DNA damage formed by electrons and light ions," *Physics in Medicine and Biology*, vol. 51, no. 7, pp. 1693–1706, 2006.

[37] W. H. Barkas, "Nuclear research emulsions. Vol. 1: Techniques and theory," *Pure and Applied Physics, New York: Academic Press, 1963*, vol. 1, 1963.

[38] Y. Hsiao and R. D. Stewart, "Monte Carlo simulation of DNA damage induction by x-rays and selected radioisotopes," *Physics in Medicine and Biology*, vol. 53, no. 1, pp. 233–244, 2008.

[39] R. D. Stewart, V. K. Yu, A. G. Georgakilas, C. Koumenis, J. H. Park, and D. J. Carlson, "Effects of radiation quality and oxygen on clustered DNA lesions and cell death," *Radiation research*, vol. 176, no. 5, pp. 587–602, 2011.

[40] T. Friedrich, U. Scholz, T. Elsässer, M. Durante, and M. Scholz, "Systematic analysis of RBE and related quantities using a database of cell survival experiments with ion beam irradiation," *Journal of Radiation Research*, vol. 54, no. 3, pp. 494–514, 2013.

[41] Y. Furusawa, K. Fukutsu, M. Aoki, H. Itsukaichi, K. Eguchi-Kasai, H. Ohara, F. Yatagai, T. Kanai, and K. Ando, "Inactivation of aerobic and hypoxic cells from three different cell lines by accelerated 3 He-, 12 C- and 20 Ne-ion beams," *Radiation research*, vol. 154, no. 5, pp. 485–496, 2000.

[42] J. J. Wilkens and U. Oelfke, "Fast multifield optimization of the biological effect in ion therapy," *Physics in Medicine and Biology*, vol. 51, no. 12, pp. 3127–3140, 2006.

[43] A. Wambersie, J. H. Hendry, P. Andreo, P. M. DeLuca, R. Gahbauer, H. Menzel, and G. Whitmore, "The RBE issues in ion-beam therapy: conclusions of a joint IAEA/ICRU working group regarding quantities and units," *Radiation Protection Dosimetry*, vol. 122, no. 1-4, pp. 463–470, 2007.

[44] J. Nocedal and S. J. Wright, *Numerical optimization.* Springer series in operations research, New York: Springer, 1999.

[45] M. Goitein, *Radiation oncology: A physicist's-eye view.* Biological and medical physics, biomedical engineering, New York, NY: Springer, 2008.

[46] Chen, G. T. Y., C. A. Pelizzari, D. R. Spelbring, and A. Awan, *Evaluation of treatment plans using dose volume histograms.* United States: S Karger Publishers Inc, 1987.

[47] R. E. Drzymala, R. Mohan, L. Brewster, J. Chu, M. Goitein, W. Harms, and M. Urie, "Dose-volume histograms," *International Journal of Radiation Oncology*Biology*Physics*, vol. 21, no. 1, pp. 71–78, 1991.

[48] A. Niemierko and M. Goitein, "Implementation of a model for estimating tumor control probability for an inhomogeneously irradiated tumor," *Radiotherapy and Oncology*, vol. 29, no. 2, pp. 140–147, 1993.

[49] A. Saltelli, *Sensitivity analysis in practice: A guide to assessing scientific models.* Hoboken, NJ: Wiley, 2004.

[50] K. O. Arras, "An introduction to error propagation: Derivation, meaning and examples of Cy= Fx Cx Fx," 1998.

[51] A. Saltelli, M. Ratto, T. Andres, F. Campolongo, J. Cariboni, D. Gatelli, M. Saisana, and S. Tarantola, *Global sensitivity analysis: The primer.* Chichester: John Wiley, 2008.

[52] T. Friedrich, W. Weyrather, T. Elsässer, M. Durante, and M. Scholz, “Accuracy of RBE: experimental and theoretical considerations,” *Radiation and Environmental Biophysics*, vol. 49, no. 3, pp. 345–349, 2010.

[53] L. Papula, *Mathematische Formelsammlung: Für Ingenieure und Naturwissenschaftler*. Wiesbaden: Springer Vieweg, 2014.

List of Publications

Papers in journals

First author

- Kamp F., S.C. Brüningk, G. Cabal, A. Mairani, K. Parodi and J.J. Wilkens: "Variance-based sensitivity analysis of biological uncertainties in carbon ion therapy" Physica Medica 30(5), 583-587, 2014.
- Kamp F., G. Cabal, A. Mairani, K. Parodi, J.J. Wilkens and D.J. Carlson: "Fast biological optimization of heavy ion therapy using the mechanistic repair-misrepair-fixation (RMF) model and nuclear fragment spectra" submitted

Coauthor

- Brüningk S.C., F. Kamp and J. J. Wilkens: "EUD-based biological optimization for carbon ion therapy" in preparation
- Landry G., G. Dedes, C. Zoellner, J. Handrack, G. Janssens, J. Orban de Xivry, M. Reiner, C. Paganelli, M. Riboldi, F. Kamp, M. Söhn, J.J. Wilkens, G. Baroni, C. Belka and K. Parodi: "Phantom based evaluation of CT to CBCT image registration for proton therapy dose recalculation" accepted in Phys. Med. Biol.
- Landry G., G. Dedes, J. Handrack, R. Nijhuis, C. Thieke, G. Janssens, J. Orban de Xivry, M. Reiner, F. Kamp, J. Wilkens, C. Paganelli, M. Riboldi, G. Baroni, U. Ganswindt, C. Belka and K. Parodi: "Investigating CT to CBCT image registration for head and neck proton therapy as a tool for daily dose recalculation" accepted in Med. Phys.

Papers in books and conference abstracts

First author

- Kamp F., G. Cabal, A. Mairani, K. Parodi, J.J. Wilkens and D.J. Carlson: "Predicting the Relative Biological Effectiveness of Carbon Ion Radiation Therapy Beams Using the Mechanistic Repair-Misrepair-Fixation (RMF) Model and Nuclear Fragment Spectra" International Journal of Radiation Oncology, Biology, Physics 90(1, Suppl.), S849, 2014. (poster)
- Kamp F. and J.J. Wilkens: "Variance-based Sensitivity Analysis to Quantify the Impact of Biological Model Uncertainties in Carbon Ion Therapy" in: S. Klöck (ed.) Joint Conference of the SSRMP, DGMP, ÖGMP: Dreiländertagung der Medizinischen Physik (Zurich/Switzerland), ISBN 978-3-9816508-5-3, p. 192, 2014. (oral presentation)

- Kamp F., S.C. Brüningk and J.J. Wilkens: "Variance-Based Sensitivity Analysis to Quantify the Impact of Biological Uncertainties in Particle Therapy" Med. Phys. 41(6), p. 494, 2014. (oral presentation)
- Kamp F. and J.J. Wilkens: "Variance Based Sensitivity Analysis of Biological Uncertainties in Carbon Ion Therapy" Radiotherapy & Oncology 110(Suppl. 1) p. S50, 2014. (oral presentation)
- Kamp F. and J.J. Wilkens: "Sensitivity Analysis of Biological Uncertainties in Carbon Ion Therapy" Particle Radiosurgery, A new Frontier in Physics in Medicine, 25-29 August 2013, Obergurgl/Austria, 2013. (poster)
- Kamp F. and J.J. Wilkens: "Vergleich von optimalen Setup-Margins aufgrund der unterschiedlichen lateralen Aufstreuung von Protonen und Kohlenstoffionen in der Strahlentherapie" in: Hodapp N., J. Hennig, M. Mix (eds.) Medizinische Physik 2010 (Deutsche Gesellschaft für Medizinische Physik: Freiburg) ISBN 3-925218-88-2, 74-77, 2010. (oral presentation)

Coauthor

- Brüningk S., F. Kamp and J.J. Wilkens: "Biological optimization for carbon ion therapy planning based on the Equivalent Uniform Dose (EUD)" in: S. Klöck (ed.) Joint Conference of the SSRMP, DGMP, ÖGMP: Dreiländertagung der Medizinischen Physik (Zurich/Switzerland), ISBN 978-3-9816508-5-3, p. 192, 2014.
- Landry G., G. Dedes, J. Handrack, G. Cabal, R. Nijhuis, M. Söhn, M. Reiner, U. Ganswindt, C. Thieke, G. Janssens, J. Orban de Xivry, C. Paganelli, F. Kamp, M. Riboldi, J.J. Wilkens, G. Baroni, C. Belka and K. Parodi: "A novel approach to estimate the dosimetric influence of anatomical changes in head and neck cancer patients undergoing proton therapy using daily CBCT imaging" in: S. Klöck (ed.) Joint Conference of the SSRMP, DGMP, ÖGMP: Dreiländertagung der Medizinischen Physik (Zurich/Switzerland), ISBN 978-3-9816508-5-3, p. 192, 2014.
- Dedes G., G. Landry, J. Handrack, G. Cabal, R. Nijhuis, M. Söhn, M. Reiner, C. Thieke, U. Ganswindt, F. Kamp, J.J. Wilkens, C. Belka and K. Parodi: "Monte Carlo study on the sensitivity of positron and prompt-gamma imaging to proton range variations due to inter-fractional anatomical changes in head and neck and prostate cancer patients" in: S. Klöck (ed.) Joint Conference of the SSRMP, DGMP, ÖGMP: Dreiländertagung der Medizinischen Physik (Zurich/Switzerland), ISBN 978-3-981 6508-5-3, p. 192, 2014.
- Brüningk S.C., F. Kamp and J.J. Wilkens: "Equivalent uniform dose (EUD) based biological optimization for carbon ion therapy" Radiotherapy & Oncology 110(Suppl. 1) pp. S17-18, 2014.

Acknowledgment

Many great people contributed to this work and made it possible as it is. At this point I would like to thank them for their help, advice and support.

First of all I thank my supervisor Prof. Dr. Jan J. Wilkens for his always open door, for all the advice, help and ideas. I had amazing years in the advanced technologies in radiation therapy group and I thank you, Jan, for all the support throughout this time. The thesis is part of the DFG project "A unified framework for biological optimization in ion beam radiation therapy" which provided the funding. I am also very thankful to Prof. Dr. Franz Pfeiffer for agreeing to be the second referee.

I had the great opportunity to stay three month at the Yale - New Haven Hospital. I thank Prof Dr. David J. Carlson for providing this opportunity, for all the discussions and explanations. In this context I also thank Olivia Kelada for the warm welcome and the DAAD (German Academic Exchange Service) for the scholarship that made those amazing three months possible.

Furthermore, I am very grateful for the fruitful collaboration with the medical physics group of the Ludwig-Maximilians-University in Munich. I especially thank Prof. Dr. Katia Parodi, Prof. Dr. Gonzalo Cabal and Dr. Andrea Mairani for the fragmentation data they provided.

Then I would like to express my gratitude to a small but powerful office team. Kerstin Hofmann, Frauke Alexander, Dr. Tanja Wenzl, Birgit Müller, Karin Burger, Dr. Nicole Humble and Severin Kampfer, thank you for all the coffees, cakes and laughs we shared. I especially thank Sarah Brüningk for her enthusiasm and the great projects we managed together. This work is based on the excellent work of Dr. Stefan Schell, who prepared CERR for ion therapy.

Last but not least I want to thank my family for the continuous support to get me to this point and Alexandra Zvereva for being in my life, moving to Munich and supporting me whenever she can.